LUNFD6/(NFFL-7217)2004

Optimized event selection within the chargino analysis at the DELPHI experiment.

Thesis submitted for the degree of
Philosophy Licentiat
by

Stefan Ask

LUND UNIVERSITY

Experimental High Energy Physics
Department of Physics
Lund University

By:

Stefan Ask

Division of Experimental High Energy Physics
Lund University, Box 118, SE-221 00 Lund, Sweden
Stefan.ask@hep.lu.se

Abstract

A search for charginos has been made at the DELPHI experiment. The final results were based on the data collected during the years 1999-2000, corresponding to a integrated luminosity of 450 pb^{-1} at center–of–mass energies up to 209 GeV. Since no significant signs of a chargino signal have been observed the results have been used to set exclusion limits and to constrain the supersymmetric parameter space. Within this analysis the event selection has been optimized using a likelihood ratio technique to give the optimal exclusion in the absence of a signal. This event selection technique will be the main topic of this licenctiate thesis, but the other parts of the chargino analysis will be discussed as well.

The analysis and results presented in this thesis are published in

Searches for supersymmetric particles in e+e- collisions up to 208 GeV, and interpretation of the results within the MSSM ,
J. Abdallah *et.al.* [DELPHI Collaboration], CERN-EP 2003-007, hep-ex/0311019
(Accepted for publication by Eur. Phys. J C).

Contributed paper to:

The International Europhysics Conference on High Energy Physics,
European Physical Society (EPS 2003), Aachen, Germany July 2003.

XXI International Symposium on Lepton and Photon Interactions at High Energies,
Lepton Photon (LP 2003) FNAL , Batavia, Illinois USA, August 2003.

Acknowledgment

Since the DELPHI experiment is a collaboration consisting of more than 500 participants I will only mention the persons I have worked closest with. First I would like to thank my supervisor Dr.Vincent Hedberg for all encouragement, supervision and criticism during my work in the chargino team. I would also like to acknowledge Vincent for the iterative and painful process of reading and commenting this thesis. I would like to thank Dr.Thomas Alderweireld whom I worked with/for in the chargino team. Not only for the guidance through the analysis work and the very fun collaboration, but also for the continuous effort to get me to the same level of understanding, concerning the analysis, as him (maybe one day ?). Furthermore I would like to express my gratitude, since I learned very much during our work in many different, related areas, such as statistics, SUSY theory etc... Finally I would like to thank the people in the DELPHI SUSY community Drs., Jalal Abdallah, Mikael Berggren, Maria Espirito Santo, Klas Hultqvist, Per Johansson, Anna Lipniacka, Luc Pape, Andrea Perrotta, Pierpaolo Rebecchi, Ulrich Schwickerath, Patrice Verdier, among others for the open and relaxed atmosphere which made the work both easier and funnier, both during the work with the SUSANA paper and in general. I would like to express a special thanks to Dr.Patrice Verdier for the help to implement his “weighting” method to estimate the systematic errors.

Contents

Chapter 1

Introduction

Chargino pair production at LEP was one of the most probable first sign of supersymmetry (SUSY) if it had existed within the kinematic reach of the LEP accelerator. The reason for this is a combination of things. From the experimental point of view the fact that the LEP accelerator was the largest and most powerful accelerator of its kind, which enabled one to search for heavier unknown particles, was the main reason together with the very clean events which are produced in e^+e^- collisions. The chargino pair production is also the process which would have the highest cross section in a very large part of the SUSY parameter space (except for a few processes which are not possible to detect). Chargino pair production would therefore have a non-negligible cross section through out the whole SUSY parameter space in the allowed kinematical region.

The reason why supersymmetry and its additional particles should be in the region of 1 TeV are mainly related to the problems in the Standard Model (SM) which appear at energies of > 10 TeV. Examples are unification of the gauge interactions, the extremely sensitive tuning of the Higgs mass and a first attempt towards including gravity.

In the DELPHI experiment the chargino analysis was based on four different event topologies, the fully hadronic, the semi–leptonic, the leptonic and the radiative topology. The event selection was optimized further with respect to the characteristics of a possible chargino signal with a likelihood ratio method. The likelihood ratio method did not only improve the sensibility to detect a chargino signal but did also provide a very convenient method for event selection at different luminosities. The analysis would otherwise have to be re-tuned for every data sample with a sequential cut selection. Since no significant signs of a chargino signal have been observed, exclusion limits have been set and the event selection optimized the exclusion limits in the absence of a signal. The limits were computed with a multichannel Bayesian formula, which makes it possible to combine the results properly from the different event topologies obtained at different center–of–mass energies at different integrated luminosities in a easy way. These exclusion limits were then interpreted in terms of excluded SUSY parameter space for different theoretical scenarios. The scenario where the chargino search has the largest impact is the so called SUGRA scenario and hence only this scenario will be addressed here.

The focus of this thesis is on the optimized event selection used in the DELPHI chargino search in the semi–leptonic and radiative topologies.

The thesis is divided into the following chapters.

SUperSYmmerty:

This chapter gives a brief introduction to supersymmetry and the reasons why it is considered to be the most attractive extension to the SM. A more detailed description of the chargino related production and decay processes are also given. First some of the problems with the SM as a theory at higher energies are addressed and after that an introduction to supersymmetry is made.

Then a section describes how SUSY would cure the known problems in the SM at higher energies and why it is considered to be such an attractive theoretical scenario. The rest of the chapter concerns the phenomenology related to a possible chargino production at LEP. These sections discuss the SUSY particle mass spectrum, especially focused on the sparticles closest related to the chargino processes. It also address the chargino production cross section and decay channels. This chapter describes the aspects of SUSY which are of interest to the chargino analysis. The description of SUSY is brief, and for a more general and rigorous introduction to SUSY the reader is referred to [3, 4, 5, 6].

Experimental Facilities and Simulations:

A description of the Large Electron Positron collider (LEP) at CERN is made. The DELPHI experiment and its sub detectors are described, with the focus on the sub-detectors most relevant for the chargino analysis. The problem with the main tracking chamber (the Time Projection Chamber, TPC) in DELPHI that arose during the last months of year 2000 will also be discussed.

The data sample will be presented together with the standard model background events and the chargino signal events that have been simulated. SM background events from 37 different processes were simulated and additional Monte Carlo samples were made which takes the defect TPC into account (both for the chargino signal and for the SM background).

The Likelihood ratio based event selection:

The different steps of the event selection are described in detail as well as the likelihood ratio method used to optimize the exclusion limits. This corresponds to four different selection steps: topology-, common-, pre- and final-selection. The first three are sequential selections and the final selection consists of the likelihood ratio based selection which minimize the excluded cross section in the absence of a signal. The final selection is further more optimized with respect to the discriminating variables used in the likelihood ratio method and the optimal set of variables is used for the analysis. The methods used to compute the corresponding statistical and systematic errors will also be discussed. Finally the selection results are presented in terms of the selected number of events at different stages of the selection procedure together with the final candidate events selected in the analysis, with a comparison with simulated SM expectations. The selection results presented in the last part of this section will only concern the semi–leptonic and radiative topologies.

The Final Results:

The interpretation of the results from the chargino search, in terms of exclusion limits, will be discussed together with a brief description of the limit computation. This includes the number of candidates in all the topologies, the obtained signal detection efficiencies from the events selection and the corresponding excluded SUSY parameter space.

Conclusions and Summary:

Finally the conclusions about the results will be summarized together with the obtained chargino mass limits.

Chapter 2

SUperSYmmetry

2.1 An Introduction and Overview

This section will give a brief introduction to supersymmetry and the relevant aspects and scenarios for the chargino search presented in this thesis. The main arguments for why SUSY is such an attractive extension of the SM will be addressed as well. For a more general and rigorous introduction to SUSY the reader is referred to [3, 4, 5, 6].

2.1.1 The Problems with the Standard Model

The standard model as it looks today is a very accurate and self consistent theory. It can describe all experimental measurements until now with a very high precision. A question often asked is therefore why the SM cannot be "the theory of everything" (TOE), since there are no experiments which disagree with it? There are several reasons and three major problems will be discussed here which would be solved if SUSY existed at the TeV scale.

First of all the SM cannot be the TOE since it does not contain a quantum description of gravity and hence does not contain everything. This is also a problem for many extensions of the SM. One might regard the string theory as the only present possibility which incorporate gravity but string theory is at present very far from describing nature. This problem would not be solved by SUSY, but it would be brought one step further towards a solution and SUSY is usually a necessity for many string theories.

The second problem refers to the unification of the three remaining gauge interactions. Since the unification of the electroweak (EW) theory it has been suggested that also the strong force might be included in a theory, a so called Grand Unified Theory (GUT), where all the SM gauge interactions are unified at a higher energy scale (since they are not very similar at the energy scale probed by experiments). A necessary condition to construct a GUT is that if the coupling constants are renormalized to higher energies they should at some point get the same value, i.e. the strength of the gauge interactions unifies at a certain energy scale. If the three SM coupling constants are renormalized according to the SM they unfortunately do not end up together at the same energy scale which indicates that something new must be taken into account also for a GUT.

The third problem is the so called **hierarchy problem**. Even if one does not care about having a TOE or a GUT, the SM will behave badly at higher energies if not something new is introduced. The hierarchy problem can be formulated as why is the W-mass ($m_W = 81$ GeV/c^2) so much smaller than the Plank mass ($m_P \sim 10^{18}$ GeV/c^2)? This is equivalent to asking why the gravitational force is so much weaker than the electroweak force ? This might sound philosophical but there are practical consequences to the SM from this as well. If there would be nothing in addition to the SM until the Plank scale, the correction to the Higgs mass (where Λ now is the Plank mass) would be:

$$m_h^2 \sim m_{h0}^2 + \frac{\lambda}{4\pi^2}\Lambda^2 + \delta m_h^2. \qquad (2.1)$$

The Higgs mass would then have a quadratic divergence that would have to be canceled by the term δm_h^2. This is a possibility but the $\frac{\lambda}{4\pi^2}\Lambda^2$ term would be in the order of $\mathcal{O}(10^{18}\ \mathrm{GeV}/c)^2$ which must be canceled by δm_h^2 which should result in a m_h^2 of the order of $\mathcal{O}(10^2\ \mathrm{GeV}/c^2)^2$ (m_h cannot be higher in order to prevent unitarity violation of the longitudinal gauge boson scattering). This implies that the parameters must be tuned to give a m_h which is 16 orders of magnitude less than Λ and δm_h. This tuning would in addition have to be done again for every order in perturbation theory. This is regarded by most physicists as an unnatural precision of the parameter tuning and this is also referred to as the **naturalness problem**.

2.1.2 Supersymmetry

Supersymmetry is a symmetry between fermions and bosons and the idea was introduced already in the 70's. The motivation for a supersymmetric theory was at that time not to cure any of the problems mentioned above, but in order to describe the neutrino or the mesons and baryons. A supersymmetry operator $\mathcal{Q}$ would transform a fermion into a boson and the other way around and hence for any fermion field there would exists a bosonic partner field,

$$\mathcal{Q}|Boson>=|Fermion>, \qquad \mathcal{Q}|Fermion>=|Boson>. \qquad (2.2)$$

The two partners would have exactly the same quantum numbers except for the difference of 1/2-spin. Since the other quantum numbers should be identical there is no particle pair in the SM that could be SUSY partners to each other, so all the SM fermion and boson SUSY partners should be undiscovered. For renormalization reasons, the SUSY partners to the fermion fields would have to be scalar fields and the partners to the SM boson fields would have spin–1/2. The scalar partner to the SM fermions are normally called sfermions ("s" for scalar) and the partners to the SM gauge bosons gets "ino" added at the end, like photino, zino, higgsino etc. Since the total number of degrees of freedom for the boson fields in a SUSY must be equal to the degrees of freedom of the fermion fields, there would exists two scalar partners, due to the two helicity states, for each fermion field. These are in general called the left and right handed sfermions, but refers to two different scalar particles, which interact differently like the two fermion helicity states.

Apart from these new SUSY partners, a SUSY theory also implies that two Higgs doublets are needed. This is to prevent triangular gauge anomalies of the electroweak theory, which includes $Tr[Y^3] = Tr[T_3^2 Y] = 0$, which runs over all left-handed fermionic Weyl fields. T_3 and Y corresponds to the third component of weak isospin and the hyper charged respectively, normalized to the electromagnetic charge as $Q_{em} = Y + T_3$. In the SM there is only one bosonic Higgs doublet, which hence do not contribute to the trace, but in SUSY there is a fermionic partner and for that reason two doublets are needed in order to cancel each other out. In addition to this, two Higgs doublets are also needed in a SUSY theory in order to give the up and down[1] quarks their correct masses from the Yukawa terms.

The total set of fields needed for the minimal supersymmetric extension of the standard model (MSSM) is shown in table 2.1, together with their transformation properties according to the SM gauge groups, $SU(3)_C$, $SU(2)_L$, $U(1)_Y$[2]. Since the supersymmetry partners only differ with respect to the spin, the sparticles will interact in the same way and with the same

[1]Together with the other families.

[2]Most of the conventions will follow the one used for the SUSYGEN generator [21], since it has been used for most of the computations presented here.

Names		spin 0	spin 1/2	$SU(3)_C$, $SU(2)_L$, $U(1)_Y$
squarks, quarks	Q	$(\tilde{u}_L \ \ \tilde{d}_L)$	$(u_L \ \ d_L)$	$(\,\mathbf{3},\,\mathbf{2}\,,\,\frac{1}{6})$
(×3 families)	$\bar{u}$	$\tilde{u}_R^*$	$u_R^\dagger$	$(\,\overline{\mathbf{3}},\,\mathbf{1},\,-\frac{2}{3})$
	$\bar{d}$	$\tilde{d}_R^*$	$d_R^\dagger$	$(\,\overline{\mathbf{3}},\,\mathbf{1},\,\frac{1}{3})$
sleptons, leptons	L	$(\tilde{\nu}\ \tilde{e}_L)$	$(\nu \ \ e_L)$	$(\,\mathbf{1},\,\mathbf{2}\,,\,-\frac{1}{2})$
(×3 families)	$\bar{e}$	$\tilde{e}_R^*$	$e_R^\dagger$	$(\,\mathbf{1},\,\mathbf{1},\,1)$
Higgs, higgsinos	H_2	$(H_2^+ \ \ H_2^0)$	$(\tilde{H}_2^+ \ \ \tilde{H}_2^0)$	$(\,\mathbf{1},\,\mathbf{2}\,,\,+\frac{1}{2})$
	H_1	$(H_1^0 \ \ H_1^-)$	$(\tilde{H}_1^0 \ \ \tilde{H}_1^-)$	$(\,\mathbf{1},\,\mathbf{2}\,,\,-\frac{1}{2})$

Names	spin 1/2	spin 1	$SU(3)_C$, $SU(2)_L$, $U(1)_Y$
gluino, gluon	$\tilde{g}$	g	$(\,\mathbf{8},\,\mathbf{1}\,,\,0)$
winos, W bosons	$\tilde{W}^\pm \ \ \tilde{W}^0$	$W^\pm \ \ W^0$	$(\,\mathbf{1},\,\mathbf{3}\,,\,0)$
bino, B boson	$\tilde{B}^0$	B^0	$(\,\mathbf{1},\,\mathbf{1}\,,\,0)$

Table 2.1: The minimal SUSY fields contents in the Weyl representation [4].

strength as the SM partners and they should in principle then also have the same mass. This is obviously not the case since scalar electrons etc. would have been discovered easily a long time ago and hence the supersymmetry must be a broken symmetry at the TeV scale. A soft supersymmetry breaking mechanism would then give rise to the mass splitting between the SM and SUSY partners.

In the same way as the EW symmetry breaking give rise to a mixing of the W^0 and B^0 into the Z^0 and the photon, the SUSY symmetry breaking mixes the SUSY partners of the SM gauge bosons into so called gauginos. The SUSY partners to the charged gauge bosons, $\tilde{W}^\pm$, $\tilde{H}_1^-$, $\tilde{H}_2^+$, mixes into two mass eigenstates called the **charginos** ($\tilde{\chi}_i^\pm$, $i = 1,\ 2$), which are the particles searched for in the analysis presented here. The SUSY partners to the neutral SM gauge bosons, $\tilde{\gamma}$, $\tilde{Z}$, $\tilde{H}_1^0$, $\tilde{H}_2^0$, mixes into four different mass eigenstates, the **neutralinos** ($\tilde{\chi}_i^0$, $i = 1,\ 2,\ 3,\ 4$). The gaugino masses and their field composition will be discussed in detail in section 2.2.

There are several mechanisms proposed which could generate the SUSY breaking. The most popular one is that SUSY should be broken by gravity, the so called supergravity induced SUSY breaking (SUGRA). In this case the theory is supersymmetric at the GUT scale (about 10^{16} GeV), and becomes broken by gravitational strength interactions on its way down to the TeV scale. At the GUT scale, gaugino and sfermion mass unification is normally assumed. In this scenario their masses at the GUT scale are given by the parameters $m_{1/2}$ and m_0 respectively and under this assumption the parameter A_0 is normally used to determine the Yukawa couplings between the sfermions. The next step is to assume whether R-parity should be conserved or not. R-parity is represented by the multiplicative quantum number $R_p = (-1)^{3B+L+2S}$, where SM particles obtains the value +1 and the SUSY partners -1. R-parity violating processes could be allowed in a SUSY theory, but for various reasons R-parity conservation is normally considered to be the most attractive alternative. R-parity conservation result in two important phenomenological consequences namely that the lightest SUSY particle (LSP) will be stable and that the SUSY particles would be produced in pairs. The stable LSP can be only weakly interacting due to cosmological constrains and the stable LSP prediction is one (strong) reason why R-parity conservation is a very attractive scenario, since the LSP is a good candidate to solve the cold dark matter problem observed in the universe. Since the LSP is only weakly interacting, production of SUSY events in a experiment would get the characteristic signature of missing energy due to the escaping LSP.

The chargino search presented here is made under the mass unification and R-parity conservation assumptions previously described and this combined with the knowledge about the EW symmetry breaking means that the only additional parameters needed to describe this SUGRA theory are: the ratio of the vacuum expectation values from the two Higgs doublets, $\tan\beta$, and the sign of the Higgs sector mixing parameter μ. The last constraint will be relaxed in the analysis presented here and hence μ will be treated as a free parameter. Under these assumptions all masses and couplings at the EW scale can be determined from the SUSY parameters

$$m_{1/2},\ m_0,\ A_0,\ \tan\beta\ , sign(\mu), \tag{2.3}$$

by renormalization. This is normally called the minimal SUGRA (mSUGRA) scenario and as will be shown, the chargino search presented here will depend on all these variables with the exception of A_0.

There are, as mentioned above, also other theories of how SUSY can be broken and the most popular alternative is the so called gauge mediated SUSY breaking scenario, where SUSY is broken by normal gauge interactions [7]. The chargino search presented here will, however, only discuss the SUGRA scenario, since it is the most popular model and due to the large importance of the chargino search with this model.

2.1.3 How SUSY Would Improve the SM

What makes this boson–fermion symmetry so attractive? For many theorists the fact that the supersymmetric algebra is the only known way to unify the spin-2 graviton with the other spin-1 gauge bosons, and it therefore is crucial for string theories etc., is a reason which alone makes SUSY (one of) the most attractive extensions of the SM. Other attractive implications exists as well.

As mentioned in the beginning, it would be nice if all the SM gauge interactions were unified at a higher energy scale. Especially since it is today known that all three gauge couplings have a converging behavior with increasing energy plus the fact that the electromagnetic and weak interactions already are unified. The SM running couplings do not converge towards the same value and they can for that reason not be converted into a single gauge group representation. Since this imply that the three curves, representing the running couplings, should cross each other at the same point (see figure 2.1) one realizes that this is necessarily not a trivial problem. In a SUSY theory, as the one described here, the contribution of SUSY partner particles with masses in the order of TeV/c^2 would automatically contribute to the running gauge couplings in such a way that they all would unify at the same point at the GUT scale. This is shown in figure 2.1, which shows the evolution of the three coupling constants with the energy scale Q according to the SM (left) and SUSY (right).

The third problem mentioned above was the so called hierarchy problem, which concerns the quadratic divergence of the Higgs mass at higher energies, since the radiative corrections to the Higgs mass contributed to the SM with a term,

$$\delta m_h^2 \simeq \mathcal{O}(\frac{\alpha}{\pi})\Lambda^2, \tag{2.4}$$

which has to be canceled by fine tuning, i.e. a tuning where m_h^2 is 36 orders of magnitude lower than δm_h^2 (obtained from the radiative corrections). With identical interactions this unreasonable tuning cancels, since SUSY implies a bosonic partner for every fermion and vice versa. The

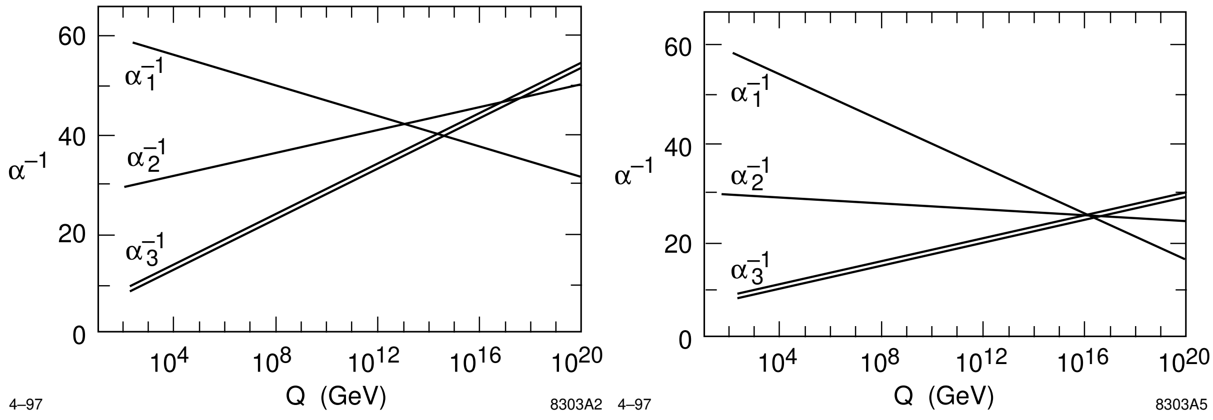

Figure 2.1: The convergence of the gauge coupling constants with increasing Q according to the SM (left) and SUSY (right) respectively. The figures show the possibility of gauge coupling unification in a SUSY theory which is not the case in the SM [5].

obtained radiative corrections in SUSY equals,

$$\delta m_h^2 \simeq \mathcal{O}(\frac{\alpha}{\pi})(m_B^2 - m_F^2), \tag{2.5}$$

where m_B is the mass of the SUSY partner boson to the SM fermion with mass m_F. Equation 2.5 shows that the Higgs mass corrections are naturally small if the bosonic SUSY partner is not too heavy compared to the SM fermion mass. This imply that in order to get rid of the hierarchy problem the mass difference should be,

$$|m_B^2 - m_F^2| < \mathcal{O}(1)\ \mathrm{TeV}^2/c^4. \tag{2.6}$$

This is the main argument for why the SUSY particle masses should be in the order of a TeV$/c^2$, since this would automatically remove the hierarchy problem.

2.2 The Sparticle Mass Spectrum

The sparticle mass spectrum can be determined by renormalization from the SUSY parameters at the GUT scale. Figure 2.2 shows the mass evolution as a function of Q from the gaugino and sfermion masses at the GUT scale ($m_{1/2},\ m_0$).

The gaugino masses at the EW scale (which will be investigated more in detail in the next sections) are determined from the unmixed gaugino mass parameters at the EW scale, $M_1,\ M_2,\ M_3$, corresponding to $U(1),\ SU(2)$ and $SU(3)$. They all originates from $m_{1/2}$, but obtains different values due to the different evolution of their coupling constants. The relation between M_1 and M_2 is of special interest for the chargino search, since they are needed to calculate the chargino and neutralino states and under the mass unification assumption these have the relation

$$M_1 = \frac{5}{3}\tan^2\theta_W M_2 \simeq \frac{1}{2}M_2. \tag{2.7}$$

In this equation θ_W is the weak mixing angle and from the renormalization the relation to $m_{1/2}$ is found to be $M_2 \simeq 0.8m_{1/2}$.

The evolution of the sfermion masses is also shown in figure 2.2. The masses of the first family of sleptons at the EW scale are approximately,

$$m_{\tilde{e}_L}^2 = m_0^2 + 0.45m_{1/2}^2 - 0.27m_Z^2\cos 2\beta, \tag{2.8}$$

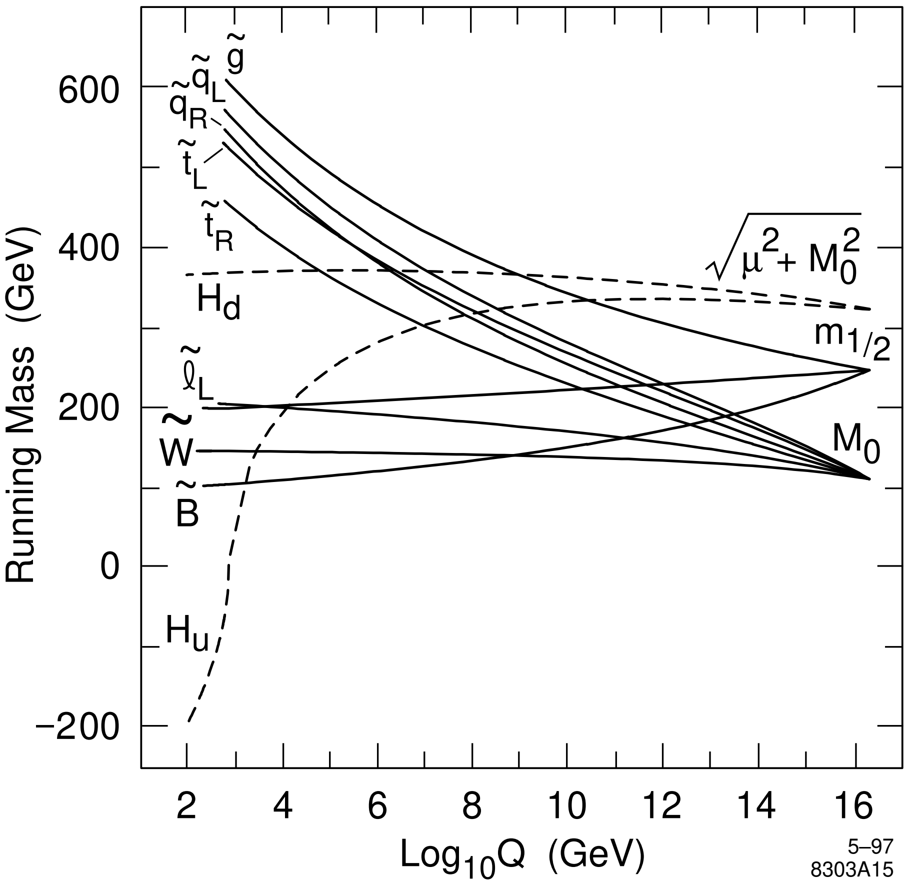

Figure 2.2: The evolution of the sparticle mass spectrum as it is renormalized from the unification scale [5].

$$m^2_{\tilde{\nu}_L} = m_0^2 + 0.45 m^2_{1/2} + 0.50 m_Z^2 \cos 2\beta, \tag{2.9}$$

$$m^2_{\tilde{e}_R} = m_0^2 + 0.15 m^2_{1/2} - 0.23 m_Z^2 \cos 2\beta. \tag{2.10}$$

and it can be seen that the $\tilde{e}_L$ is normally heavier than the $\tilde{e}_R$. Since the mass evolution is proportional to the running gauge couplings, the $\tilde{q}_{R,L}$ obtains higher masses than the sleptons at low energies. The sfermions could, however, also appear as mixtures between the $\tilde{f}_L$ and $\tilde{f}_R$ particles (like the gauginos), giving rise to two sfermion mass eigenstates for each sfermion type,

$$\tilde{f}_1 = \tilde{f}_L \cos\theta_{\tilde{f}} + \tilde{f}_R \sin\theta_{\tilde{f}}, \quad \tilde{f}_2 = -\tilde{f}_L \sin\theta_{\tilde{f}} + \tilde{f}_R \cos\theta_{\tilde{f}}. \tag{2.11}$$

This mixing is proportional to the fermion Yukawa couplings, hence related to the mass of the SM partners, and for this reason the mixing only becomes relevant for the third generation of squarks. The sleptons therefore remains very close to the unmixed states and the sfermion mixing will not be affecting the chargino analysis presented here. It can be noted that due to the mixing, the stop or sbottom could still be relatively light, even though the $\tilde{q}_{R,L}$ are normally heavier than the other sparticles.

2.2.1 The Chargino

The chargino mass terms in the supersymmetric Lagrangian appears like

$$\Delta\mathcal{L} = -c\ (\psi_k^-)^T\ M^c\ \psi_l^+ \tag{2.12}$$

where $\psi_k^{\pm}$ corresponds to the gaugino bases

$$\psi_k^+ = (-i\tilde{W}^+,\ \tilde{H}_2^+) \text{ and } \psi_k^- = (-i\tilde{W}^-,\ \tilde{H}_1^-). \tag{2.13}$$

and M^c to the chargino mass matrix,

$$M^c = \begin{pmatrix} M_2 & \sqrt{2}m_W \sin\beta \\ \sqrt{2}m_W \cos\beta & \mu \end{pmatrix}. \tag{2.14}$$

The gaugino eigenstates are related to the chargino mass eigenstates by $\tilde{\chi}_k^+ = V_{kl}\psi_l^+$ and $\tilde{\chi}_k^- = U_{kl}\psi_l^-$. Here the rows in the 2×2 eigenstate matrix V corresponds to the chargino composition of the positively charged chargino 1 and 2 respectively. Hence the matrix U refers to the negatively charged chargino. The chargino mass eigenstates and eigenvalues can be computed by diagonalizing the matrix 2.14 according to

$$m_{\tilde{\chi}_k^+}\delta_{kl} = U_{km}^* V_{ln} M_{mn}^c \tag{2.15}$$

and the analytical solution gives the following chargino masses from the parameter M_2, $\tan\beta$ and μ:

$$m_{\tilde{\chi}_i^+}^2 = \frac{1}{2}[M_2^2 + \mu^2 + 2m_w^2 \tag{2.16}$$

$$\mp\sqrt{(M_2^2 - \mu^2)^2 + 4m_W^4 \cos^2 2\beta + 4m_W^2(M_2^2 + \mu^2 + 2M_2\mu\sin 2\beta)}$$

Where $i = 1$ and $i = 2$ ($\tilde{\chi}_i^+$) corresponds to the light and heavy chargino mass eigenstates. Due to the eigenvalue relation between the SUSY parameters (M_2, $\tan\beta$, μ) and the chargino composition, two extreme cases can be identified. The first is when $M_2 >> \mu$ since then the lightest chargino evolves towards a pure higgsino composition, with increasing M_2 for a fixed μ. The second is the opposite case, when $M_2 << \mu$, since then the lightest chargino becomes wino dominated (also referred to as gaugino dominated). Since the chargino composition affects how the chargino couples to other particles, these effects are important for the phenomenological signature of the chargino.

2.2.2 The Neutralino

The neutralino mass and composition is obtained in an similar way to the chargino, with the difference that there are four neutralinos which are linear combinations of a four gaugino base

$$\psi_l^0 = (-i\tilde{\gamma},\ -i\tilde{Z},\ \cos\beta\tilde{H}_1^0 - \sin\beta\tilde{H}_2^0,\ \sin\beta\tilde{H}_1^0 + \cos\beta\tilde{H}_2^0). \tag{2.17}$$

The neutralino mass matrix (according to the photino, zino, higgsino base chosen) corresponds to

$$M^n = \begin{pmatrix} M_1\cos^2\theta_W + M_2\sin^2\theta_W & (M_2 - M_1)\cos\theta_W\sin\theta_W & 0 & 0 \\ (M_2 - M_1)\cos\theta_W\sin\theta_W & M_2\cos^2\theta_W + M_1\sin^2\theta_W & m_Z & 0 \\ 0 & m_Z & \mu\sin 2\beta & -\mu\cos 2\beta \\ 0 & 0 & -\mu\cos 2\beta & -\mu\sin 2\beta \end{pmatrix} \tag{2.18}$$

and is used to determine the neutralino masses and compositions by solving the eigenvalue problem

$$m_{\tilde{\chi}_k^0}\delta_{kl} = N_{km}N_{ln}M_{mn}^n. \tag{2.19}$$

The rows in the 4×4 N matrices contains the neutralino eigenvectors which relates the gaugino bases to the neutralino eigenstates: $\tilde{\chi}^0_k = N_{kl}\psi^0_l$. Since this is a 4×4 matrix eigenvalue problem the neutralino mass solutions are a bit more complex than for the chargino and will not be discussed further here. The composition of the lightest neutralino behaves, however, in the same way as the lightest chargino under the two extreme cases discussed above and for that reason $M_2 << \mu$ is often called the **gaugino region** and $M_2 >> \mu$ the **higgsino region**, since both the lightest chargino and neutralino are dominated by their corresponding gaugino and higgsino parts.

In the SUGRA scenario, the lightest neutralino is always lighter than the lightest chargino and from figure 2.2 one can see that it normally also is the LSP (always for what concerns the analysis presented here). Since R-parity is assumed to be conserved all other SUSY particles produced in e^+e^- collisions will hence decay in one way or another into SM particles and a $\tilde{\chi}^0_1$, which will escape detection in the experiment.

2.3 The Phenomenology

The phenomenological signature of the chargino was computed under the assumptions described in the previous sections and the chargino results are valid under the following model assumptions:

- The lightest neutralino, $\tilde{\chi}^0_1$, is the LSP (SUGRA);
- R-parity is conserved. Implying chargino pair production and stable LSP;
- The gaugino and sfermion masses are unified at the GUT scale ($m_{1/2}$, m_0);
- The sfermions are heavy ($m_0 = 1000$ GeV/c^2);
- The mass difference $\Delta m \geq 3$ GeV/c^2 (explained below).

The heavy sfermion constraint can be relaxed in some cases, which is described in section 5.4.

2.3.1 The Chargino Cross Section

Since the supersymmetric partners to the charged SM gauge bosons have exactly the same quantum numbers, except for the spin, as the SM particles, the only new information needed to determine the chargino pair production cross section is the chargino mass and the chargino mixing. The possible chargino pair production cross section, in e^+e^- collisions, is obtained at tree level by the two Feynman diagrams in figure 2.3.

The first important remark about the chargino cross section is that the t-channel sneutrino diagram contribute with a destructive interference. The sneutrino propagator implies that the diagram will have a greater influence, hence lower the cross section more, with a decreasing sneutrino mass. For the s-channel diagram one should keep in mind that this search is made for a chargino with a mass significantly larger than $m_Z/2$ and for that reason no on-shell Z will be produced due to initial state radiation (ISR), as in many SM processes.

Only the photon couples with the same strength to the charginos as to SM particles, due to the same electric charge. The coupling strength between the Z and the charginos as well as for the sneutrino–chargino–electron coupling is given by

$$g^L_{Z\tilde{\chi}^+_j\tilde{\chi}^-_i} = -V_{i1}V^*_{j1} - \frac{1}{2}V_{i2}V^*_{j2} + \delta_{ij}sin^2\theta_W \tag{2.20}$$

$$g^L_{e\tilde{\nu}\tilde{\chi}^\pm_i} = V_{i1} \tag{2.21}$$

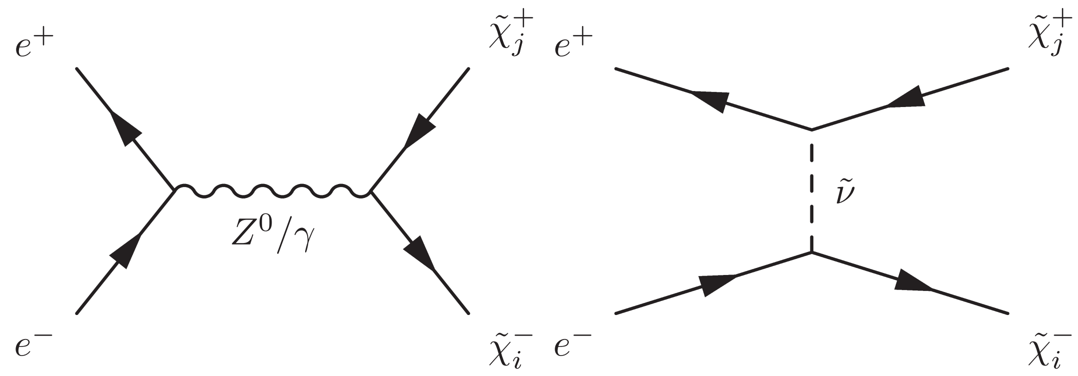

Figure 2.3: The two Feynman diagrams contributing to the chargino pair production amplitude at tree level.

Here V_{i1} corresponds to the wino composition of the chargino of type i (1 or 2) and V_{i2} corresponds to the higgsino part. The right handed coupling, $g^R_{Z\tilde{\chi}_j^+\tilde{\chi}_i^-}$, is obtained by changing the eigenvectors V to the U vectors presented in section 2.2.1. In the equations above one sees that the Z couples both to the gaugino (wino) and the higgsino part of the chargino whereas the sneutrino only couples to the gaugino part. This gives the effect that the negative interference from the t-channel diagram decreases with an increasing higgsino part and for a higgsino dominated chargino it becomes very small. If the sneutrino is heavy enough, the t-channel diagram gives a negligible contribution and the chargino pair cross section is highest for a gaugino like chargino since the remaining Z coupling becomes stronger.

The chargino search presented here is made under the assumption of heavy sfermions ($m_0 =$ 1000 GeV/c^2), which implies a heavy sneutrino, partly due to the negative interference effect of the sneutrino. This constraint can, however, be relaxed in some parts of the SUSY parameter space where the cross section gets insensitive to the contribution from the t-channel diagram. This will be explained further in section 5.4.

2.3.2 The Decay Channels

Finally one needs to know how the chargino decay into the final state SM particles and the LSP ($\tilde{\chi}_1^0$). The diagrams describing the chargino decays are shown in figure 2.4. The chargino can either decay into two fermions and a neutralino, through a W or a sfermion ($\tilde{f} = \tilde{q},\ \tilde{\ell},\ \tilde{\nu}$). The sfermion decay processes gets suppressed with increasing sfermion masses and this is the other reason (together with the negative interference from the sneutrino diagram) why the analysis here is made under the assumption of heavy sfermions, $m_0 = 1000$ GeV/c^2 . Hence the chargino is mostly decaying through the W process and in this scenario a produced chargino pair give rise to final states similar to the ones from SM WW production, but with two additional neutralinos.

Since the neutralino escapes detection, a very important quantity for how a chargino would appear in the experiment is the mass difference between the chargino and the lightest neutralino. This is what will be referred to as Δm and it is defined as

$$\Delta m = m_{\tilde{\chi}_1^\pm} - m_{\tilde{\chi}_1^0}. \tag{2.22}$$

This mass difference reflects the visible energy in the chargino event and for that reason strongly affects the signal efficiency of the analysis. For a very high Δm, the chargino signal gets almost identical to SM WW events and these contribute with an almost irreducible background. In the high Δm region the next–to–lightest neutralino often becomes kinematically accessible (mainly

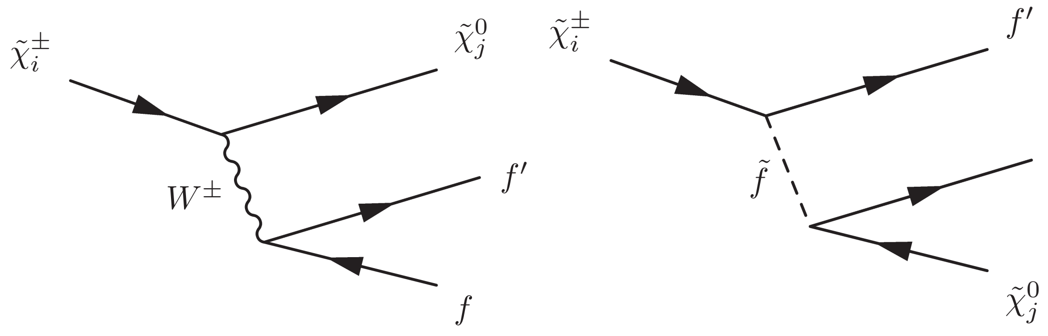

Figure 2.4: The diagrams for chargino decays if R-parity is conserved.

in the region where M_2 and μ are both small) and the branching ratio for the radiative neutralino cascade decay, like the two shown in figure 2.5, becomes large [8]. This makes it possible to use radiative chargino final states in order to better distinguish a possible chargino signal from the SM background in the problematic high Δm region. For this radiative process, the Δm is redefined as

$$\Delta m = m_{\tilde{\chi}_1^{\pm}} - m_{\tilde{\chi}_2^0}. \tag{2.23}$$

The $\tilde{\chi}_2^0$ can of course also decay into a $\tilde{\chi}_1^0$ and a Z through an ordinary two body decay.

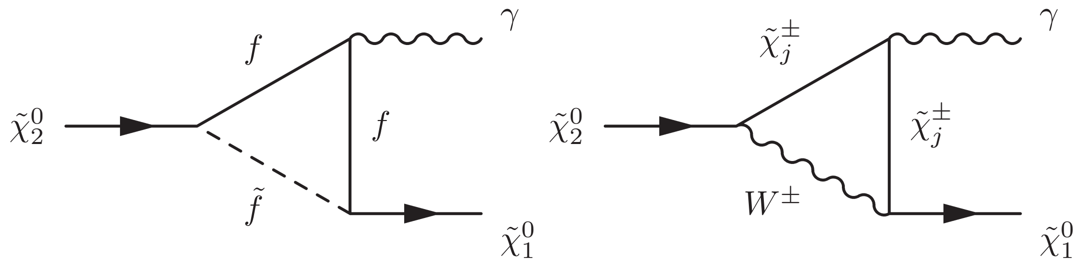

Figure 2.5: Two example diagrams for radiative neutralino cascade decays. Other similar diagrams do also contribute, which contains other particles in the loop.

In this analysis, the chargino signal event contribution was based on pair produced $\tilde{\chi}_1^{\pm}$ which decay into two WW and either, $\tilde{\chi}_1^0\ \tilde{\chi}_1^0$, $\tilde{\chi}_1^0\ \tilde{\chi}_2^0$ or $\tilde{\chi}_2^0\ \tilde{\chi}_2^0$, where the $\tilde{\chi}_2^0$ decay into a $\tilde{\chi}_1^0$ and a γ or Z, as discussed above. There are parts of the parameter space where the $\tilde{\chi}_2^{\pm}$ is kinematically accessible, but in this analysis the only signal contribution from $\tilde{\chi}_2^{\pm}$ production taken into account was $\tilde{\chi}_2^{\pm}\ \tilde{\chi}_2^{\pm}$ production when the lightest and next–to–lightest charginos are mass degenerate. In that case the decay for $\tilde{\chi}_2^{\pm}$ into a $\tilde{\chi}_1^{\pm}$ is suppressed and the $\tilde{\chi}_1^{\pm}\ \tilde{\chi}_1^{\pm}$ and $\tilde{\chi}_2^{\pm}\ \tilde{\chi}_2^{\pm}$ give rise to the same kind of final states. From these chargino processes and decays the following signal final states can be produced:

$$\begin{aligned} \tilde{\chi}_1^+\tilde{\chi}_1^- \to W^+W^-\ \tilde{\chi}_{1(2)}^0\tilde{\chi}_{1(2)}^0 &\to ff\ f'f'\ \tilde{\chi}_1^0\ \tilde{\chi}_1^0\ (Z\ /\ \gamma)\ (Z\ /\ \gamma) \\ &\to ff\ f'f' \quad \tilde{\chi}_1^0\ \tilde{\chi}_1^0 \quad (f''f''\ /\ \gamma) \quad (f'''f'''\ /\ \gamma) \end{aligned} \tag{2.24}$$

The different final states can be divided into four different decay channels defined as:

- **Hadronic**, corresponds to the decay channel where both the charginos have decayed into hadronic final states. In this decay channel all the decay products consists of hadronic matter.

- **Semi–leptonic**, refers to the decay channel where one chargino has decayed into a lepton–neutrino pair, but where also hadronic decay products are present.
- **Leptonic**, refers to the decay channel where all final state particles are leptons.
- **Radiative**, this decay channel refers to chargino decays where the final state particles contains at least one photon produced in a $\tilde{\chi}_2^0$ cascade decay.

Chapter 3

Experimental Facilities and Simulations

3.1 The LEP Collider

The DELPHI experiment was built around one of the collision points along the large electron positron accelerator ring (LEP) [9] at CERN just outside Geneva, Switzerland. LEP accelerated electrons and positrons, by superconducting RF-cavities, in opposite directions in a circular beam-pipe at a pressure close to vacuum. The beam was kept in its orbit by a magnet system which contained 4184 magnets mounted along the LEP ring. The electrons and positrons went through five different accelerators, which accelerated them to an energy of 20 GeV , before they were injected into LEP, which accelerated them up to their highest energy before forcing them into head-on collisions at four places along the ring. The LEP collider is the largest particle accelerator ever built and it had a circumference of 27 km. Figure 3.1 illustrates the CERN accelerator complex with the successive chain of accelerators from the production to the injection of the electron/positron beam. LEP was located 100 m below ground which was necessary due to the high level of synchrotron radiation produced by bending the beams.

During the first years, between 1989 and 1995, LEP was running with a center–of–mass energy around m_Z in order to measure the Z-width and related electroweak physics and that period of time is called the LEP1 period. After 1995 the energy was increased successively with the highest collision energy achieved in the last year of running (2000) at $\sqrt{s} = 208.8$ GeV and this running period was called LEP2. Figure 3.2 shows the delivered luminosity, as a function of time, for each year and the LEP accelerator delivered an integrated luminosity of 1 fb^{-1} during the total period of running. The figure also shows the excellent performance during the last two years, 1999 and 2000, which corresponds to the data used for the chargino search presented here.

3.2 The DELPHI Experiment

DELPHI was a multi-purpose detector which was running from 1989 to November year 2000 at LEP. It was designed to cover the full 4π solid angle and to contain many different subdetector systems in order to provide good particle identification and high quality measurements. For details about the DELPHI detector and its subdetectors the reader is referred to [10] and here will only be given a brief description.

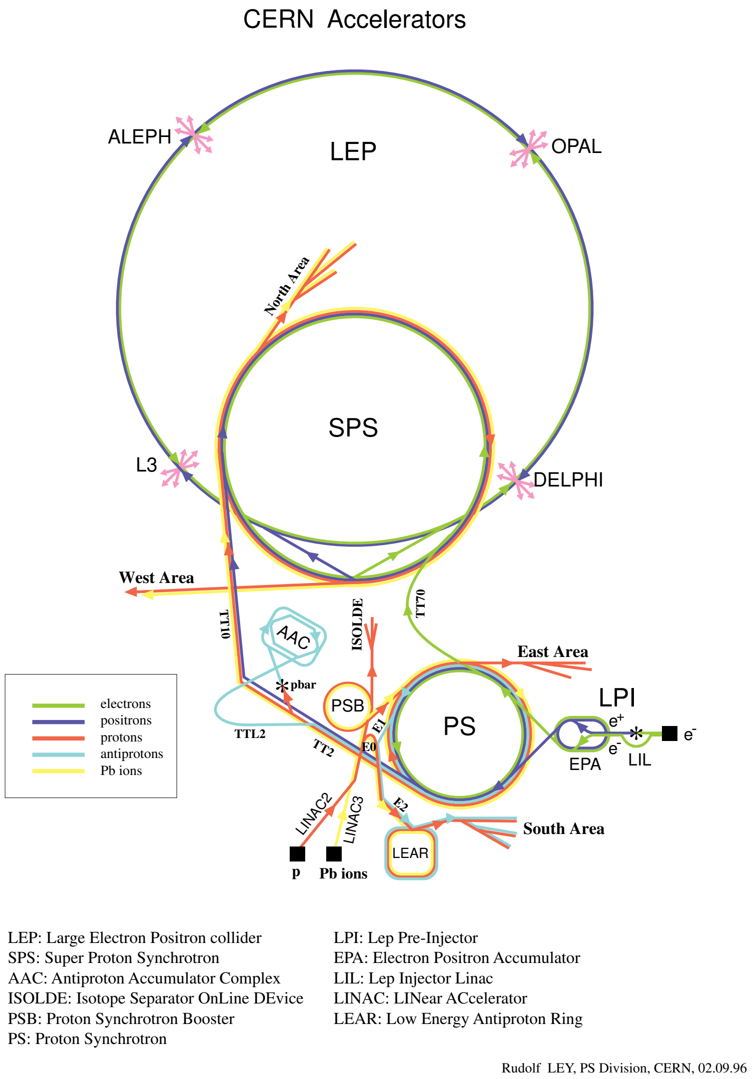

Figure 3.1: The accelerator chain at CERN. The figure shows the successive acceleration of the electron/positron before being injected into the LEP accelerator.

3.2.1 The Subdetector Systems

Figure 3.3 shows a schematic overview of the DELPHI experiment and its subdetectors. The DELPHI coordinate system has its origin in the middle of the detector, where the e^+e^- interaction point (IP) is, and is defined such that the **z**-axis is parallel with the beam-pipe and pointing in the same direction as the electron beam. The **x**-axis points towards the center of LEP and **y** is pointing upwards. In polar coordinates, the θ-angle is the polar angle relative to the z-axis, ϕ is the azimuthal angle around z and the radius is defined as $\mathbf{r} = \sqrt{\mathbf{x^2} + \mathbf{y^2}}$. In figure 3.3 one can see that the DELPHI detector was divided up into one barrel region and two endcap regions and that these regions had an almost identical subdetector structure. The endcaps could be separated from the barrel in order to gain access to the subdetectors during the winter when LEP was not operating. In general, the tracking detectors were placed closest

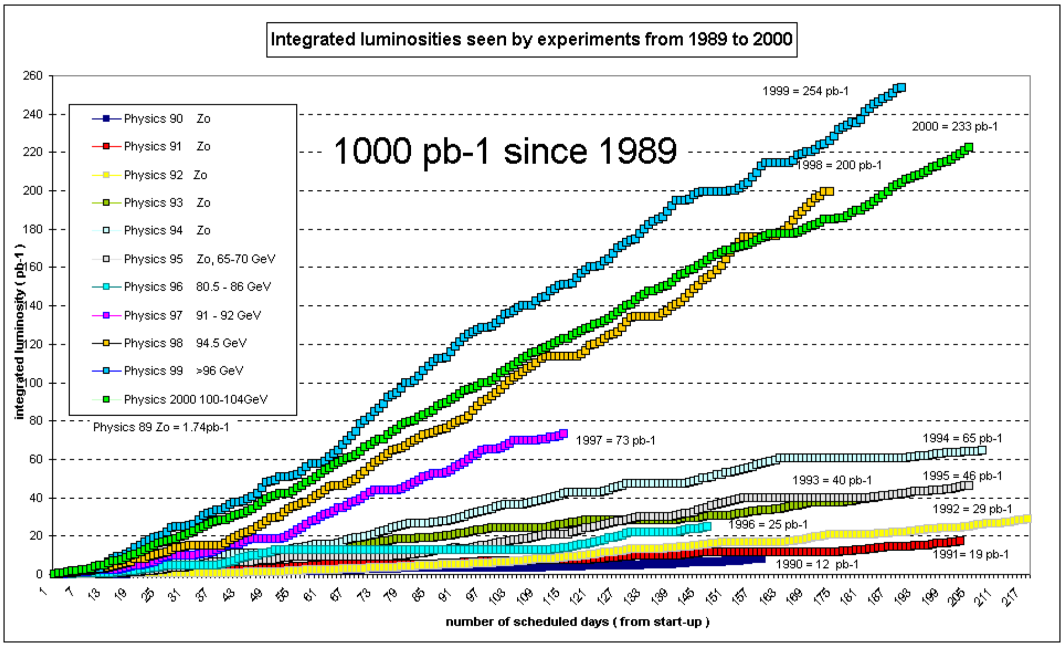

Figure 3.2: The luminosity delivered by the LEP accelerator during the period 1989 to year 2000.

to the interaction point followed by the electromagnetic and hadronic calorimeters, respectively, which were surrounded by the muon identification detectors. In DELPHI one could identify the particles and determine their properties from how far they were able to propagate through the experiment together with the deposited energy and track information. In some regions, such as at $\theta = 90°$ and in the cable ducts between the barrel and forward regions (about $40°$ and $140°$ in θ), there was not full coverage and for that reason extra scintillation counters were installed to detect activity in these regions and hence provide complete hermeticity.

Since the tracking detectors had to be operated in a magnetic field in order to get particle momentum information, a superconducting coil was installed at a radius where it could provide an uniform 1.23 Tesla magnetic field parallel to the z-direction.

Because of the different decay channels of the chargino, the signal signature can vary a lot and hence the chargino analysis depends strongly[1] on both the subdetectors most important for hadronic final states (such as the hadron calorimeter) as well as the subdetectors most related to leptonic final states (such as the EM-calorimeters and the muon detectors). Since the chargino signal is characterized by missing energy, due to the escaping LSP, the chargino analysis is also very depending on the hermeticity of the detector and hence the hermeticity taggers were important in this analysis. The main tracking detector in DELPHI had a part which did not work during the last months of year 2000, which implied a larger dependence on the remaining tracking systems. More details about the most important detectors (which will be referred to later on) for the chargino analysis are presented below.

- **Tracking**. The DELPHI detector contained four main tracking detectors called, the VD, the ID, the TPC, the OD, the FCA and the FCB. The locations of the detectors are given in figure 3.3, with the VD closest to the interaction point.

  - **VD**. The **V**ertex **D**etector was a silicon tracker mounted closest to the beam-pipe. It

[1] This means that they are not only used as veto of some final states, but they are used to measure properties of the events.

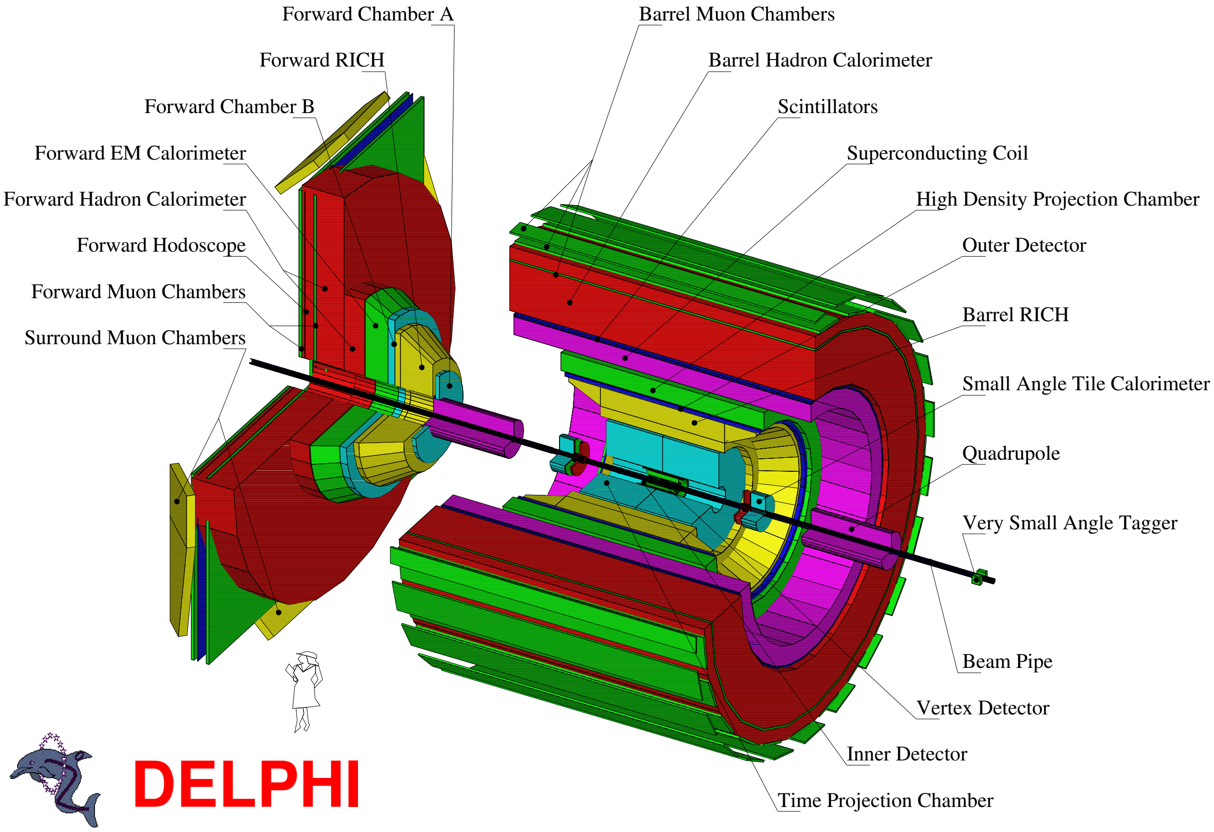

Figure 3.3: A schematic overview of the DELPHI experiment and its subdetectors. It shows the general structure of the DELPHI subdetectors, where the tracking systems are closest to the IP followed by the calorimeters and the muon identification detectors.

consisted of one barrel part and one so called very forward part. The barrel part was built from three cylindrical silicon strip detector layers at the radial distances 6.3, 9.0 and 10.9 cm and had a length of 48 cm. A very forward part was added as an upgrade to improve the angular coverage down to $10°$ ($170°$). This detector consisted of two cone shaped layers of silicon pixel detectors, mounted between the beam-pipe and the outer and inner barrel layers. The very forward part also contained two rings of strip detectors mounted close to the beam-pipe at a larger z than the pixel cones. All silicon strip modules contained detector elements with opposite strip direction and the two cones at each side were rotated with respect to each other to cover cracks.

– **ID**. The **I**nner **D**etector was mainly a jet (drift) chamber, but it also contained five outer layers of straw (drift) tubes. The jet chamber was located at a radial distance of 12-23 cm and covered an angular region of $15° \leq \theta \leq 165°$. Five cylindrical layers of straw tubes were located outside the jet chamber, containing 192 tubes per layer. These were used together with the jet chamber to provided $R\phi$ information, but they were also used in the DELPHI trigger system.

– **TPC**. The **T**ime **P**rojection **C**hamber was the main DELPHI tracker and consisted of two cylindric volumes containing a 80% Ar/20% CH_4 gas mixture at a pressure of 1 atm. The end-plates of each cylinder were divided into six sectors where each sector was equipped with 192 sense wires and 16 circular pad rows with equal spacing, which provided 16 space points for a particle passing through. The TPC could measure radial positions between $40 < r < 110$ cm and covered the angular region $39^\circ \leq \theta \leq 141^\circ$. The angular region could be extended further if it was not required that the particle crossed all the 16 pad rows. The angular coverage was for example $20^\circ \leq \theta \leq 160^\circ$ for particles that crossed at least three pad rows.

- **OD**. The **O**uter **D**etector was a five layer drift tube detector. The OD was located at a radius between 197 to 206 cm and covered a polar angle of $42^\circ \leq \theta \leq 138^\circ$. The drift tubes could in addition to the $R\phi$ determination also measure the z coordinate by timing the signal at the ends of the anode wires (limited streamer mode).

- **Calorimetry**. In DELPHI the calorimetry was divided up into three different electromagnetic calorimeters and one hadron calorimeter. The electromagnetic calorimeters were called STIC, FEMC and HPC and they covered different regions in θ.

  - **STIC**. The **S**mall angle **TI**le **C**alorimeter was a lead-scintillator electromagnetic calorimeter where the scintillation light was read out by longitudinal wavelength shifting fibers. The lead-scintillator layers were successively rotated in order to prevent particles to escape trough the fiber holes. The STIC calorimeter consisted of two cylindrical detectors mounted close to the beam pipe on each side of the interaction point. Their main purpose was to determine the luminosity from Bhabha events, but they were also used in various analysis. The STIC calorimeter covered the angular region between $1.6^\circ \leq \theta \leq 10.6^\circ$.
  - **FEMC**. The **F**orward **E**lectro**M**agnetic **C**alorimeter was a lead glass calorimeter where the Cherenkov light was read out by photomultipliers attached to the lead glass. It consisted of 4532 truncated, pyramid shaped lead glass blocks which were pointing towards the interaction point, with a 1° tilt in order to prevent particles to escape in the cracks between the blocks. The FEMC calorimeters were located at a distance $|z| = 284$ cm from the interaction point and covered the polar angles $8^\circ \leq \theta \leq 35^\circ$ ($145^\circ \leq \theta \leq 172^\circ$).
  - **HPC**. The **H**igh density **P**rojection **C**hamber was the barrel electromagnetic calorimeter, which was mounted in front of the superconducting solenoid. The HPC consisted of 144 modules mounted in six rings, where each module was an individual TPC containing 41 layers of lead to convert the electrons and photons into particle showers. The HPC was located at a radius of 208 to 260 cm and covered $40^\circ \leq \theta \leq 140^\circ$.
  - **HAC**. The **HA**dron **C**alorimeter consisted of one barrel part and two forward parts, covering almost the full 4π solid angle ($11^\circ \leq \theta \leq 169^\circ$). The calorimeter was situated in the magnet return yoke, hence located behind the superconducting coil and contained 20 (19 in the end-caps) layers of drift tubes. These were used in the limited streamer mode to measure the shower properties.

- **MUC**. The **MU**on **C**hambers all consisted of drift chambers which were located on the outside of the DELPHI detector and they were divided up into three parts, the barrel, the forward and the surrounding chambers (which covered the 40° (140°) region). Only muons with a momenta over 2 GeV/c were expected to go through the hadron calorimeter and for that reason most of the signals in the drift chambers could be associated with a muon.

- **Hermeticity taggers**. The hermeticity taggers were used to monitor the activity in the regions where there was a lack of electromagnetic calorimetry. The taggers were lead-layers followed by scintillator counters which were read out by wavelength shifting fibers. There was three regions where these were located. The first was in the region of the cable ducts between the FEMC and the HPC (called the 40°-taggers). The second was in the 90° region where the HPC had a gap (called the 90°-taggers) and the last covered cracks in ϕ between the HPC and the cryostat (called the phi-taggers).

During the first of September in year 2000 there was a short circuit in the TPC sector 6. One of the sense wires became loose and touched the neighboring sense wire. This result was in that the whole sector 6 became useless. Since there was no possibility to get access to the TPC during the remaining part of the running of LEP (which ended the first of November year 2000) the last 60 pb^{-1} of data, at the highest energy, was recorded without the information from sector 6 in the TPC. Due to this, the detector simulation, the event reconstruction and processing of data and MC had to be totally re-made in order make a proper analysis of the data with no information from the TPC sector 6. The tracking in the sector 6 region was in the modified reconstruction program based only on the VD, the ID and the OD.

3.2.2 The Trigger and Data Acquisition System

The DELPHI trigger system [11] consisted of four increasingly selective triggers called T1, T2, T3 and T4. T1 and T2 were hardware triggers which were synchronized with the beam cross over (BCO), whereas the T3 and T4 were software triggers which were not synchronized with the BCO. The first T1 trigger was a pre-trigger to T2 with loose criteria. Since the trigger frequency was largest for T1 it was based on the fast tracking detectors such as the various scintillator detectors, the FEMC and the barrel part of the MUC. No correlation between different detectors were taken into account in the T1. The second trigger T2 was based on the same detectors as T1 with some additions, such as the TPC, the HPC and the forward part of the MUC. The second level trigger also used coincidences between more noisy detectors. The coincidence logics for the T2 trigger is presented in [11], however a general description of the trigger requirements are:

- **Tracks**. The tracking subtrigger was based on the tracking detectors used in the T1 trigger plus the TPC. The trigger required the tracks to have a $p_{\rm t} > 1$ GeV/c in the barrel region ($29° \leq \theta \leq 151°$) and a transverse momentum $p_{\rm t} > 1.6$ GeV/c in the forward region ($11° \leq \theta \leq 33°$, $147° \leq \theta \leq 169°$).

- **e**$^-/\gamma$. The electromagnetic subtrigger used the information from the HPC and FEMC calorimeters where an energy deposition of 2 GeV respectively 2.5 GeV were required. In FEMC a lower value could be allowed if it was used in correlation with some other detector.

- μ . The muon subtrigger was mainly based on the MUC systems. The MUC trigger covered an angular region of $50° \leq \theta \leq 130°$ (the barrel detectors) and $15° \leq \theta \leq 41°$ ($139° \leq \theta \leq 165°$) (the forward detectors).

- **q** . HAC was used for the hadronic subtrigger. Three different energy thresholds were used for the HAC, corresponding to 0.5, 2 and 5 GeV and the angular acceptance was the same as the one of the HAC detector it self.

The DELPHI trigger had a high degree of redundancy which was important in order to maintain a high trigger efficiency during the long periods of running. The high redundancy did however increase the background and after the T2 trigger only about 20% of the events were interesting e^+e^- physics events. The T3 trigger was based on the same detector logic as the

T2 trigger, but used more detailed information. Since the signals from the detectors had been digitized at that stage, calibration constants could be applied which allowed for more refined cuts, e.g. on energy deposition and track directions. The T3 trigger was used to decrease the data logging frequency down to 2 Hz. After the T3 trigger the event rate was low enough to allow a more complete processing of the data by the T4 trigger. T4 was a software filter, which was running a sequential set of algorithms on the data from the individual subdetectors to decide if the event should be written to tape or be rejected. The level 4 trigger was based on a special version of the DELPHI analysis package DELANA [12], and rejected events with no tracks pointing back towards the interaction point and events without any energy deposition in the calorimeters. The trigger frequency decreased from about 700 Hz at T1 to 1.5 Hz at T4 (4.5 Hz at T2 and 2.0 Hz at T3) and after the T4 trigger the fraction of the events written to tape that originated from physics events was approximately 50%.

The trigger efficiency was in most cases very high. The trigger efficiency for electrons and muons within polar angles between $20^\circ \leq \theta \leq 160^\circ$ was consistent with 1 at the level of 10^{-4} and a single track with $p_t > 1$ GeV/c in either the barrel ($42^\circ \leq \theta \leq 138^\circ$) or the forward ($10^\circ \leq \theta \leq 32^\circ$, $148^\circ \leq \theta \leq 170^\circ$) region exceeded a trigger efficiency of 0.95. This high efficiency and the high multiplicity in hadronic final states mean that the trigger efficiency for hadronic events was very close to 1 over almost the full solid angle. There are topologies, however, with lower trigger efficiencies.

The DELPHI data acquisition system (DAS) consisted of 150 fastbus crates which were connected by an Ethernet connection to a VAX cluster. The crates were divided into partitions corresponding to the different subdetectors and the trigger. In order to minimize the dead-time after an event had occurred, the front-end was in general equipped with an event buffer. One critical task of the DAS was to switch the buffer when a new event was read out. This switch took 3 ms which introduced a 0.4% dead-time. The trigger and read out was made by software, slightly different for each subdetector and running on so called fastbus intersegment processors (FIP) in the crates. The information from the FIPs was read out by a software called the local event supervisor (LES), also running in a FIP, which transfered the information into two different buffers, the local spying and the central read out buffer. The local spying buffer was used, by a VAX station, for local monitoring or individual test of the specific subdetector. The central read out buffer was used for the main data collection stream. The central read out buffer was used to build an event (in ZEBRA data format) inside the fastbus system, i.e. the process was running in a FIP and the event information was stored in the fastbus memory. The event was only built if it had passed the level 3 trigger. The event information was then copied to the VAX cluster where the T4 filter was used to decide if the event should be stored or not. If the event passed the level 4 trigger it was sent over an optical link to the central data recording facility at CERN where it was stored on tape and after that the final reconstruction work could be performed at the local DELPHI computer farm.

3.3 The Data Samples

The data recorded during the years 1999 and 2000 was used for the DELPHI chargino analysis. Since a chargino signal would have a larger production cross section at a higher center–of–mass energy, the data recorded during the year of 2000 will not only have a higher kinematical reach than the 1999 year data, but it is also more important in the region where they both can be used, for an equal value of integrated luminosity. In order to increase the sensitivity in areas where the efficiency is low, such as in the low Δm region, there are good reasons to combine the data from 1999 and 2000. The data collected during 1999 was recorded around four different center–of–mass energies, 192, 196, 200 and 202 GeV and the total integrated luminosity was 226 pb^{-1}. The individual luminosities are presented in table 3.1.

Year	$<\sqrt{s}>$ GeV	$\mathcal{L}$ pb^{-1}
1999	192	25.9
	196	76.4
	200	83.4
	202	40.6

Year	$<\sqrt{s}>$ GeV	$\mathcal{L}$ pb^{-1}
2000	204.8	77.7
	206.5	79.4
	208	7.1
No TPC	206.3	60.1

Table 3.1: The different energy regions used in the analysis and their corresponding integrated luminosities.

The data recorded during the year 2000 was, as mentioned earlier, affected by the breakdown of sector 6 in the TPC. The data collected during year 2000 with the sector 6 working corresponded to an integrated luminosity of 164 pb^{-1} with an average center–of–mass energy $<\sqrt{s}>=$ 206 GeV. This data sample was called the C1 sample due to the C1 version of the processing that was used. The data recorded without the TPC sector 6 corresponded to 60 pb^{-1} and had a mean center–of–mass energy of $<\sqrt{s}>=$ 206 GeV, and this data was called the S1 data because of the version of the processing. In order to increase the chargino sensitivity near the kinematic limit, the C1 data was divided into three sub samples for the combination. Figure 3.4 shows how the luminosity is distributed with respect to the mean center–of–mass energy. The upper plot corresponds to the C1 data and the lower to the S1 data and the plot also shows how the three different region of the C1 data was divided with respect to the center–of–mass energy. The individual luminosities, for the year 2000 data samples, are also presented in table 3.1.

3.4 Event and Detector Simulations

In order to compare the DELPHI data to the expectation from the SM and possible new physics, Monte Carlo simulation techniques were used both to simulate the physics processes in the e^+e^- collisions and to simulate the detector response. For the SM and new physics processes, events were first generated which were then used by the detector simulation program to produce events containing the same information as the one read out from the detectors by the DAS in a real data event. This section will present the different generators used in the chargino analysis and describe the detector simulation briefly. The quark fragmentation of all the generated final states, both signal and background events, was based on `JETSET` v7.4 [13], which had been tuned to LEP1 data.

3.4.1 SM Event Simulation

For the SM background simulation 37 different processes were simulated to cover as many of the possibles background sources as possible. The background processes were classified into four fermion, two fermion and gamma-gamma background:

- **4f**. The four fermion background at LEP was dominated by double W/Z processes such as $e^+e^- \to WW$ and $e^+e^- \to ZZ$, or some kind of single W/Z process, such as $e^+e^- \to We\nu$ or $e^+e^- \to Zee$.
- **2f**. Two fermion events at LEP was normally produced through a γ/Z s-channel process or some t-channel process. In the case of a Z s-channel diagram a ISR photon can allow the Z to be on mass shell, which can have a large effect on the cross section of the process.

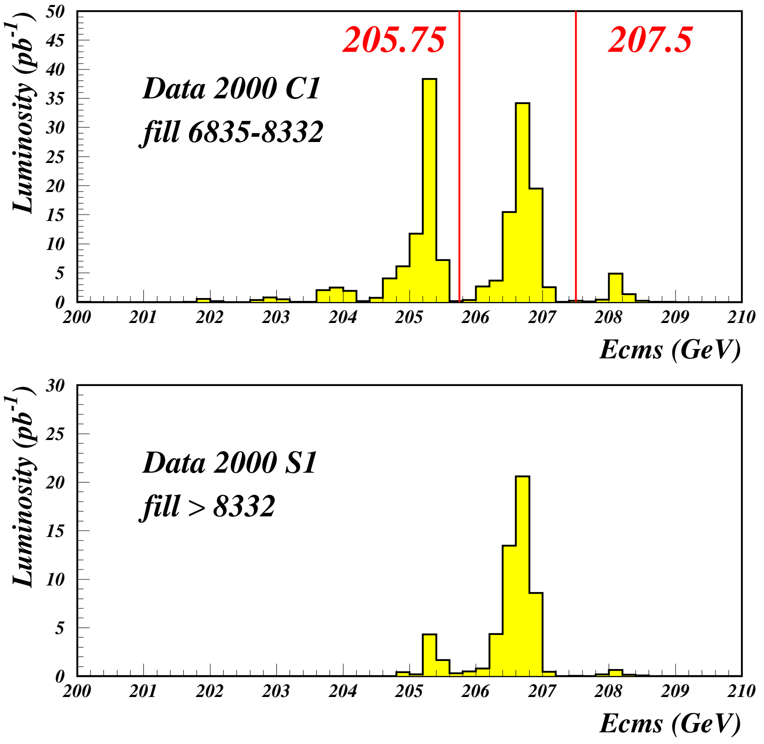

Figure 3.4: The distribution of luminosity with respect to the center–of–mass energy for the year 2000 data. The upper plot corresponds to the period with the TPC sector 6 operating and the lower to when it did not. The upper plot also shows how the data was divided into three subsamples to increase the chargino sensitivity.

- $\gamma\gamma$. The two photon (or gamma-gamma) background was considered separately, even though some of it has a four fermion final state, since it differs a lot from the other four fermion processes. Since the two photon process is described by diagrams where the interacting photons are emitted from each initial $e^{\pm}$, in a t-channel configuration, the final e^+e^- pair tend to get a very high momentum at angles close to the beam-pipe. The event topology is therefore very different for the same four fermion final states from the other four fermion background processes mentioned above.

Four different generators were used to simulate the two fermion background. For Bhabha events $e^+e^- \rightarrow e^+e^-$, the `BHWIDE` generator [14] was used, for the $e^+e^- \rightarrow \mu^+\mu^-$ background the `DYMU3` generator [15] and for the process $e^+e^- \rightarrow \tau^+\tau^-$ `KORALZ` v4.2 [16] was used. The hadronic two fermion events $e^+e^- \rightarrow q\bar{q}(n\gamma)$ were generated by `PYTHIA` v6.125 [13].

The main generator used for the four fermion SM events was `EXCALIBUR` [17]. The `GRC4F` [18] was also used for parts of phase space not covered by `EXCALIBUR`

In the chargino analysis most of the two photon events were rejected in the analysis, since they are very unlike signal events, but since the two photon cross section is very high it still represents a large fraction of the SM background (especially in the low Δm region). Since the two photon events normally has a different topology to chargino events, the selected events are from the tails of the distributions which demands a very accurate simulation by the MC generators. For this reason both the `PYTHIA` v6.143 [13] and the `TWOGAM` [19] generators were used for the hadronic final states. PYTHIA was considered as the official two photon event generator within DELPHI, but TWOGAM was also used for cross checks. In this case when a very small fraction of events from the tails is selected, one would have to generate an incredible amount of events to get a satisfactory statistics of events remaining after the selection and therefore biased samples were produced where one explicitly produced events with the characteristics of the events passing the selection. This was made for both the leptonic and hadronic final states, where the leptonic events were generated by BDKRC [20] for both the biased and unbiased samples.

In addition to these main background processes other background events, like events from QED, Compton, $e^+e^- \to \nu\nu(\gamma)$, were generated for the analysis. For all four and two fermion background processes at least 50 times the number of events corresponding to the data was generated. For the two photon background it was more problematic to generate a sample where the statistics is large after the chargino selection, but by producing the biased samples the number of generated events corresponded to at least ten times the expected number of events in the collected data.

3.4.2 SUSY Event Simulation

In the final chargino search at LEP2, signal events were generated for chargino masses above $m_{\tilde{\chi}_1^\pm} = 45$ GeV$/c^2$ and the search was performed at Δm values equal to or above 3 GeV$/c^2$. Gaugino mass unification was assumed, hence the $\tilde{\chi}^\pm - \tilde{\chi}^0$ mass relation is constrained, and all simulations were made under the assumption of heavy sfermions (m_0 = 1000 GeV$/c^2$). The chargino signal events were generated by the SUSYGEN [21] generator. The events were generated at 132 different SUSY points (M_2, $\tan\beta$, μ) within the SUGRA scenario described in the previous chapter and all decay channels described was taken into account. At each point, 3000 chargino events were generated and these points are shown in the $m_{\tilde{\chi}^\pm} - m_{\tilde{\chi}^0}$ plane in figure 3.5. Figure 3.5 shows both the points with and without the possibility of radiative cascade decays.

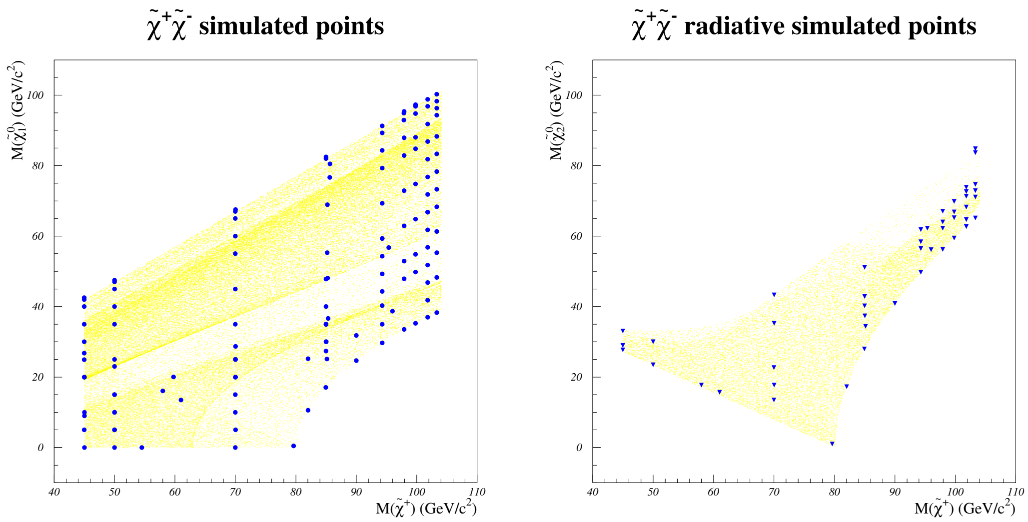

Figure 3.5: The simulated points in the SUSY parameter space, shown in the $m_{\tilde{\chi}^\pm}$ -$m_{\tilde{\chi}^0}$ plane. The plots corresponds to the points where the radiative cascade decay is possible (right) or not possible (left). Note that due to the different definitions of Δm the plots have $m_{\tilde{\chi}_2^0}$ and $m_{\tilde{\chi}_1^0}$ on the vertical axis.

The points where chosen such as to take into account the strong dependence of the signal topology on the Δm value and the gaugino compositions, which can be determined from the

SUSY parameters M_2, μ and $\tan\beta$ together with the assumption of gaugino mass unification. Points with a possibility of radiative cascade decays $\tilde{\chi}_2^0 \rightarrow \tilde{\chi}_1^0\gamma$ were also simulated. The radiative branching ratio is largest for small M_2 and μ values, which corresponds to relatively large Δm values and this feature of the branching ratio is the reason for the distribution of SUSY points in the radiative case, in the $m_{\tilde{\chi}^\pm}$ -$m_{\tilde{\chi}^0}$ plane. As can be seen in the plots, the non-radiative and radiative points are shown as functions of the $\tilde{\chi}_1^0$ and $\tilde{\chi}_2^0$ mass respectively, due to the different definition of Δm.

3.4.3 Simulation of the DELPHI Detector

DELSIM [22] is the simulation program used to simulate the detector response of the DELPHI detector. It was developed by the DELPHI collaborators after the decision in 1982 that the DELSIM program should not be based on the `GEANT` simulation package which the other LEP experiments used.

The DELSIM program was made in such a way that it is possible to interface it with any event generator providing the events are in the standard LUND common LUJETS format. This made it convenient to use with most event generators "on the market".

DELSIM simulated the propagation of the final state particles through the detector and the production of secondary particles inside the detector from interactions with the material in DELPHI. DELSIM also simulates the detector response to these particles and even the electrical signals that would have been read out in the real subdetectors. Many physical processes were taken into account (such as ionization, bremsstrahlung, multiple scattering etc.) together with the magnetic field in order to compute the particle trajectories and their interactions with the subdetectors and other material.

The output from the DELSIM simulation was stored in the same format as the raw data read out by the DELPHI DAS.

All background and signal events in the chargino analysis were processed through the full DELSIM detector simulation.

3.5 Reconstruction and Identification

3.5.1 DELANA

DELANA [12] was the DELPHI reconstruction program which was used for event reconstruction both of simulated and real data. The DELANA program started with an initialization of the detector dependent software, in which it got the proper calibration values like pedestals and machine running conditions.

The reconstruction was then made in two steps. In the first step, the reconstruction was made individually for the different subdetectors. The signals read out from the detectors were calibrated and local pattern recognition might be performed. The output from the first step in the reconstruction were space point hits in a tracker, energy clusters in the calorimeters and track segments in the TPC etc. After the first step, a global track reconstruction was made, where a set of algorithms were used to combine the information from the different tracking detectors and where they were extrapolated through the DELPHI detector. The tracks were then associated with energy clusters in the calorimeters and hits in the MUC and other subdetector signals. Also so called neutral tracks were extrapolated from the energy clusters with no associated track.

Finally this information from the event reconstruction was written to a data summary tape (DST), which were used for the proceeding physics analysis.

3.5.2 SUSANA

A common analysis framework to all the (SUGRA) SUSY searches was made in order to make it easier for cross checks and combinations of the results. This framework was called SUSANA and contained the particle identification and isolation criteria which was used in the different SUSY searches. A loose general preselection was also made at the SUSANA level and for the SM and data events passing that selection the values of a defined set of observables were stored in ntuples. Equivalent ntuples were also produced for the SUSY signal in the various searches and from these ntuples the final signal specific analysis could be performed.

In the SUSANA framework the acceptance of charged and neutral particles were constrained by the following quality requirements. For the charged particles a momentum of $p > 100\mathrm{MeV}/c$ was required and for particles with $p > 0.75\sqrt{s}$ the relative momentum error had to be $\Delta p/p < 1$. The accepted charged particles should also have an extrapolated trajectory within 5 cm in $r\phi$ from the main vertex and 10 cm/$\sin\theta$ in z. Similar, but more stringent, criteria were used for charged particles with an extrapolated trajectory through the TPC acceptance, but with no signal in the TPC. The energy threshold for an electromagnetic cluster to be associated with a particle varied between 300-500 MeV depending on the region of the detector and for the hadronic calorimeter the cluster energy threshold was 900 MeV. An energy cluster with energy over the threshold and with no associated charged particle was classified as a neutral particle. Additional cuts to remove noise caused by radioactivity in the calorimeters and to reject background from cosmic ray showers were also applied.

The particle identification was made by various algorithms. For the jet reconstruction the `LUCLUS` [13] algorithm was used to associate the hadronic tracks in the detector to hadronic jets, corresponding to the hadronization of quarks or gluons produced in the e^+e^- collision. The `LUCLUS` algorithm is based on a defined separation distance in four-momentum space (d_{join}). The jet reconstruction is made by grouping together the hadronic tracks in the event until the d_{join} separation, for the individual jets, exceeds a specified value and in the chargino analysis the value was set to $d_{join} = 10$ GeV/c .

For the electron and photon identification the `REMCLU` [23] package was used. The identification of an electron or a photon was mainly based on the activity in the electromagnetic calorimeters with or without any associated track. Since the probability for the photon to convert into a electron–positron pair was quite large, `REMCLU` contains algorithms which tries to minimize the impact of this phenomena. In the STIC acceptance where there is no tracking information the electron–photon separation was based on the information from two scintillator layers located in front of the STIC calorimeters.

For the muon identification the standard DELPHI algorithms were used [10], which were based mainly on the MUC information together with associated tracks and some HAC activity.

The SUSANA selection criteria is described in section 4 where the whole chargino event selection will be described in detail.

Chapter 4

Likelihood Ratio Based Event Selection

The DELPHI chargino analysis was a search where different event topologies were combined to maximize the sensitivity to detect a possible production of chargino pairs. The selection was further optimized within each topology with respect to the Δm value due to its high phenomenological impact.

The event selection was made in a number of steps where each step tightened the selection criteria. The different steps of the selection procedure were made separately in order to make the analysis more transparent and to make it easy to monitor the quality of the SM background simulation and compare it to the data.

The event selection was based on a likelihood ratio method which provided a powerful tool to obtain a minimal excluded cross section under the assumption that no chargino signal was present. An other advantage of using the likelihood ratio method, compared to a conventional selection based on sequential cuts, is that the likelihood ratio selection is based on only one discriminating variable and the optimized cut on this variable is easily re-tuned for different data samples. When the analysis is made for different data samples recorded at different center–of–mass energies the likelihood ratio method is therefore very easily adopted to the different samples while a sequential analysis normally have to re-tune all the cuts for each sample.

The analysis was not only made separately for the six different Δm regions within the four topologies, but also for the nine data samples recorded at the different center–of–mass energies 192, 196, 200, 202, 205, 206, 207, 208 and 206.5S1 (GeV, a specific Δm region in one of the topologies at a certain center–of–mass energy will be referred to as a specific search window). The sample 206.5S1 corresponds to the 60.1 pb^{-1} recorded during the year 2000 when sector 6 in the TPC was not working. The difference in Δm affect the distributions for many observables of the signal events significantly since the Δm value is closely related to the visible energy of an event. This effect have been studied [25], in terms of variation of the distributions, from simulated chargino signal events at different Δm values.

Figure 4.1 shows how the mean value of the visible energy and the missing transverse momentum changes with the Δm value and the Δm regions for the analysis were chosen to give distributions with similar shapes within a given Δm. The six Δm regions chosen are shown in table 4.1.

Figure 4.2 shows a schematic description of the event selection used in the DELPHI chargino search, where the selection was made separately for each center–of–mass energy. The events were first selected into one of four different topologies. The four topologies are mutually exclusive and hence an event can only belong to one topology. The remaining selection procedure was made separately for the different topologies. A set of common cuts was used after the topological classification which was the same for all Δm regions. These cuts were used to reject events

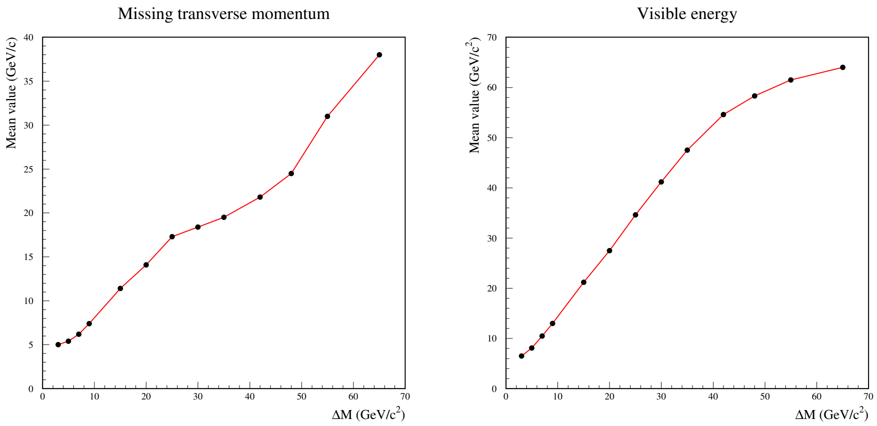

Figure 4.1: Mean values of the distribution of the missing transverse momentum and visible energy as a function of Δm for hadronic chargino events with $m_{\tilde{\chi}_1^{\pm}} = 103.3$ GeV$/c^2$ at $\sqrt{s} = 207$ GeV .

Δm regions	
1	$3 \leq \Delta M < 5$ GeV$/c^2$
2	$5 \leq \Delta M < 10$ GeV$/c^2$
3	$10 \leq \Delta M < 25$ GeV$/c^2$
4	$25 \leq \Delta M < 35$ GeV$/c^2$
5	$35 \leq \Delta M < 50$ GeV$/c^2$
6	50 GeV$/c^2 \leq \Delta M$

Table 4.1: The different Δm regions.

which did not originate from the LEP collisions, e.g. events triggered by cosmic rays, and to reduce the background from processes with very high cross sections, e.g. Bhabha and two photon events. Since the variables used by the likelihood ratio method were not totally uncorrelated, an additional preselection was made based on the signal distributions. These cuts were made to reject background events with properties very unlike the signal events, to minimize correlation effects in the proceeding likelihood ratio selection. This preselection was made separately for all the Δm regions. The events in a given topology and Δm region that were accepted by the described selection chain were then used in the likelihood ratio selection. The likelihood ratio method was used for all individual Δm regions and an optimization of the set of variables used by the likelihood ratio method was also made for each window. All steps in the event selection was based only on simulations of the SM background and the chargino signal. No corrections were made based on the data such as a manual scan of the chargino candidates.

A so called "weighting" method was used to estimate the systematic errors on the selected number of background events, due to an imperfect simulation of the detector response. For the statistical errors a Poisson based method was used which made it possible to compute asymmetric errors.

The selection method and algorithm will be described generally, including all the topologies,

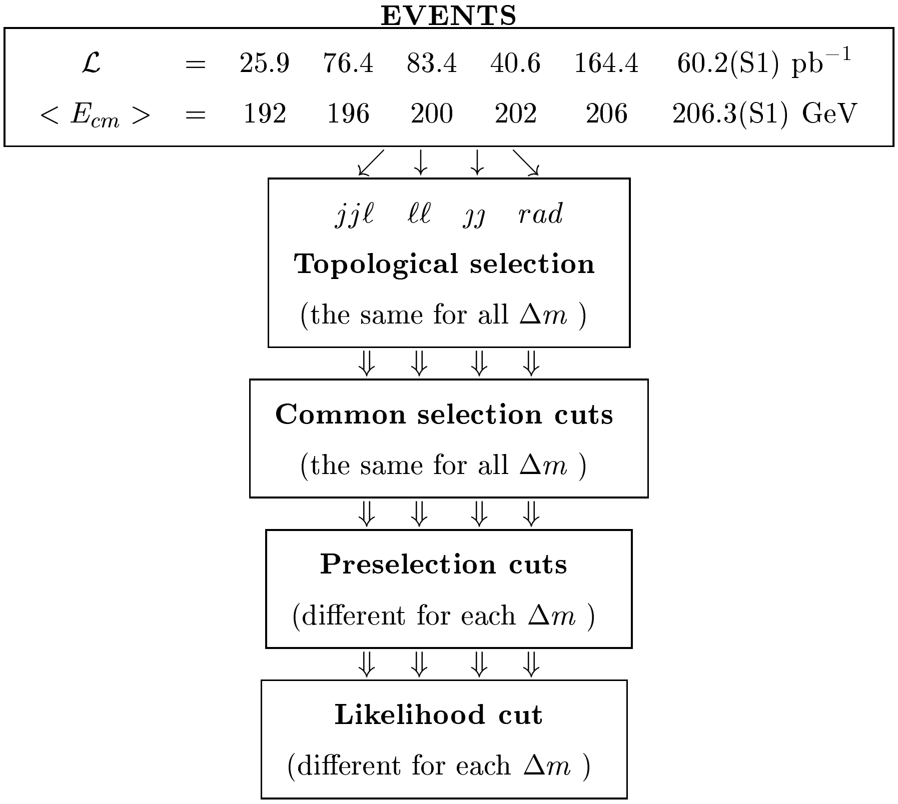

Figure 4.2: A schematic overview of the event selection used in the DELPHI chargino analysis.

in the following sections, but it should be noted that the results from the event selection presented in section 4.4 will only concern the $jj\ell$ and rad topologies.

4.1 Likelihood Ratio Optimization

A likelihood ratio method can be used in searches for new particles to optimize the analysis either for a discovery or to exclude the theory investigated. The likelihood ratio method uses probability density functions of different variables to construct only one discriminating variable. In the case where no signal is observed one normally wants to compute exclusion limits of the theory from the measurement. Minimizing the excluded cross section with a cut on the discriminating likelihood ratio variable will then give the optimum event sample for the analysis. For a set of uncorrelated variables the likelihood ratio method gives the best background suppression possible for a given signal efficiency [24]. The method can also be used in the case where the variables are weakly correlated since the result will be close to the real optimum. Due to the ability to optimize the whole event selection by using only one discriminating variable the likelihood ratio method provides, apart from being a powerful signal to background optimization, a very convenient method for re-tuning the event selection to different event samples, e.g. data samples with different center–of–mass energies where an analysis based on sequential cuts would have to be re-tuned with respect to all the cuts individually.

4.1.1 The Likelihood Ratio Method

The likelihood ratio method uses a likelihood ratio function, $\mathcal{L}_\mathcal{R}(x_1,...,x_n)$, as a discriminating variable. The $\mathcal{L}_\mathcal{R}$-function gives a measure of how signal-like an event is, with respect to a certain set of variables. From this $\mathcal{L}_\mathcal{R}$-function one classifies an event as a signal candidate if the likelihood ratio value of the event exceeds a specified cut, $\mathcal{L}_\mathcal{R}(x_1,...,x_n) > \mathcal{L}_{\mathcal{R}cut}$.

The $\mathcal{L}_\mathcal{R}$-function is constructed from probability density functions (pdfs) of different discriminating variables from the signal and background events. If $P^i_S(x_i)$ is the pdf of variable x_i for the signal and $P^i_B(x_i)$ is the pdf of variable x_i for the background the likelihood functions for the signal and the background respectively are defined as

$$\mathcal{L}_S = \Pi^n_{i=1} P^i_S(x_i) \tag{4.1}$$

$$\mathcal{L}_B = \Pi^n_{i=1} P^i_B(x_i) \tag{4.2}$$

and the $\mathcal{L}_\mathcal{R}$-function, for non-correlated variables, is defined as

$$\mathcal{L}_\mathcal{R}(x_1,...,x_n) = \frac{\mathcal{L}_S}{\mathcal{L}_B} = \frac{\Pi^n_{i=1} P^i_S(x_i)}{\Pi^n_{i=1} P^i_B(x_i)}. \tag{4.3}$$

The n-variables in $\mathcal{L}_\mathcal{R}(x_1,...,x_n)$ should be chosen such as to maximize $\mathcal{L}_\mathcal{R}(x_1,...,x_n)$ since this will get the best signal to background ratio from the event sample. It will be shown in the next section that it is usually quite easy to construct these pdfs and since they are not correlated (or at least very weakly correlated) it is possible to choose which and how many variables to use.

The $\mathcal{L}_\mathcal{R}$-function can also be used when the variables are weakly correlated since the result will be close to the optimum. If the variables are not independent, the $\mathcal{L}_\mathcal{R}$-function cannot be constructed by separately obtained pdfs of the variables and the $\mathcal{L}_\mathcal{R}$-function must be defined as

$$\mathcal{L}_\mathcal{R}(x_1,...,x_n) = \frac{P_S(x_1,...,x_n)}{P_B(x_1,...,x_n)}. \tag{4.4}$$

This function is usually much harder to construct in practice.

If Ω represent the region where $\mathcal{L}_\mathcal{R}(x_1,...,x_n) > \mathcal{L}_{\mathcal{R}cut}$, the number of background events, N_B, and the signal efficiency, ϵ_S, are defined as

$$N_B(\mathcal{L}_{\mathcal{R}cut}) = N_B(0) \times \int_\Omega P^1_B(x_1)\dots P^n_B(x_n)dx_1\dots dx_n \tag{4.5}$$

$$\epsilon_S(\mathcal{L}_{\mathcal{R}cut}) = \epsilon_S(0) \times \int_\Omega P^1_S(x_1)\dots P^n_S(x_n)dx_1\dots dx_n. \tag{4.6}$$

From the $N_B(\mathcal{L}_{\mathcal{R}cut})$ and $\epsilon_S(\mathcal{L}_{\mathcal{R}cut})$ one can find the $\mathcal{L}_{\mathcal{R}cut}$ that gives the minimal excluded cross section, which is then used for the final events selection.

4.1.2 The Probability Density Functions

In the case when the pdfs for the different variables can be obtained separately, this is usually done by producing the histograms of the variables from Monte Carlo simulations and then normalize them to one. In figure 4.3 (left) two histograms of the P_{miss}/E_{miss} from the simulated chargino signal and the SM background, at $\sqrt{s} = 206$ GeV for Δm region 6, is shown.

One usually wants to smooth out the high frequency statistical fluctuations, caused by the finite number of simulated events. In this way the pdf of the variable looks like if it had been produced with infinite statistics. Different kind of low pass filters can be applied for the smoothing. A triangular filter was used in the chargino analysis where the output signal is the input signal convoluted with a triangular function

$$P^{Smooth}(x) = \int P^{Raw}(x')t(x'-x)dx' \tag{4.7}$$

$$t(x) = \begin{cases} C-|x| & \text{if } |x| < C \\ 0 & \text{if } |x| \geq C \end{cases}$$

Since the pdfs in this analysis are represented by histograms consisting of a finite number of bins, the triangular filter was implemented in a more convenient discreet way. Because of the histograms bin structure, the triangular filter can be applied by recomputing the value of each bin by taking the weighted average of the neighboring bins weighted according to the triangular function, i.e. the value from a distant bin receive a small weight and vice versa.

Figure 4.3 and 4.4 shows two histograms from the $jj\ell$ topology in the year 2000 analysis with the TPC sector 6 ON in the Δm region 6, where figure 4.3 corresponds to the variable P_{miss}/E_{miss} and figure 4.4 to the θ–angle of the most energetic jet in the event. Both figures shows the simulated chargino signal and SM background distributions before and after applying the smoothing filter and one can clearly see how the statistical fluctuations are removed.

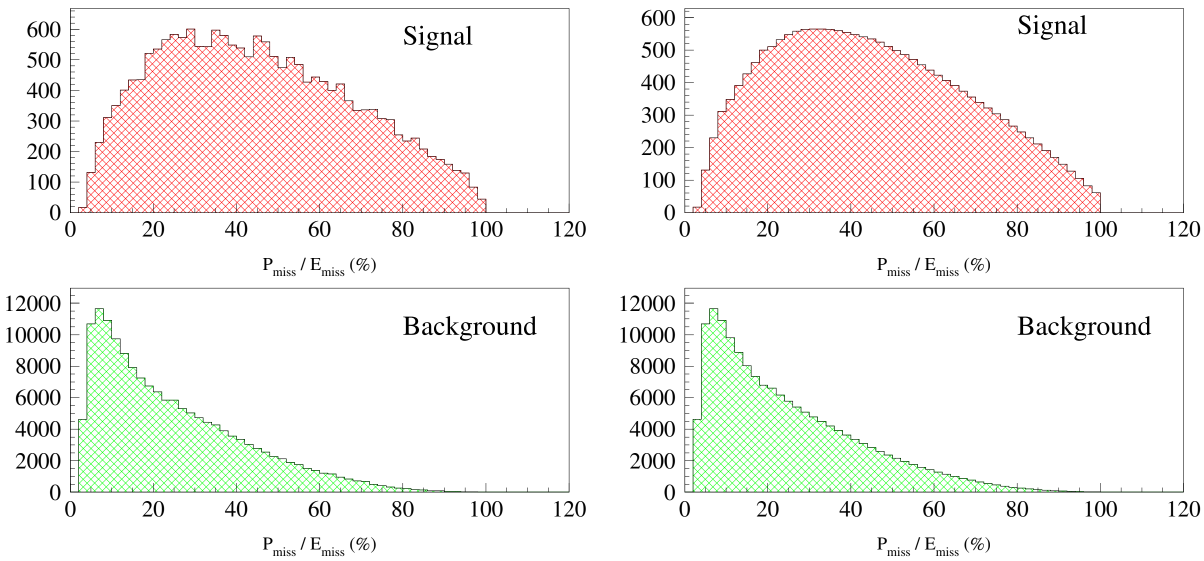

Figure 4.3: The P_{miss}/E_{miss} distributions from the signal and background used in the year 2000 analysis with TPC sector 6 ON for the $jj\ell$ topology in Δm region 6. The left and right plots corresponds to before and after applying the smoothing filter respectively.

After the smoothing, the histograms are normalized to one and in the chargino analysis a linear interpolation between the bins was used to make the pdfs into continuous functions. Pdfs are then produced for the signal and background variables, which can then be used to produce the likelihood ratio function or to evaluate the number of background events, $N_B(\mathcal{L}_{\mathcal{R}cut})$, and the signal efficiency, $\epsilon_S(\mathcal{L}_{\mathcal{R}cut})$. Figure 4.5 shows the signal and background pdfs of the variable P_{miss}/E_{miss}, produced from the histograms in figure 4.3. As shown in the figure, the background distribution decrease much faster than the signal with an increasing P_{miss}/E_{miss} value. Implying that the signal–to–background ratio, hence also the $\mathcal{L}_{\mathcal{R}}$ value, should be increasing with respect to this variable alone. This can be clearly seen in figure 4.6 which corresponds to the $\mathcal{L}_{\mathcal{R}}$ function from the distributions in figure 4.5, since the $\mathcal{L}_{\mathcal{R}}$ value increase strongly with increasing P_{miss}/E_{miss}.

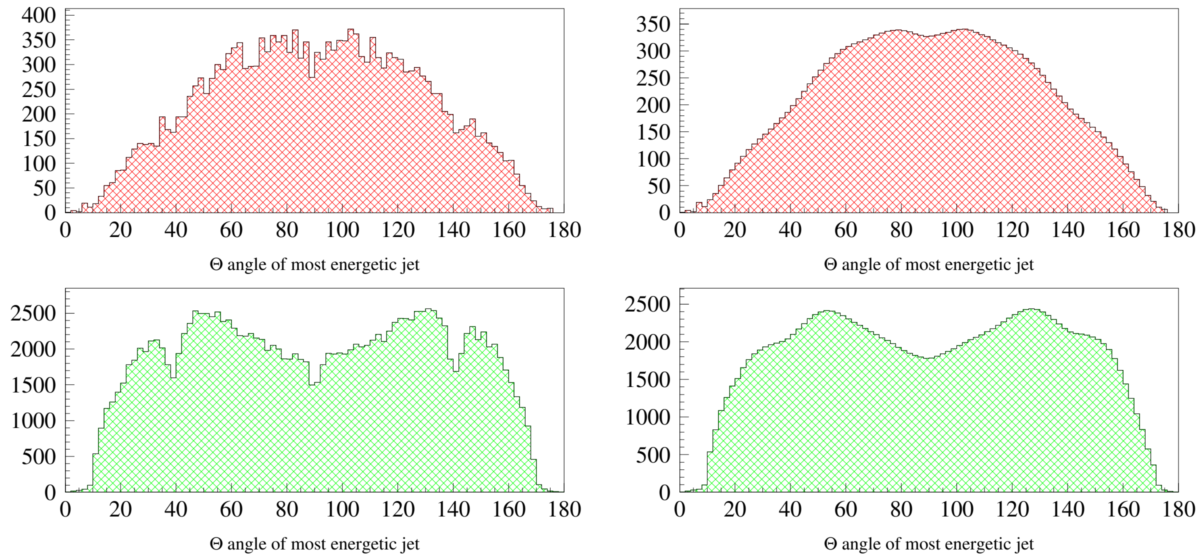

Figure 4.4: The polar angle distributions of the most energetic jet in the events for the signal and background used in the year 2000 analysis (with TPC sector 6 ON for the $jj\ell$ topology in Δm region 6). The left and right plots corresponds to before and after applying the smoothing filter respectively.

4.1.3 Optimizing the Expected Excluded Cross Section

The goal with the likelihood ratio optimization is to get an event sample where one can discover or exclude a signal as strongly as possible. The results of a search where no signal is observed are normally used to compute exclusion limits on the corresponding theory. The likelihood ratio method can in this case be used to optimize the event selection in order to exclude an as low signal cross section as possible.

The likelihood ratio cut which gives the lowest excluded cross section is found by minimizing the excluded cross section, with respect to the $\mathcal{L}_{\mathcal{R}cut}$ value

$$\sigma_{Exclusion} = \frac{N_{95}(N_B(\mathcal{L}_{\mathcal{R}cut}))}{\epsilon_S(\mathcal{L}_{\mathcal{R}cut}) \times L} \tag{4.8}$$

where L stands for the luminosity and N_{95} is the upper limit on the number of signal events expected from the background, at a 95% confidence level, which was computed with a mono-channel Bayesian formula (see section 5.3). The optimization is made under the assumption that there is no signal present and so the number of observed events is set equal to the number of events expected from the background. Since N_{95} and ϵ_S changes differently with respect to the $\mathcal{L}_{\mathcal{R}cut}$ a minimum can be found for the $\sigma_{Exclusion}$ (see figure 4.7) and it is at that $\mathcal{L}_{\mathcal{R}cut}$ value one obtains the best event selection to exclude the unobserved signal if the data consists only of background events. It is important to point out that the optimization should be made without using the real data, which could cause an overestimation of the limit by picking up statistical fluctuations.

Figure 4.8 shows how the number of expected SM background events evolves with $\mathcal{L}_{\mathcal{R}cut}$ (left) and also how the signal efficiency changes with $\mathcal{L}_{\mathcal{R}cut}$ (right). These results are again taken from the $jj\ell$ topology in the chargino analysis at $\sqrt{s} = 206$ GeV within Δm region 6 and the likelihood ratio function is constructed from all the variables used in this analysis. Figure 4.7 (left) shows how the expected excluded cross section, corresponding to the plots in figure 4.8, changes with the $\mathcal{L}_{\mathcal{R}cut}$ and the minimum excluded cross section corresponds to about 0.09 pb at $\mathcal{L}_{\mathcal{R}cut} = 211$. The variation of the excluded cross section in this window is relatively modest

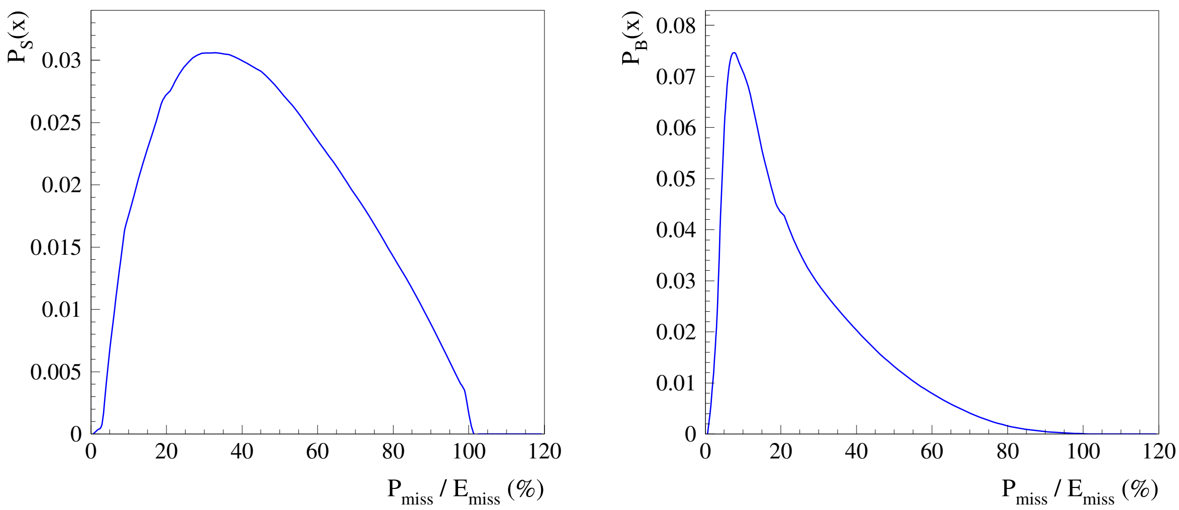

Figure 4.5: The pdfs of the P_{miss}/E_{miss} histograms in figure 4.3. The left and right plots corresponds to signal and background respectively.

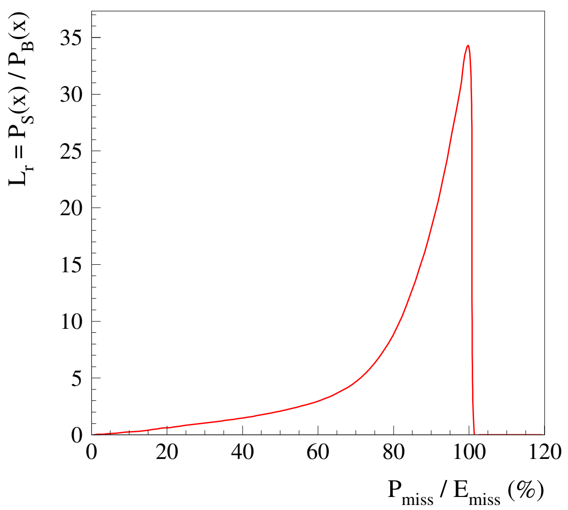

Figure 4.6: The likelihood ratio function from the P_{miss}/E_{miss} pdfs in figure 4.5.

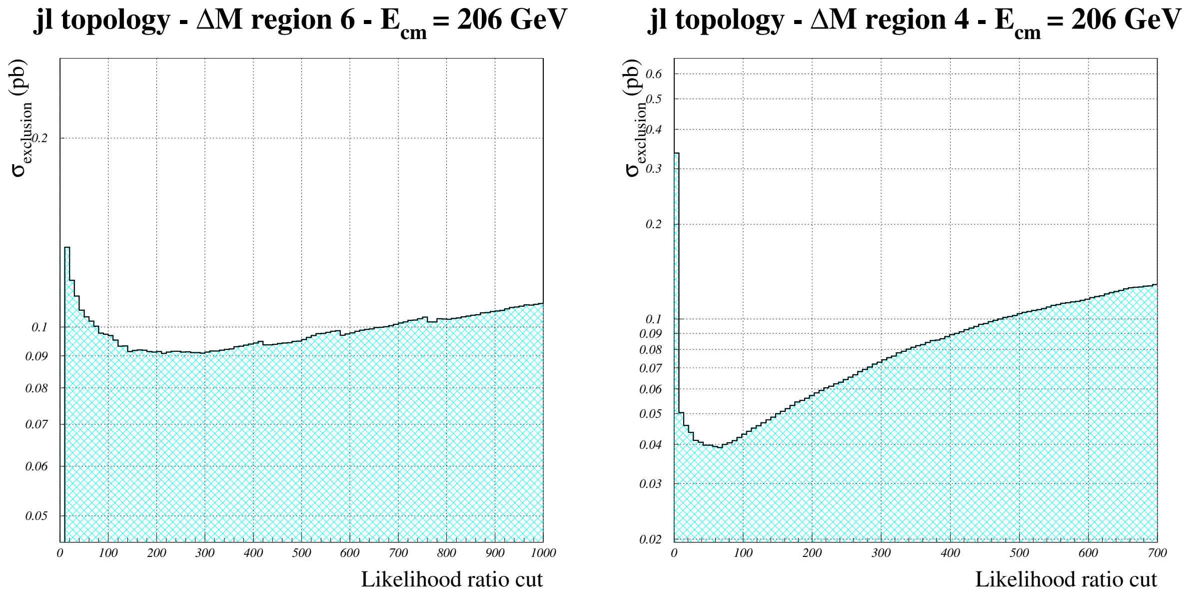

Figure 4.7: The cross section excluded at 95% C.L. as a function of the likelihood ratio cut. Left: Results obtained from the analysis made for the $\sqrt{s} = 206$ GeV data sample within the $jj\ell$ topology with Δm region 6. Right: Results obtained from the analysis made for the $\sqrt{s} = 206$ GeV data sample within the $jj\ell$ topology with Δm region 4.

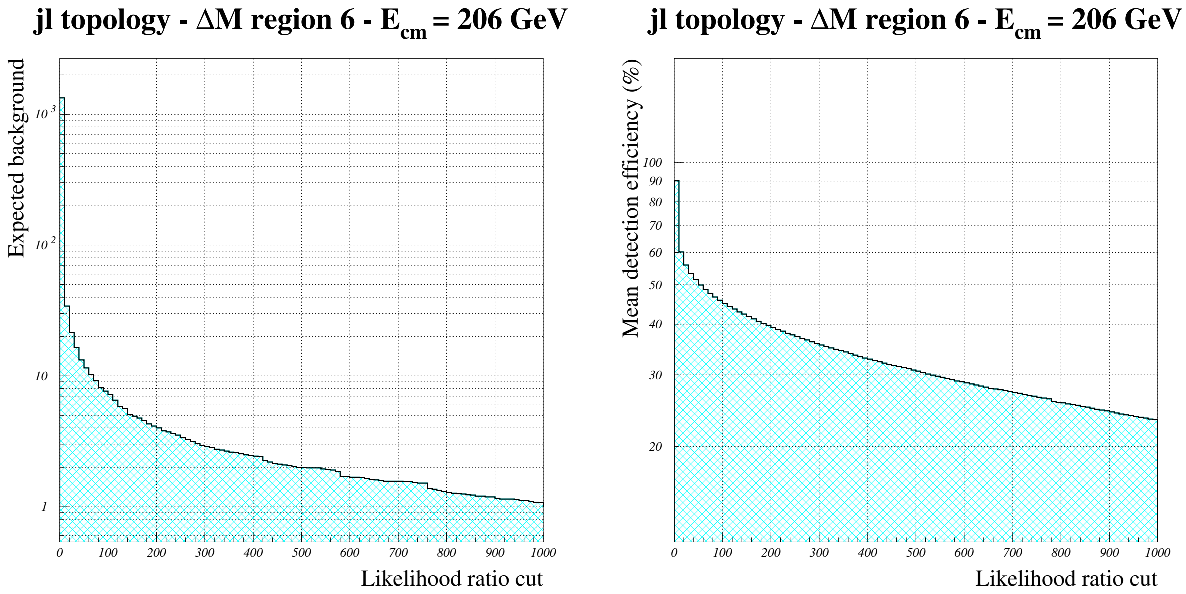

Figure 4.8: The expected number of background events as a function of the $\mathcal{L}_{\mathcal{R}cut}$ (left) and the signal efficiency as a function of the $\mathcal{L}_{\mathcal{R}cut}$ (right).

and figure 4.7 (right) shows the more extreme case of Δm region 4 where the excluded cross section varies between 0.33 pb and 0.04 pb.

In plot 4.7 (left) the first bin is zero. This is only a feature of the algorithm where the first bin is skipped if its corresponding number of background events exceeds one thousand. This is only to speed up the computation, since the optimum will in any case not be in the first bin.

4.2 The Chargino Event Selection

The event selection procedure in the DELPHI chargino search was divided into four parts: the topological selection, the common selection, the automatic preselection and the likelihood ratio based selection. The reason to divide it into these parts was both to make the analysis more transparent and to be able to monitor the quality of the background simulation. This made it easier to understand various biases by the analysis on the resulting observables as well as it enhanced the possibility to understand discrepancies connected to problems with the SM background simulation. In searches for new physics, problems due to imperfect simulations of the SM events is normally larger than in other analysis, since optimization of the signal–to–background ratio tend to select events from the tails of the distributions. Here the simulation is more problematic than in the region where the bulk of the events is located.

4.2.1 The Topology Selection

The first part of the event selection in the chargino analysis was the topology selection. At this stage the events are selected into one of the four event topologies:

- $jj\ell$ - The semi-leptonic topology contains events with more than five charged particles, no isolated photons and at least one isolated lepton. The lepton must have a momentum $P_\ell >$ 3 GeV/c and an isolation angle $\alpha_\ell^{Isolation} > 20°$ from the jets;
- $\ell\ell$ - The leptonic topology contains events with five or less charged particles and no isolated photons;
- jj - The hadronic topology contains events with more than five charged particles and no isolated photons or leptons;
- rad - The radiative topology contains events with at least one isolated photon. The photon must have an momentum $P_\gamma > 5$ GeV/c and be within the polar angle acceptance $15° < \theta_\gamma < 165°$. The photon must also have an isolation angle $\alpha_\gamma^{Isolation} > 15°$.

Due to the complex and varying phenomenology expected from chargino pair production, the use of different event topologies increase the sensitivity significantly in many parts of the parameter space. It is important to note that events from one decay channel can be selected into different topologies. An event from the semi leptonic decay channel can for example be selected into the hadronic topology if the lepton is unidentified or an event from the hadronic decay channel can be selected into the leptonic topology if it has a small visible energy and a large fraction of neutral particles. An event from any chargino decay channel could also be selected into the radiative topology if an ISR photon is detected within the allowed acceptance. This migration effect can vary a lot and it also depends on the Δm region. These effects have been taken into account in the estimation of the detection efficiency. The splitting of the analysis into the four topologies also increases the sensitivity of the chargino search in general, since the signal to background ratio can be very different for different topologies and for different parts of the parameter space and this information can be extracted through the multi-channel method used [28, 29] for the confidence level computation. The $\ell\ell$ topology for example is very important in the lowest Δm region, from where the overall chargino mass limit is obtained. In the highest Δm region the chargino signal would be similar to the WW background (especially if the Δm is close to the W mass). Here the rad topology is very important since the chargino might in this region decay through a cascade decay and emit a photon. The photon spectrum would in this case differ a lot from ISR.

4.2.2 The Common Selection

The common selection is composed of three sets of sequential cuts. The three sets were designed for different reasons, but with the purpose to get a well simulated event sample of a reasonable size to use in the likelihood ratio selection. The cuts were made very loose so that the signal detection efficiency is only marginally decreased and to keep a statistically significant number of events for data – Monte Carlo comparison. The first set of cuts were made to reject events which are not well reconstructed or where detector noise and background contamination are not related to the e^+e^- collisions. The second set of cuts was used to select events with SUSY-like properties. This was to reject the large number of events from background processes with a high cross section which have topologies unlike events produced in SUSY processes. Both these two sets of cuts were the same for all topologies and Δm regions. The third set introduces specific cuts for the different topologies to reduce high cross section background sources which are specific for a specific topology. The topology specific cuts were the same for all the different Δm regions (with two exceptions).

Common cuts, set # 1
≥ 1 charged particle with $P_T > 1.5$ GeV
$P_t^{Total} > 4$ GeV
≥ 2 charged particles
≥ 1 reconstructed track in the TPC
$< 75\%$ rejected particles
$< 40\%$ E^{total}_{VD-ID} relative to $E_{visible}$
$< 40\%$ error of $E_{neutral}$ relative to $E_{visible}$

Table 4.2: The first set of common cuts. They are made to reject events that are not well reconstructed or detector noise and background contamination which is not related to the e^+e^- collisions.

Common cuts, set # 2
$\not{P}_t > 2$ GeV
$< 40\%$ of $E_{visible}$ recorded by STIC
Thrust < 0.98
Positive $\not{M}^2$
$\not{P}_t$ not pointing towards a $40°$ tagger element with a signal

Table 4.3: The second set of common cuts which were used to reject high cross section background sources which are different from a possible SUSY signal.

The first set of common cuts are listed in table 4.2. The first two cuts are very close to what the DELANA filter normally accepts for topologies containing charged particles. Together with the other cuts, the first set can efficiently reject events which are not originating from e^+e^- collisions. These events are usually triggered by cosmic radiation where the events are often characterized by particle trajectories through the detector which do not intersect at the interaction point. The other main category is events triggered by noise in the different subdetectors. In this case the events usually appears like isolated signals in a small number of subdetectors, e.g., as an isolated energy cluster in one of the calorimeters. The fifth cut in table 4.2 requires that less than 75% of the particles in the event were rejected by the quality requirements described in section 3.5. To pass the sixth cut the events must have less than 40% of its visible energy coming from pure VD and ID tracks and the last cut accepts events only if the error on the total energy of neutral particles (particles without any tracks related to them) is less than 40% of the visible energy in the event. The second set of SUSY related cuts are compiled in table 4.3. The first cut on missing transverse momentum is a very effective cut in SUSY searches, since many high cross section SM background processes have a very low missing transverse momentum whereas a typical SUSY signal have a high missing transverse momentum due to the escaping LSP. The second cut is designed to reject Bhabha events where the missing momentum criteria is fulfilled due to the emittance of an ISR photon that has escaped detection. The Bhabha cross section increase strongly with decreasing polar angle which makes this cut very powerful even though it is only used in the STIC acceptance. The next two cuts are also very efficient in rejecting SM background without a significant decrease of the signal efficiency. The thrust cut is used to select events with a cigar-like shape and the positive missing mass constraint is typical for SUSY events with conserved R-parity. The missing mass squared refers to the total missing energy of the reconstructed event squared minus the total missing momentum squared. The last cut listed in table 4.3 rejects events where the missing transverse momentum vector is pointing in the same azimuthal angle region (ϕ) as a 40° tagger with a signal and the tagger is not related to a reconstructed jet or charged particle.

Common cuts, set # 3				
Cut	$jj\ell$	$\ell\ell$	jj	rad
$\not{P}_t > 4$ GeV	X		X	X
$E_{EM}/E_{vis} < 95\%$	X		X	
Acoplanarity $> 10°$		X		
$P_t/E^{max}_{HCAL-neutral} < 0.4$ GeV	X		X	X
Photons are not allowed to convert (low Δm)				X
$E_{vis} < 65$ GeV (high Δm)			X	

Table 4.4: The third set of common cuts. They are used to reduce high cross section background sources typical in a specific topology.

The final topology related common preselection cuts are listed in table 4.4. Here the typical SUSY cut on missing transverse momentum was increased to 4 GeV/c in all topologies except the purely leptonic. The signal efficiency in the leptonic topology is normally more sensitive to this cut since the leptonic topology is the most important one in the low visible energy region (low Δm) of the signal. A cut on the acoplanarity was introduced instead for the leptonic topology. The acoplanarity cut rejects a large amount of low multiplicity background events, such as events from two photon processes and Bhabha events. In addition to the four first cuts, which are the same for all the six Δm regions, two Δm specific cuts were introduced. In the low Δm region in the radiative topology it was required that events were rejected if the photon was associated with tracks in the main tracking detectors[1]. This requirement decreased the problem with reconstructing photons that have converted due to the material between the interaction point and the EM-calorimeter. Finally, a cut on the visible energy was made in the fully hadronic topology in the high Δm region and this reduces the 2- and 4-fermion SM background significantly.

4.2.3 The Pre- and Likelihood Ratio Selection

At this stage the analysis was divided up into 24 windows, corresponding to the six Δm regions in each of the four topologies. The rest of the event selection was then performed separately for each window except for the three first Δm windows in the $jj\ell$ topology which were merged to one. In the rad topology the first four Δm regions were merged as well as the Δm regions 5 and 6. The merger in the $jj\ell$ and rad topologies was made in order to improve the statistics in these windows which would otherwise have been to low to obtain a satisfactory quality of the pdfs for the selection.

[1]The photon had to be classified as a tight photon according to REMCLU[23].

In the likelihood ratio based selection used in the chargino analysis a few additional steps were applied to minimize the impact of statistical effects from the SM and SUSY event simulation and the fact that some variables had a small correlation between each other. These additional procedures concerned the pdf construction algorithm and were as follows:

- **Fillhole** - If one bin in the histogram had a zero value, but its neighboring bins were not zero, the zero bin was given a value from linear interpolation between the neighboring bins. This prevented bins in the tails of the simulated histograms, which had a zero value due to the lack of statistics, to contribute with extreme likelihood ratio values.

- **Statkill** - If a part of the histogram was disconnected from the main part with more then one bin and had a total integrated value less than 1% of the main part it was removed. This was done to remove fluctuations which were small, but could give huge likelihood ratio values in areas of the variable distributions which are not of interest for the chargino analysis.

- **Preselection** - A cut was made where the corresponding signal histogram starts and ends for each variable used. This was a set of automatically generated preselection cuts which were made to cut away background events which were not in the region of the signal histograms of the variables used. The purpose of this cut was mainly to minimize the effect of the correlation between the variables, since the background events outside the signal region of one variable might change the shape of the distribution inside the region of the signal histogram of another variable.

The pdfs had to be generated two times in this algorithm. After the common selection the pdfs were generated (with the Fillhole and Statkill procedures) and from these pdfs the automatic preselection cuts were obtained. The event samples were then refined using the preselection cuts and the final pdfs were then produced.

The various procedures are demonstrated in figure 4.9 and 4.10. In both figure 4.9 and 4.10 the signal and background pdfs (left) are shown together with the corresponding likelihood ratio function (right). Both figures are based on the variable E_{vis}/E_{cm} from the $\ell\ell$ topology in Δm region 4. The plots in figure 4.9 are obtained only from the simulated events, before smoothing or any of the procedures mentioned. In figure 4.10 the signal and background histograms are plotted after applying the Fillhole procedure, the smoothing and also the Statkill procedure. The likelihood ratio function in figure 4.10 is produced using the whole pdf construction algorithm, i.e. also including the Preselection procedure. An example of the Fillhole procedure can be seen if one compares the signal histograms from figure 4.9 and 4.10, where the bin from 42% to 44% have been given a value based on its neighbors before the histogram was smoothed. The two background histograms shows how the Statkill procedure have removed the disconnected low probability area between 86% and 100%. The preselection cut can be demonstrated in figure 4.10 where a cut is made at 52% on the background events used to produce the corresponding likelihood function.

After the probability density functions were produced using the above algorithm, the likelihood ratio function was calculated, according to the method for uncorrelated variables in section 4.1. An optimization was also made to construct the likelihood ratio function based on the optimal set of discriminating variables. The optimization was based on the variables:

- The total multiplicity (# Part);

- The charged multiplicity (# Tracks);

- The leptonic multiplicity (# ℓ);

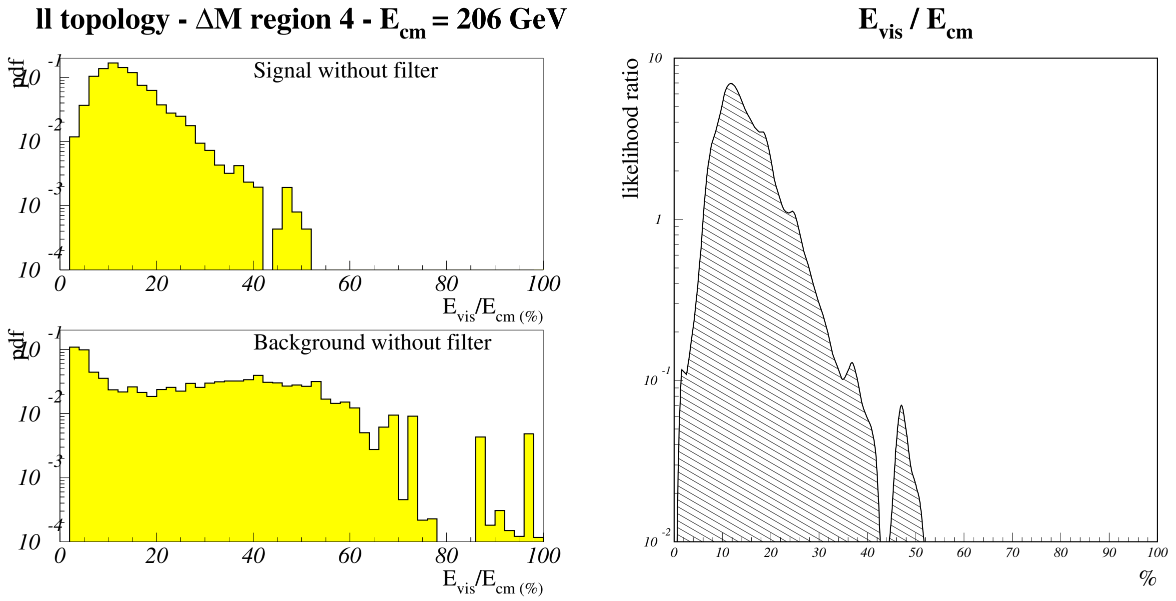

Figure 4.9: Probability density functions of the ratio between the visible energy and the center–of–mass energy for the signal and background events (left) from Δm region 4 of the $\ell\ell$ topology passing the common selection. Together with the corresponding likelihood ratio function (right).

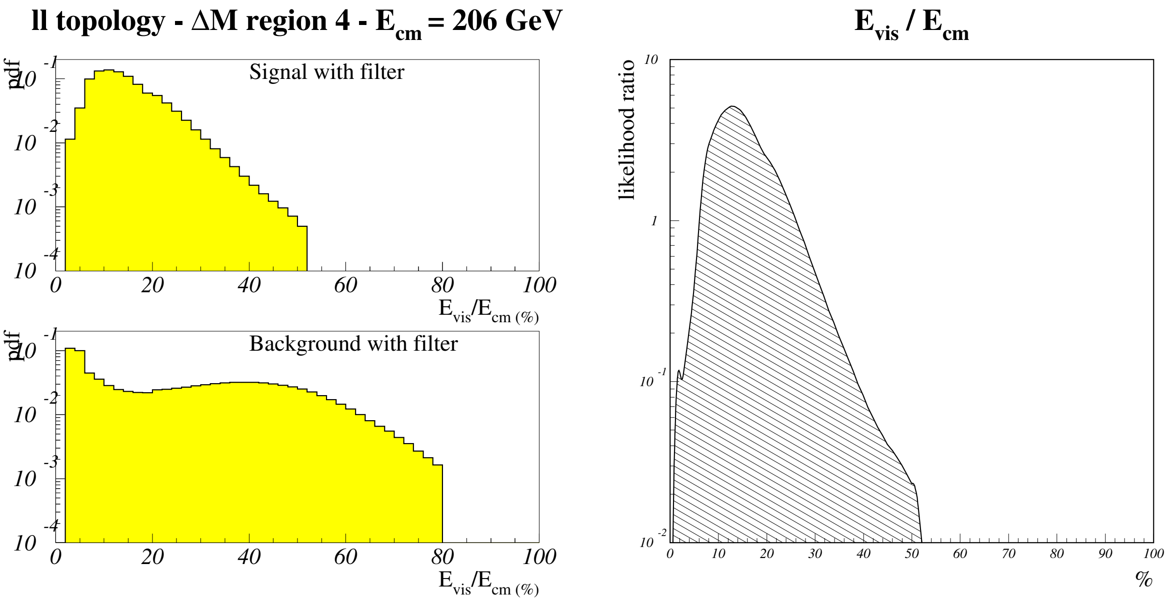

Figure 4.10: Probability density functions of the ratio between the visible energy and the center–of–mass energy for signal and background (left) events from Δm region 4 of the $\ell\ell$ topology where the smoothing, **Fillhole** and **Statkill** procedures were used. The corresponding likelihood ratio function obtained using the whole pdf construction algorithm is also given (right).

- The visible mass (M_{vis});
- The invariant mass of the lepton–neutrino system ($M_{\ell\nu}$);
- The invariant mass of the hadronic system (M_{jj});
- The missing transverse momentum ($\not{P}_t$);
- The momentum of the most energetic track (P^{max}_{track});
- The momentum of the second most energetic track (P^{2nd}_{track});
- The momentum of the most energetic isolated lepton (P^{max}_{ℓ});
- The momentum of the most energetic jet (P^{max}_{jet});
- The squared sum of the transverse momentum with respect to the thrust axis ($\tilde{P}^2$);
- The visible energy (E_{vis});
- The transverse energy (E_t);
- The charged transverse energy (E^{ch}_t);
- The fraction of EM energy ($\%\ E_{EM}$);
- The energy fraction in the 30° forward cone ($\%\ E^{cone}_{30^\circ}$);
- The energy fraction of the most energetic photon and EM energy (E^{max}_{γ}/E_{EM});
- The effective center–of–mass energy ($\sqrt{s'}$);
- The theta angle of the missing momentum ($\theta_{\not{p}}$);
- The theta angle of the most energetic track (θ^{max}_{track});
- The theta angle of the most energetic jet (θ_{jets});
- The theta angle of the most energetic neutral particle ($\theta^{max}_{neutral}$);
- The acoplanarity;
- The acollinearity;
- The separation distance where the event classification changes from 2 jets to 3 jets using the LUCLUS algorithm (y^{cut}_2).

The likelihood ratio optimization was performed for all windows with likelihood ratio functions constructed by all combinations of the variables presented above (with a minimum of four variables) to distinguish the optimal set of variables for each topology and Δm region. The same sets of variables were used in the final selection both for the samples with TPC sector 6 ON and OFF. The optimal sets of variables used for the different Δm regions in the $jj\ell$ and rad topologies of the analysis of the 2000C1 data are shown in table 4.5-4.6.

<table>
<tr><th>Topology</th><th>Variables</th><th colspan="6">Δm regions (GeV/c^2)</th></tr>
<tr><td></td><td></td><td>$3 \leq \Delta m < 5$</td><td>$5 \leq \Delta m < 10$</td><td>$10 \leq \Delta m < 25$</td><td>$25 \leq \Delta m < 35$</td><td>$35 \leq \Delta m < 50$</td><td>$50 \leq \Delta m$</td></tr>
<tr><td rowspan="9">$jj\ell$</td><td>Acoplanarity</td><td colspan="3">X</td><td>X</td><td>X</td><td>X</td></tr>
<tr><td>$\not{P}_t$</td><td colspan="3">X</td><td>X</td><td>X</td><td></td></tr>
<tr><td>$\theta_{\not{p}}$</td><td colspan="3">X</td><td>X</td><td>X</td><td>X</td></tr>
<tr><td>% E_{EM}</td><td colspan="3"></td><td></td><td></td><td>X</td></tr>
<tr><td>$\not{M}$</td><td colspan="3"></td><td></td><td></td><td>X</td></tr>
<tr><td>θ_{jets}</td><td colspan="3"></td><td>X</td><td></td><td>X</td></tr>
<tr><td>$M_{\ell\nu}$</td><td colspan="3">X</td><td>X</td><td>X</td><td>X</td></tr>
<tr><td>M_{jj}</td><td colspan="3"></td><td>X</td><td>X</td><td>X</td></tr>
<tr><td>P_{ℓ}^{max}</td><td colspan="3">X</td><td></td><td>X</td><td>X</td></tr>
</table>

Table 4.5: The optimal set of variables defining the likelihood ratio for each Δm region in the $jj\ell$ topology in the analysis of 2000 C1 and S1 data.

Topology	Variables	Δm regions (GeV/c^2)					
		$3 \leq \Delta m < 5$	$5 \leq \Delta m < 10$	$10 \leq \Delta m < 25$	$25 \leq \Delta m < 35$	$35 \leq \Delta m < 50$	$50 \leq \Delta m$
radiative	Acoplanarity	X				X	
	E_{vis}	X				X	
	P_{track}^{max}	X				X	
	P_{track}^{2nd}	X				X	
	P_{jet}^{max}	X				X	
	E_t	X				X	
	E_t^{ch}	X				X	
	E_γ^{max}/E_{EM}	X				X	

Table 4.6: The optimal set of variables defining the likelihood ratio for each Δm region in the *radiative* topology in the analysis of 2000 C1 and S1 data.

4.3 Systematic and Statistical Errors

Various methods have been used in order to estimate the systematic errors. In this section the method used to estimate the systematic errors on the selected number of background events will be explained.

The way the statistical errors on the number of selected background events have been computed will also be described.

4.3.1 Systematic Errors with a Weighting Method

This method was used to estimate the systematical error on the number of selected background events due to an imperfect simulation of the detector response. It is based on how the difference between the data and the simulated background at preselection level propagates to the final selection level with respect to the variables relevant for the analysis.

For each discriminating variable used in the event selection, a 25 bin histogram was built from the data and the simulated background at both preselection and final level.

From the preselection histograms a weight factor was calculated as N_{Data}/N_{Back} for each bin. After applying this factor on the background distribution it was in perfect agreement with the data. The weighting factor was computed if the bin contained at least 1 % of the total number of background events and the number of data events was not equal to zero.

The background histograms at the final selection level were then weighted with the factors from the corresponding bins at the preselection level and the systematic error for each variable was then determined by subtracting the total number of selected background events from the total number of weighted background events.

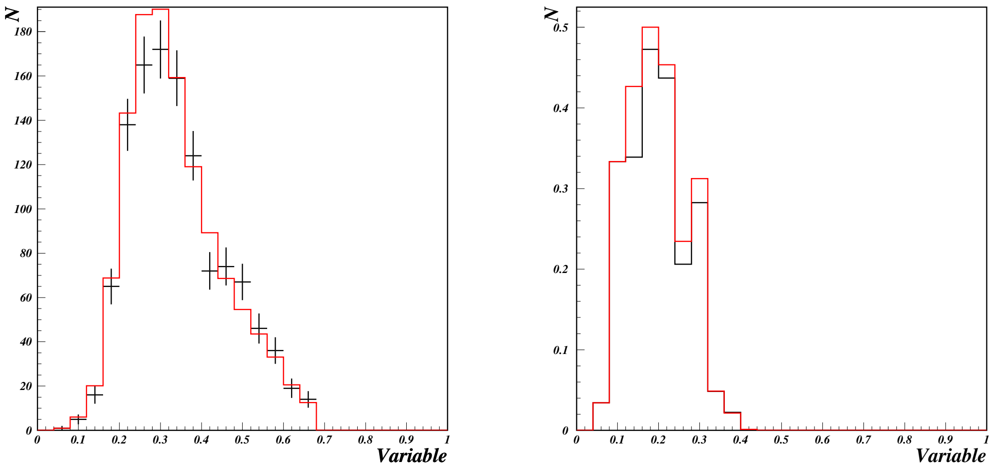

Figure 4.11: A variable distribution at preselection level (left) where the weighting factors for each bin are obtained from N_{Data}/N_{Back} (the data is represented by the crosses and the background as the solid line) and the distribution at the final level (right) with weighting (lower curve) and without weighting (upper curve).

The left plot in figure 4.11 shows an example of a variable which is divided into 25 bins and from which the weighting factors are computed. The right plot shows the same distribution at the final level with and without weighted bins. The error for this variable is then obtained by the integral of the lower curve minus the integral of the upper curve.

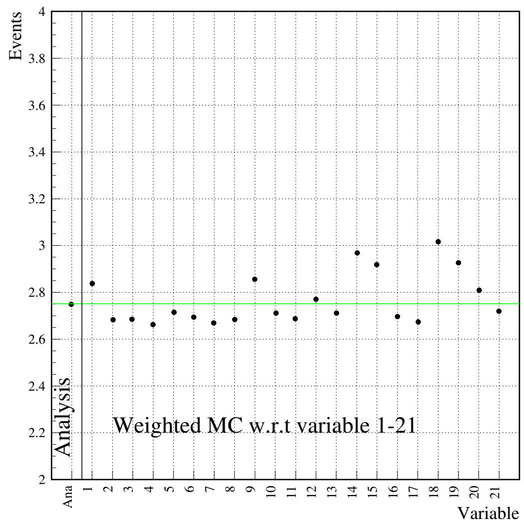

Figure 4.12: A comparison between the number of selected background events before and after weighting for the different variables used in the analysis.

Figure 4.12 shows an example of the total number of selected background events in a particular search window, with and without weighting of the different variables. The corresponding errors are seen as the deviation from the value obtained without weighting.

The total positive and negative systematical errors in a specific window are then computed as a quadratic sum of the errors from the different variables with a positive or a negative contribution,

$$\epsilon^{+} = \sqrt{\sum (N_{Back}^{RW}(i) - N_{Back})^2}\ , \quad if\ N_{Back}^{RW}(i) > N_{Back},$$

$$\epsilon^{-} = \sqrt{\sum (N_{Back}^{RW}(i) - N_{Back})^2}\ , \quad if\ N_{Back}^{RW}(i) < N_{Back}.$$

Where $N_{Back}^{RW}(i)$ is the number of re-weighted background events from variable i and N_{Back} is the number of selected background events without weighting.

These errors can become quite large in terms of percents, but since they affect the selected number of background events it is important to keep in mind the statistical relation between the number of background events and the final results (in this case a mass exclusion limit). For this reason a quite large relative error does not necessarily give a significant error on the result.

Since one systematic effect, due to the imperfect simulation of the detector response, probably affect all the variable distributions to a different extent it seems likely that the same systematic error is taken into account several times in the quadratic sum.

This was investigated by a Kolmogorov test which gave the probability that a data and a background histogram at preselection level originated from the same distribution. This test was used to study how the compatibility between the data and the background histograms of a variable change when the background was weighted with respect to all the other variables. Table 4.7 gives an example of how the probability from the Kolmogorov test changed when the background histograms for six different variables were weighted with respect to the different

	var(1)	var(2)	var(3)	var(4)	var(5)	var(6)
Pre.	0.957	0.834	0.174	0.924	1.000	0.869
var(1)	1.000	0.995	0.244	(0.878)	1.000	0.922
var(2)	0.991	1.000	0.241	(0.913)	1.000	0.922
var(3)	1.000	0.995	1.000	(0.911)	1.000	(0.834)
var(4)	0.991	0.940	0.241	1.000	1.000	0.939
var(5)	(0.928)	(0.789)	0.177	0.926	1.000	0.872
var(6)	0.991	0.904	(0.145)	0.955	1.000	1.000

Table 4.7: Results from the Kolmogorov test of six different variables. The row **Pre.** shows the results for the different variables distributions at preselection level without re-weighting and the rows **var(i)** contains the results when the background variable distributions were re-weighted with respect to the variable i.

variables. One can clearly see that when the background distribution for one variable was corrected, the agreement for most of the other variables were also improved.

The correlation between the variables was not studied with this method, but since the total systematic errors were computed as the quadratic sum, the Kolmogorov test showed that the total errors were overestimated. This is demonstrated in table 4.7 which shows that the contributions from the different variables partly contains the same error and hence the same error will be included several times in the quadratic sum of the total error. The systematic errors from this method are also overestimated since the statistical error for each bin is included in the weighting factor. This has as a result that the overestimation of the errors increase with the number of variables, but as long as the errors have a negligible affect on the final results (in this case the exclusion limits) they can be used as a conservative estimate. This method is only valid for estimating systematical errors from the detector response to the background, since it works with the individual variable histograms where the signal usually has a very different shape compared to the background.

The method described above does, however, not take into account all kinds of systematic effects that are insignificant on the preselection level but important after the final selection. No data – Monte Carlo discrepancy of this type was observed at any level of the analysis or in any of the Δm–windows and if this type of systematic errors exist they are expected to cause a very small change of the final limits.

4.3.2 Asymmetric Statistical Errors

The statistical errors on the number of selected background events were defined as a 68.3% confidence interval around the mean (to correspond to the one standard deviation confidence interval of a Gaussian distribution), computed such as to obtain individual positive and negative errors due to the asymmetric shape of the Poisson distribution. The errors were computed separately for the different simulated background samples. The positive [negative] error for a given process i was given by the difference between the number of events passing the selection (N_i) and the number of events ($\mu_i^{\pm}$) which corresponds to the upper [lower] bound of the 68.3% confidence interval.

$$\epsilon_i^{\pm} = \mu_i^{\pm} - N_i \tag{4.9}$$

The $\mu_i^\pm$ values were obtained by integrating the Poisson distributions in order to have the probability outside the confidence interval on each side, equally distributed $a = (1 - 0.683)/2$. Hence the values $\mu_i^\pm$ could be determined by the equation,

$$\beta^\pm = \int_{\mu_i^\pm}^{\infty} \frac{e^{-N_i} N_i^\nu}{\nu!}\, d\nu \tag{4.10}$$

where μ_i^+ (μ_i^-) would be obtained from $\beta^+ = a = 15.85\%$ ($\beta^- = 1 - a = 84.15\%$). The total positive and negative statistical errors are then computed by normalizing the errors estimated for the selected events from the individual background processes to the DELPHI luminosity and then summing them as a quadratic sum:

$$\epsilon^\pm = \sqrt{\sum_i \left(\frac{\epsilon_i^\pm\, \mathcal{L}\, \sigma_i}{N_i^{gen}} \right)^2} \tag{4.11}$$

where $\mathcal{L}$ represent the luminosity, N_i is the number of selected events for background process i, N_i^{gen} is the total number of generated events for a given process and σ_i is the corresponding production cross section.

4.4 Selection Results

The likelihood ratio function for the data recorded during the year 1999 was constructed and the $\mathcal{L}_{\mathcal{R}cut}$ cut was optimized using the signal and background MC events generated at $\sqrt{s} = 200$ GeV. Since the 1999 data was recorded at center–of–mass energies between 192 to 202 GeV the distributions were assumed to not change much and the same $\mathcal{L}_\mathcal{R}$ function and $\mathcal{L}_{\mathcal{R}cut}$ was used. Since the data recorded at the highest center–of-mass energy was the most sensitive for the chargino mass limit, the $\mathcal{L}_\mathcal{R}$ function was remade and the $\mathcal{L}_{cut}$ cut was re-optimized at $\sqrt{s} = 206$ GeV which corresponds to the mean energy of the data recorded during the year 2000. New Monte Carlo samples were made for the data recorded during the period when the TPC sector 6 was not working and for that reason the $\mathcal{L}_\mathcal{R}$ function and the $\mathcal{L}_{cut}$ was redone also for these Monte Carlo samples at the mean center–of–mass energy of $\sqrt{s} = 206.3$ GeV. This re-optimization of the final year data gave an improvement of between 4% to 35% in terms of expected excluded cross section within the individual Δm regions for the different topologies, compared to the expected excluded cross sections obtained with the selection based on the optimization at $\sqrt{s} = 200$ GeV. The difference in terms of expected excluded cross section between the selection from the C1 (sector 6 ON) and S1 (sector 6 OFF) samples, normalized to the same luminosity, was between 3% to 10%. Hence the quality was similar between the different samples and the chargino analysis was not affected much by the problem with the TPC during year 2000.

The results from the analysis of the selected events with the $jj\ell$ topology in the 50 GeV/c^2 $\leq \Delta m$ region with TPC sector 6 ON is given in figure 4.13a which shows the hadronic mass distribution from the events selected by the common selection. The plot shows that the dominating background in this particular search window consist of four fermion events and one can also clearly see the m_W peak at a hadronic mass value of 65 GeV/c^2. The value has been shifted due to the event reconstruction[2]. The second analysis is an example from the rad topology in the 3 $\leq \Delta m <$ 50 GeV/c^2 region with TPC sector 6 OFF. Figure 4.13b shows the total electromagnetic energy distribution after the common selection. From this plot one can see that in this search window the background consists mainly of two fermion events which can have a large cross section due to events with a high energetic ISR photon allowing an on-shell Z^0 in the s-channel. The distributions in figure 4.13 shows a good agreement between data and the

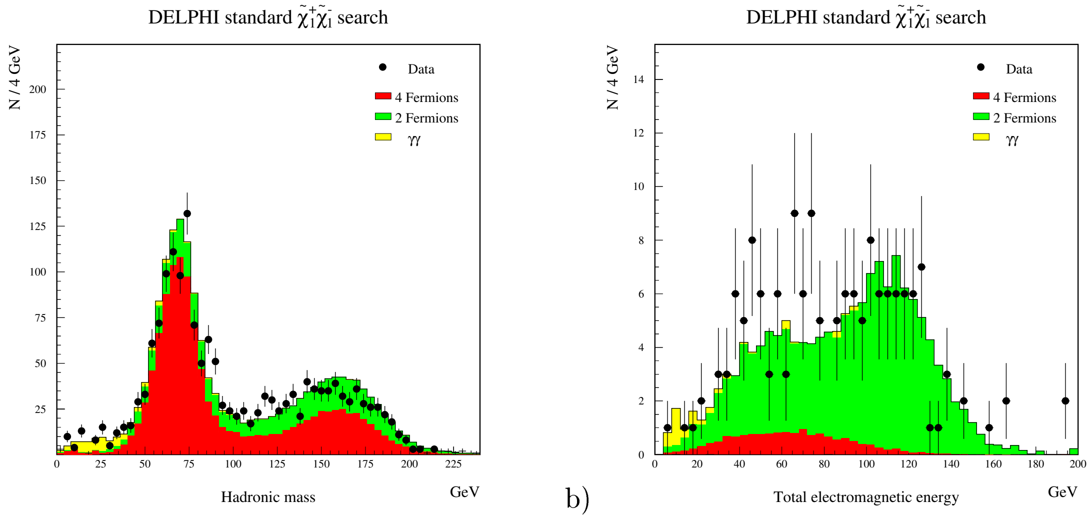

Figure 4.13: A data–MC comparison after the **common** selection. a) The $jj\ell$ topology for the data sample of year 2000 with the TPC sector 6 ON. b) The *rad* topology for the data sample of year 2000 with the TPC sector 6 OFF.

Monte Carlo and hence the background processes are well simulated in the part of phase space selected at this level.

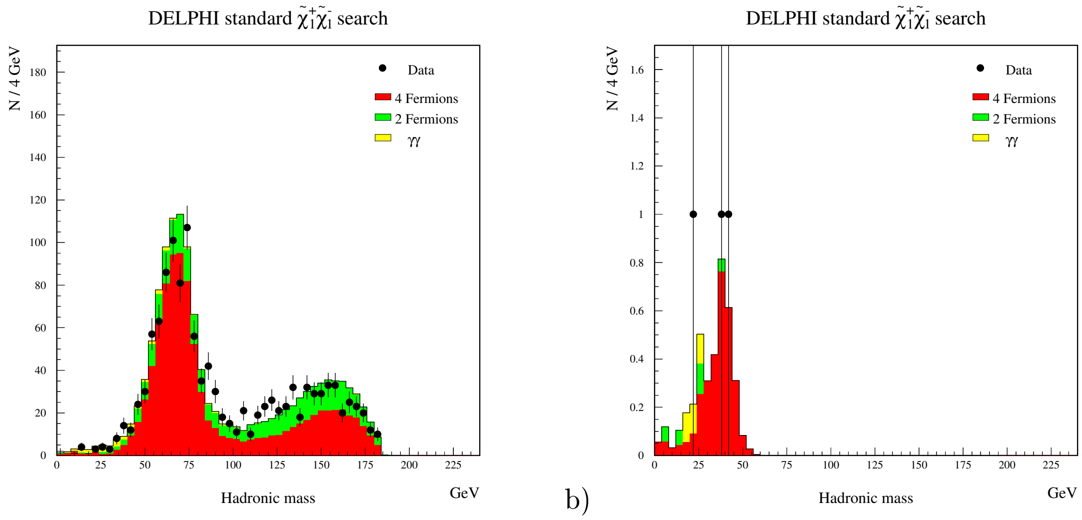

Figure 4.14: a) A data–MC comparison after the **preselection** for the $jj\ell$ topology. b) A data–MC comparison after the **final** selection for the $jj\ell$ topology. The data from year 2000 with TPC sector 6 ON in the region 50 GeV/$c^2 \leq \Delta m$.

After the common selection the event sample is further reduced by the preselection and then the final selection, which are made individually for the different Δm regions. Figure 4.14a shows the selected events after the preselection and after the common selection shown in figure 4.13a (for the 50GeV/c^2 $\leq \Delta m$ region). The total number of selected events at the preselection level for this search window corresponds to 1267 data events and 1338.6 expected events from the SM.

One can see that the data and Monte Carlo distributions are in a good agreement also at this level of the selection. Figure 4.14b shows the selected events after the final selection using the likelihood ratio method and 3 events were finally selected in the data analysis with 3.8 events expected from SM sources, i.e., no signs of an excess was observed in this search window.

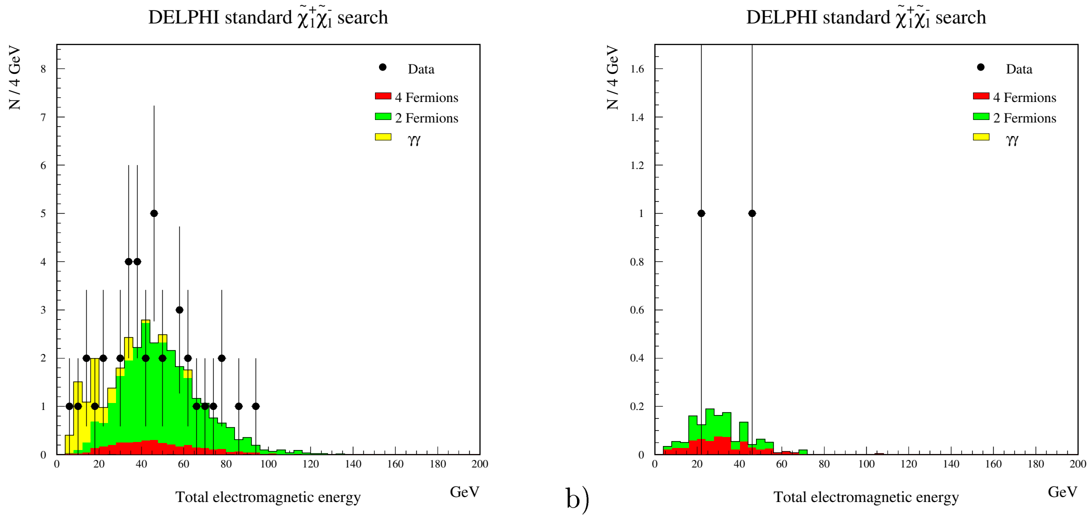

Figure 4.15: a) data–MC comparison at the **preselection** level for the *rad* topology. b) data–MC comparison at the **final** selection level for the *rad* topology. The data from year 2000 with TPC sector 6 OFF in the region $3 \leq \Delta m < 35$ GeV/c^2 .

The preselection and final selection plots after the common selection in figure 4.13b are shown in figure 4.15. Here the total number of selected events at the preselection level are 38 from the data and 32.6 expected from the SM background. 2 data events were selected after the final selection and 1.3 were expected. These were distributed as shown in figure 4.15b and also here the data agrees well with the expected background at all the levels of the selection.

A data – Monte Carlo comparison was also made as a function of the likelihood ratio cut. Figure 4.16 shows the data (dots) – Monte Carlo (solid line) comparison as a function of the likelihood ratio cut for the $jj\ell$ and rad windows previously discussed. In figure 4.16a one can see that the data – MC agreement is very good when the likelihood ratio cut is increased from the preselection ($\mathcal{L}_{cut} = 0$) level to the final selection cut ($\mathcal{L}_{cut} = 211$). Figure 4.16b shows the same for the rad window and also here the agreement is within the statistical errors of the data all the way from the preselection level to the final selection level ($\mathcal{L}_{cut} = 10$). The sharp drops of the simulated SM background are statistical effects due to the decreasing number of simulated SM events since different SM processes have a different number of simulated events.

Figure 4.17 shows the number of selected events as a function of the $\mathcal{L}_{cut}$ cut in Δm region 4 for the $jj\ell$ topology. The plot is obtained from the year 2000 data with the TPC working and the figure also shows how a chargino signal of $\sigma = 0.5$ pb (added to the SM background) would evolve with the $\mathcal{L}_{cut}$ cut. The signal corresponds to a $m_{\tilde{\chi}^\pm} = 102.8$ GeV/c^2 and $m_{\tilde{\chi}^0} = 73$ GeV/c^2. One can seen how the low number of signal events relative to the preselection sample is much less affected by the increasing likelihood ratio cut value than the SM background and how it would evolve into a statistically significant signal at larger $\mathcal{L}_{cut}$ values.

The number of selected events at the final level in the $jj\ell$ and rad topologies from the year 1999 and 2000 data are presented in table 4.8 for all the Δm regions and for both the period with the TPC sector 6 ON and OFF. Both statistical and systematic errors are shown. The

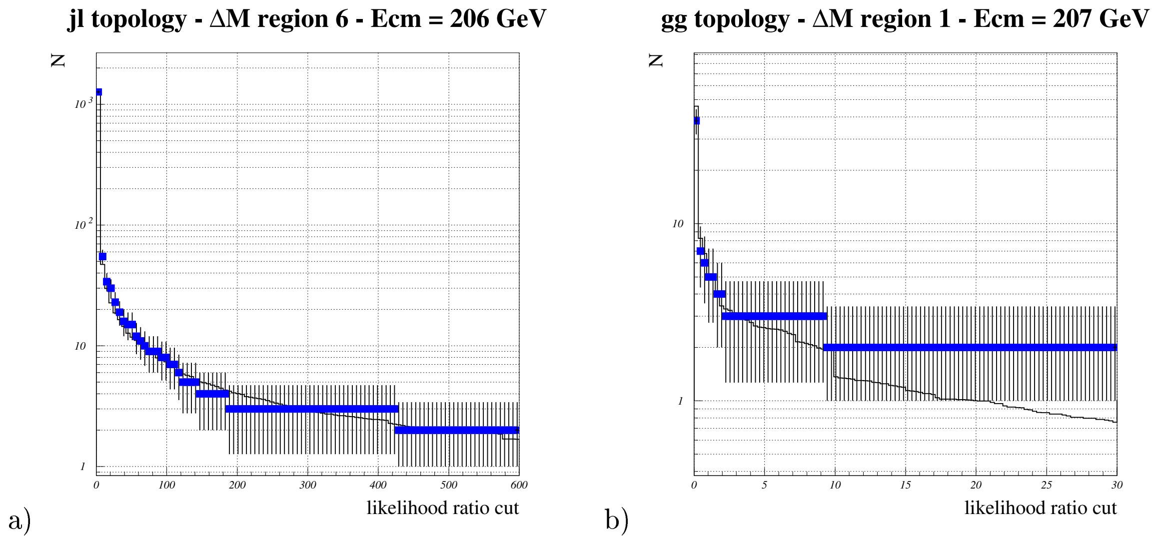

Figure 4.16: Selected number of data (dots) and Monte Carlo (solid line) events as a function of the likelihood cut. a) The $jj\ell$ topology, in the region 50 GeV$/c^2 \leq \Delta m$, for the data sample of year 2000 with the TPC sector 6 ON. b) The rad topology, in the region $3 \leq \Delta m < 35$ GeV$/c^2$, for the data sample of year 2000 with the TPC sector 6 OFF.

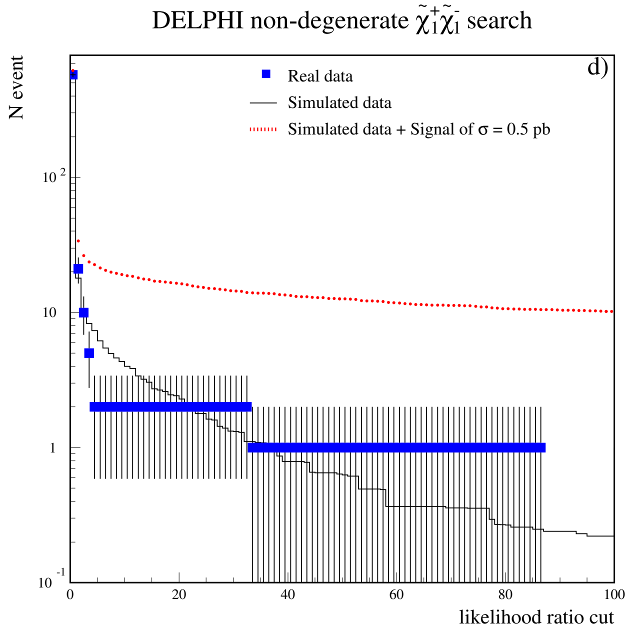

Figure 4.17: Selected data (dots) and Monte Carlo (solid line) events as a function of the likelihood cut in the region $25 \leq \Delta m < 35$ GeV$/c^2$ for the $jj\ell$ topology. The dotted line represent a $\sigma = 0.5$ pb chargino signal added to the background.

table shows a very good agreement between the selected number of data events and the expected number of SM background events for all the year 2000 windows. The data – MC agreement

Final selection - year 1999						
Topology	Δm 1	Δm 2	Δm 3	Δm 4	Δm 5	Δm 6
$jj\ell$	4			6	2	9
exp.	$2.3\ ^{+1.2+1.2}_{-0.2-0.1}$			$2.2\ ^{+0.4+0.7}_{-0.1-0.0}$	$2.3\ ^{+0.3+0.7}_{-0.0-0.1}$	$7.5\ ^{+0.5+2.2}_{-0.2-0.3}$
rad	7				14	
exp.	$5.3\ ^{+1.2+0.9}_{-0.3-0.2}$				$12.9\ ^{+1.2+1.7}_{-0.3-0.2}$	
Final selection - year 2000 with TPC sector 6 ON						
Topology	Δm 1	Δm 2	Δm 3	Δm 4	Δm 5	Δm 6
$jj\ell$	0			1	2	3
exp.	$0.4\ ^{+1.2+0.1}_{-0.1-0.0}$			$0.4\ ^{+1.2+0.0}_{-0.0-0.0}$	$2.4\ ^{+1.3+0.1}_{-0.2-0.1}$	$3.8\ ^{+1.3+0.4}_{-0.2-0.3}$
rad	3				11	
exp.	$2.5\ ^{+1.4+1.1}_{-0.2-0.1}$				$10.3\ ^{+1.3+1.6}_{-0.5-0.5}$	
Final selection - year 2000 with TPC sector 6 OFF						
$jj\ell$	0			0	0	1
exp.	$0.2\ ^{+0.5+0.1}_{-0.0-0.0}$			$0.4\ ^{+0.5+0.1}_{-0.0-0.1}$	$0.7\ ^{+0.4+0.0}_{-0.0-0.1}$	$2.0\ ^{+0.5+0.0}_{-0.1-0.6}$
rad	2				5	
exp.	$1.3\ ^{+0.5+1.0}_{-0.1-0.0}$				$4.3\ ^{+0.5+1.3}_{-0.2-0.0}$	

Table 4.8: The number of selected events after the final selection of the $jj\ell$ and rad topologies for the year 2000 data. The expected SM background is also shown together with its statistical and systematic errors.

for the data recorded during 1999 is also very good. The largest deviation is in the fourth $jj\ell$ window where there are 6 data events with 2.2 expected from the SM. This corresponds to a 2.6σ deviation which is perfectly normal to obtain in some bin when many selections are made (which is the case here since a separate selection was made for each search window). These events were further more studied and it was shown that three out of these six events contained an electron in the forward region and hence this could be related to a possible problem with the reconstruction made by the REMCLU package. The six selected events were partly found in all the four 1999 data samples, at $\sqrt{s} = 192-202$ GeV and no excess was found in the data collected during the year 2000 at higher energies, which would be expected of a chargino signal. This discrepancy was therefore not considered to be originating from chargino production and the data recorded during year 2000 could exclude a possible chargino signal beyond the kinematic reach of the 1999 data in this Δm region.

Chapter 5

The Final Results

5.1 The Chargino Candidates

The final results from the DELPHI chargino analysis were obtained by using both the data from year 1999 and the year 2000. The data recorded during 1999 was divided into four samples with the mean center–of–mass energy 192, 196, 200 and 202 GeV. The total data corresponded to a integrated luminosity of 227 pb^{-1}. The event selection of the different data samples from year 1999 was performed with a likelihood ratio function optimized at $\sqrt{s}$ = 200 GeV and for the individual topologies and Δm regions. The number of selected candidates and the corresponding number of events predicted by the SM are shown in table 5.1. The data – MC agreement is excellent with the exception of the fourth $jj\ell$ window which was discussed in the previous chapter.

The data collected during year 2000 was divided into three samples with the mean center–of–mass energies 205, 207 and 208 GeV. These samples corresponded to an integrated luminosity of 164.4 pb^{-1} (during the period where the TPC sector 6 was working correctly (C1)). The data collected during the period where the TPC sector 6 was not working (S1) was included as a separate sample with $\sqrt{s}$ = 206.3 GeV and an integrated luminosity of 60.0 pb^{-1}. The total number of candidates in the 2000 data with and without the TPC sector 6 are given in table 5.2 and 5.3 respectively. The year 2000 C1 data is in a very good agreement with the expected SM background in all of the search windows and no significant excess is seen. Also the data – MC agreement for the S1 data is very good, with a somewhat larger deviation in the $\ell\ell$ topology in the Δm region one, where there are 10 data events but 18.8 are expected from the SM background. This discrepancy corresponds only to a 2.0σ deviation, but it has been investigated and one observed small problems at the preselection level in this window[2]. These problems only affected the first Δm region and mainly the analysis of the year 2000 S1 data. This search window, due to the low multiplicity and low visible energy, contains the events that are the most difficult to simulate accurately and hence one could suspect that this discrepancy originates from problems with the simulation of the detector response. The lack of observed events in this search window is of course not due to a chargino signal and the deviation was included in the systematic error which was propagated into the computation of the chargino exclusion limits.

5.2 The Efficiency Estimation

The chargino detection efficiency was calculated from simulations of the signal made by the SUSYGEN program [21] for the different points in figure 3.5, in the parameter space (M_2, μ, $\tan\beta$, m_0). From this a parametrization of the efficiency can be made for any arbitrary parameter

Stable $\tilde{\chi}^0_1$ 1999 data, $\mathcal{L} = 227\ pb^{-1}$

Topology:	$jj\ell$	$\ell\ell$	*jets*	rad	Total
	$3 \leq \Delta m < 5$ GeV/c^2				
Obs. events:	4	39	3	7	53
Expect. events:	$2.3^{+1.2+1.2}_{-0.2-0.1}$	$49.2^{+3.2+2.6}_{-2.0-5.7}$	$5.3^{+1.4+0.0}_{-0.5-2.7}$	$5.3^{+1.2+0.9}_{-0.3-0.2}$	$62.1^{+4.0+3.0}_{-2.2-6.3}$
	$5 \leq \Delta m < 10$ GeV/c^2				
Obs. events:	4	13	1	7	25
Expect. events:	$2.3^{+1.2+1.2}_{-0.2-0.1}$	$11.9^{+1.9+0.5}_{-0.7-3.0}$	$2.5^{+1.2+0.5}_{-0.3-0.7}$	$5.3^{+1.2+0.9}_{-0.3-0.2}$	$22.0^{+2.9+1.6}_{-0.9-3.1}$
	$10 \leq \Delta m < 25$ GeV/c^2				
Obs. events:	4	14	17	7	42
Expect. events:	$2.3^{+1.2+1.2}_{-0.2-0.1}$	$14.3^{+1.6+1.7}_{-0.4-3.1}$	$15.8^{+1.9+2.1}_{-0.9-1.4}$	$5.3^{+1.2+0.9}_{-0.3-0.2}$	$37.6^{+3.0+3.1}_{-1.1-3.4}$
	$25 \leq \Delta m < 35$ GeV/c^2				
Obs. events:	6	21	10	7	44
Expect. events:	$2.2^{+0.4+0.7}_{-0.1-0.0}$	$25.1^{+1.6+4.2}_{-0.5-3.5}$	$8.3^{+0.4+0.8}_{-0.2-0.0}$	$5.3^{+1.2+0.9}_{-0.3-0.2}$	$40.6^{+2.2+4.4}_{-0.7-3.5}$
	$35 \leq \Delta m < 50$ GeV/c^2				
Obs. events:	2	40	28	14	84
Expect. events:	$2.3^{+0.3+0.7}_{-0.0-0.1}$	$45.1^{+1.8+3.1}_{-0.6-4.2}$	$23.6^{+0.5+3.4}_{-0.4-0.4}$	$12.9^{+1.2+1.7}_{-0.3-0.2}$	$84.1^{+2.2+4.9}_{-0.8-4.2}$
	$50 \leq \Delta m$				
Obs. events:	9	60	37	14	120
Expect. events:	$7.5^{+0.5+2.2}_{-0.2-0.3}$	$68.2^{+1.9+4.4}_{-0.8-6.9}$	$36.8^{+0.6+4.9}_{-0.4-0.4}$	$12.9^{+1.2+1.7}_{-0.3-0.2}$	$125.4^{+2.4+7.1}_{-1.0-6.9}$
	TOTAL (logical .OR. between different Δm windows)				
Obs. events:	14	109	54	15	192
Expect. events:	$10.7^{+1.3}_{-0.3}$	$126.1^{+3.7}_{-2.4}$	$52.8^{+2.2}_{-1.3}$	$13.9^{+1.3}_{-0.4}$	$202.6^{+4.7}_{-2.8}$

Table 5.1: The number of selected candidates in the individual topologies and Δm regions for the data recorded during the year 1999. The expected number of SM events is also shown together with the corresponding statistical and systematic errors.

point. A signal event sample of 3000 events was generated at each center–of–mass energy by SUSYGEN in up to 132 parameter points[1]. At each point, the total chargino detection efficiency within the corresponding topologies could be computed by applying the selection procedure to the simulated signal event sample. Although the four topologies are dominated by the decay channel referred to by the topology name (e.g. a signal in the leptonic topology would normally be dominated by chargino events decaying through the leptonic decay channel $\tilde{\chi}^+ \to \ell^+\nu\tilde{\chi}^0$) the events selected into one topology might of course be a combination of events originating from all four decay channels. In order to apply the efficiency for a give topology to an expected signal, the fraction of the selected signal must be evaluated for that specific topology, including the topological selection of events after simulating the DELPHI detector response. For this reason it is much more convenient to present the detection efficiencies for each decay channel since this can then be compared with an expected signal which can be obtained directly from the cross section, branching ratio and the corresponding integrated luminosity. From the simulated signal events at each point in the SUSY parameter space the efficiency could be computed for the

[1]For the samples with a center–of–mass energy below 208 GeV some point are not kinematically accessible, e.g. a point corresponding to a chargino mass equal to $m_{\tilde{\chi}^\pm} = 103$ GeV/c^2 is not accessible for a sample with a center–of–mass energy $\sqrt{s} = 200$ GeV .

Stable $\tilde{\chi}_1^0$ $< E_{cm} > = 206$ GeV, $\mathcal{L} = 164.4\ pb^{-1}$

Topology:	$jj\ell$	$\ell\ell$	$jets$	rad	Total
	$3 \leq \Delta m < 5$ GeV$/c^2$				
Obs. events:	0	20	5	3	28
Expect. events:	$0.4\ ^{+1.2+0.1}_{-0.1-0.0}$	$20.6\ ^{+2.6+0.3}_{-1.6-2.4}$	$7.5\ ^{+1.6+1.3}_{-0.8-0.6}$	$2.5\ ^{+1.4+1.1}_{-0.2-0.1}$	$31.0\ ^{+3.6+1.7}_{-1.8-2.5}$
	$5 \leq \Delta m < 10$ GeV$/c^2$				
Obs. events:	0	0	2	3	5
Expect. events:	$0.4\ ^{+1.2+0.1}_{-0.1-0.0}$	$2.0\ ^{+1.4+0.1}_{-0.4-0.5}$	$1.4\ ^{+1.3+0.5}_{-0.2-0.3}$	$2.5\ ^{+1.4+1.1}_{-0.2-0.1}$	$6.4\ ^{+2.6+1.2}_{-0.5-0.6}$
	$10 \leq \Delta m < 25$ GeV$/c^2$				
Obs. events:	0	8	4	3	15
Expect. events:	$0.4\ ^{+1.2+0.1}_{-0.1-0.0}$	$7.7\ ^{+1.7+0.9}_{-0.6-0.4}$	$5.6\ ^{+1.4+1.3}_{-0.5-0.5}$	$2.5\ ^{+1.4+1.1}_{-0.2-0.1}$	$16.3\ ^{+2.9+1.9}_{-0.8-0.6}$
	$25 \leq \Delta m < 35$ GeV$/c^2$				
Obs. events:	1	13	3	3	20
Expect. events:	$0.4\ ^{+1.2+0.0}_{-0.0-0.0}$	$11.6\ ^{+1.6+0.7}_{-0.5-2.1}$	$4.0\ ^{+1.3+1.0}_{-0.4-0.0}$	$2.5\ ^{+1.4+1.1}_{-0.2-0.1}$	$18.5\ ^{+2.8+1.6}_{-0.7-2.1}$
	$35 \leq \Delta m < 50$ GeV$/c^2$				
Obs. events:	2	23	10	11	46
Expect. events:	$2.4\ ^{+1.3+0.1}_{-0.2-0.1}$	$26.8\ ^{+1.7+1.2}_{-0.7-2.8}$	$8.0\ ^{+1.4+2.0}_{-0.4-0.0}$	$10.3\ ^{+1.3+1.6}_{-0.5-0.5}$	$47.5\ ^{+2.9+2.8}_{-0.9-2.8}$
	50 GeV$/c^2 \leq \Delta m$				
Obs. events:	3	40	22	11	76
Expect. events:	$3.8\ ^{+1.3+0.4}_{-0.2-0.3}$	$38.9\ ^{+1.7+4.3}_{-0.7-1.1}$	$18.7\ ^{+1.4+4.2}_{-0.6-0.0}$	$10.3\ ^{+1.3+1.6}_{-0.5-0.5}$	$71.7\ ^{+2.9+6.2}_{-1.0-1.2}$
	TOTAL (logical .OR. between different Δm windows)				
Obs. events:	4	76	31	11	122
Expect. events:	$5.0\ ^{+1.4}_{-0.3}$	$69.7\ ^{+3.1}_{-2.1}$	$29.0\ ^{+1.9}_{-1.1}$	$10.9\ ^{+1.4}_{-0.5}$	$114.6\ ^{+4.1}_{-2.4}$

Table 5.2: The number of selected candidates in the individual topologies and Δm regions for the data recorded during the year 2000 during the period with the TPC sector 6 ON. The expected number of SM events is also shown together with the corresponding statistical and systematic error respectively.

separate decay channels as

$$\varepsilon^i = \frac{\sum\limits_{topo} N_{selected\ from\ decay\ channel\ i}}{N_{total\ from\ decay\ channel\ i}} \tag{5.1}$$

where $N_{selected\ from\ decay\ channel\ i}$ is the number of events selected by the likelihood ratio selection constructed for the Δm region related to the SUSY point and for the corresponding topology.

After that the efficiency for the different decay channels was calculated for the 132 points and a parametrization was made to get the efficiency at an arbitrary point. The efficiency was parametrized in the $m_{\tilde{\chi}^\pm}$–Δm plane (where $\Delta m = m_{\tilde{\chi}^\pm} - m_{\tilde{\chi}_2^0}$ for the radiative decay channel) in 1 GeV$/c^2$ steps. First the parametrization was made for all values which were surrounded by three of the simulated SUSY points. In this case the values inside the triangle were obtained by a linear interpolation based on the efficiency at the three simulated points. The remaining points after the triangular interpolation within the accessible region in the $m_{\tilde{\chi}^\pm}$–Δm plane were determined by setting them equal to the closest value independent of if it was a simulated point or not.

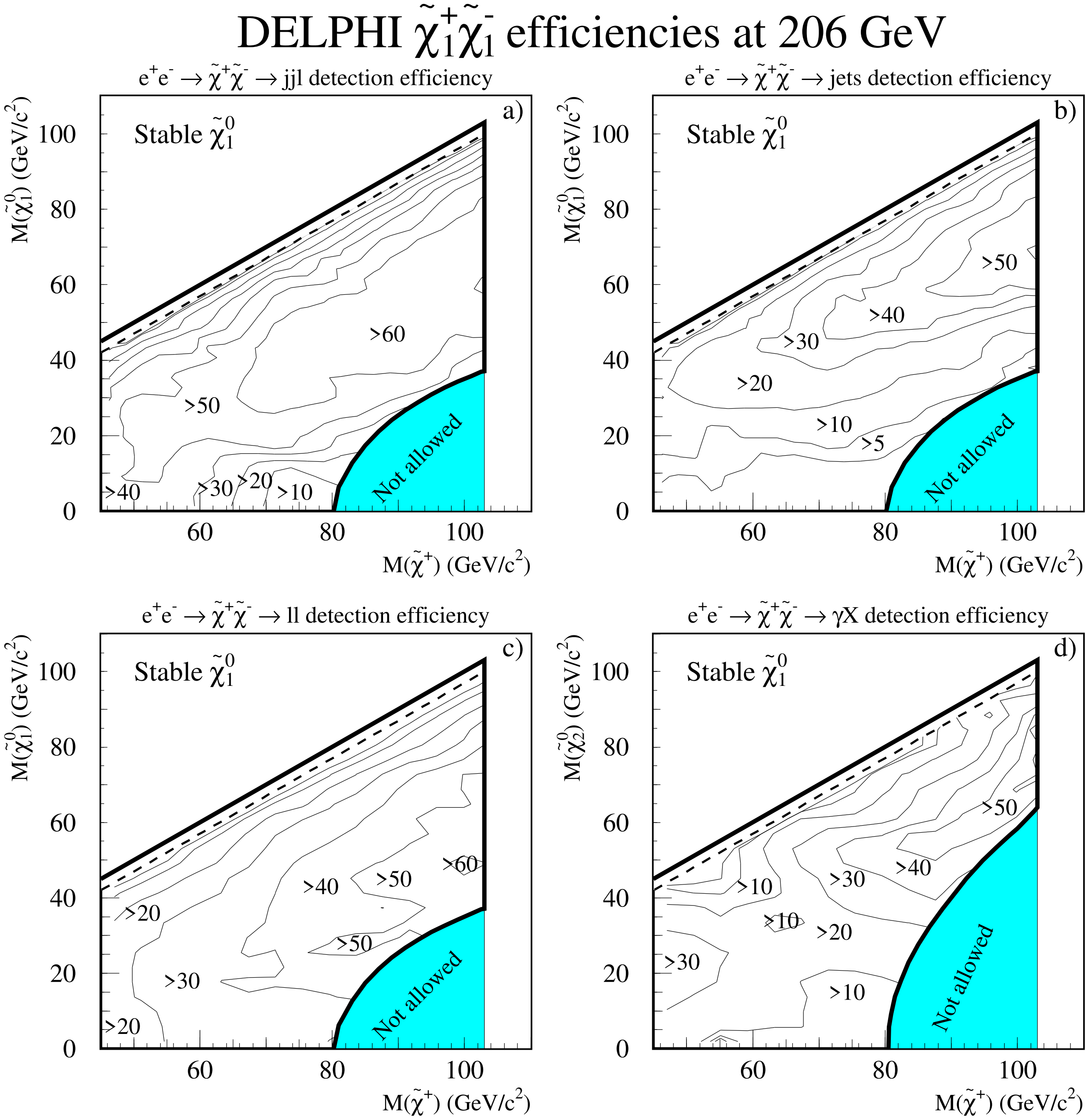

Figure 5.1: The detection efficiency for the four chargino decay channels from the analysis of the 2000 data with the TPC sector 6 ON.

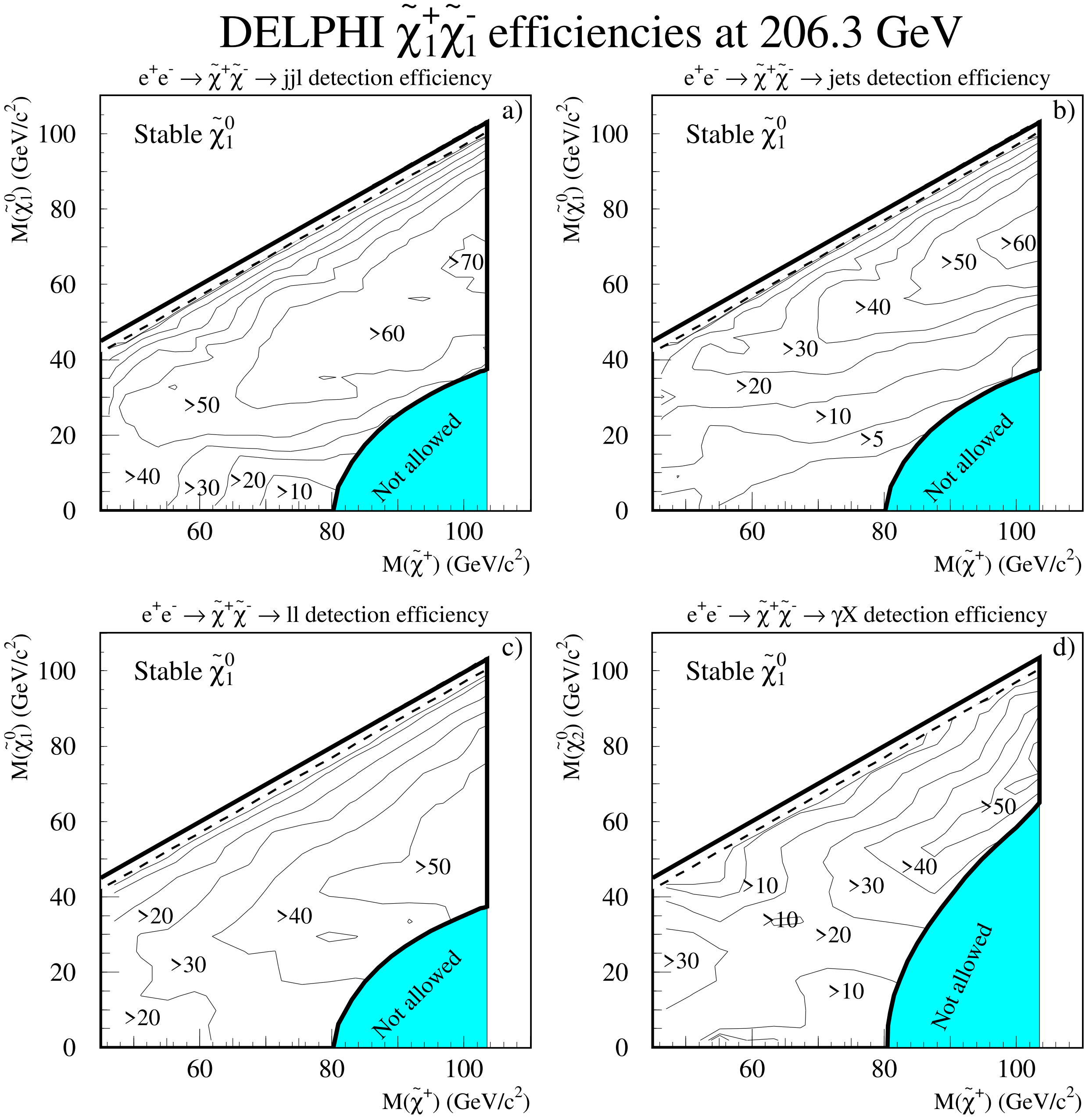

Figure 5.2: The detection efficiency for the four chargino decay channels from the analysis of the 2000 data with the TPC sector 6 OFF.

Stable $\tilde{\chi}^0_1$ $E_{cm} = 206.3$ GeV, $\mathcal{L} = 60.0\ pb^{-1}$

Topology:	$jj\ell$	$\ell\ell$	$jets$	rad	Total
	$3 \leq \Delta m < 5$ GeV/c^2				
Obs. events:	0	10	2	2	14
Expect. events:	$0.2\ ^{+0.5+0.1}_{-0.0-0.0}$	$18.8\ ^{+1.5+0.0}_{-1.1-4.0}$	$2.1\ ^{+0.8+0.9}_{-0.4-0.0}$	$1.3\ ^{+0.5+1.0}_{-0.1-0.0}$	$22.5\ ^{+1.8+1.3}_{-1.2-4.0}$
	$5 \leq \Delta m < 10$ GeV/c^2				
Obs. events:	0	4	4	2	10
Expect. events:	$0.2\ ^{+0.5+0.1}_{-0.0-0.0}$	$3.6\ ^{+0.8+0.0}_{-0.4-0.5}$	$3.9\ ^{+1.0+2.3}_{-0.6-0.1}$	$1.3\ ^{+0.5+1.0}_{-0.1-0.0}$	$9.1\ ^{+1.4+2.5}_{-0.7-0.5}$
	$10 \leq \Delta m < 25$ GeV/c^2				
Obs. events:	0	3	7	2	12
Expect. events:	$0.20\ ^{+0.5+0.1}_{-0.0-0.0}$	$2.31\ ^{+0.6+0.0}_{-0.2-0.4}$	$5.4\ ^{+1.0+2.7}_{-0.6-0.0}$	$1.3\ ^{+0.5+1.0}_{-0.1-0.0}$	$9.3\ ^{+1.3+2.9}_{-0.7-0.4}$
	$25 \leq \Delta m < 35$ GeV/c^2				
Obs. events:	0	3	4	2	9
Expect. events:	$0.4\ ^{+0.5+0.1}_{-0.0-0.1}$	$5.3\ ^{+0.6+0.0}_{-0.2-2.2}$	$3.2\ ^{+0.7+1.2}_{-0.3-0.0}$	$1.3\ ^{+0.5+1.0}_{-0.1-0.0}$	$10.3\ ^{+1.1+1.6}_{-0.4-2.2}$
	$35 \leq \Delta m < 50$ GeV/c^2				
Obs. events:	0	10	6	5	21
Expect. events:	$0.7\ ^{+0.4+0.0}_{-0.0-0.1}$	$11.7\ ^{+0.7+0.0}_{-0.3-5.2}$	$5.0\ ^{+0.6+2.1}_{-0.3-0.0}$	$4.3\ ^{+0.5+1.3}_{-0.2-0.0}$	$21.6\ ^{+1.1+2.5}_{-0.4-5.2}$
	50 GeV/$c^2 \leq \Delta m$				
Obs. events:	1	16	9	5	31
Expect. events:	$2.0\ ^{+0.5+0.0}_{-0.1-0.6}$	$14.2\ ^{+0.6+4.1}_{-0.3-1.1}$	$6.3\ ^{+0.6+2.4}_{-0.2-0.0}$	$4.3\ ^{+0.5+1.3}_{-0.2-0.0}$	$26.8\ ^{+1.1+4.9}_{-0.4-1.3}$
	TOTAL (logical .OR. between different Δm windows)				
Obs. events:	1	31	16	5	53
Expect. events:	$2.3\ ^{+0.5}_{-0.1}$	$38.8\ ^{+1.7}_{-1.2}$	$13.1\ ^{+1.2}_{-0.8}$	$4.5\ ^{+0.5}_{-0.2}$	$58.7\ ^{+2.2}_{-1.5}$

Table 5.3: The number of selected candidates in the individual topologies and Δm regions for the data recorded during the year 2000 during the period with the TPC sector 6 OFF. The expected number of SM events is also shown together with the corresponding statistical and systematic error respectively.

Figure 5.1 and 5.2 shows the efficiency for the four different decay channels for the analysis of the data recorded during the year 2000 with and without sector 6. All the efficiency plots shows a maximum efficiency in the medium Δm region which increases with an increasing chargino mass. The efficiency decrease rapidly at lover Δm values. There are scenarios in the mSUGRA model where very low Δm values are allowed, but this region is investigated by other analysis specialized for that purpose and in this analysis searches are only performed down to a Δm value of 3 GeV/c^2. The efficiency becomes lower also at very high Δm values. This is due to the almost irreducible WW background. An interesting observation is that the efficiency is in general highest in the $jj\ell$ decay channel where it is above 60% in a large part of the parameter space. One can further more see in section 5.1 that the $jj\ell$ topology which normally should contain a large fraction of the events from the $jj\ell$ decay channel have a very low SM background contamination and there is a high probability that the $jj\ell$ would be the topology where a chargino signal would be observed first. From the efficiencies of the four decay channels the total detection efficiency can be computed as

$$\begin{aligned}\varepsilon^{tot}\ (m_{\tilde{\chi}^\pm}, m_{\tilde{\chi}_1^0}, m_{\tilde{\chi}_2^0}, B_\ell, P_\gamma) = \ & [B_\ell^2 \cdot \varepsilon^{\ell\ell}\ (m_{\tilde{\chi}^\pm}, m_{\tilde{\chi}_1^0}) + \\ & 2B_\ell\,(1-B_\ell)\cdot\varepsilon^{jj\ell}\ (m_{\tilde{\chi}^\pm}, m_{\tilde{\chi}_1^0}) + \\ & (1-B_\ell)^2\cdot\varepsilon^{jj}\ (m_{\tilde{\chi}^\pm}, m_{\tilde{\chi}_1^0})\ ]\cdot(1-P_\gamma)\ + \\ & \varepsilon^{rad}\ (m_{\tilde{\chi}^\pm}, m_{\tilde{\chi}_1^0}, m_{\tilde{\chi}_2^0})\ \cdot P_\gamma\end{aligned} \tag{5.2}$$

where $\varepsilon^{\ell\ell}\ (m_{\tilde{\chi}^\pm}, m_{\tilde{\chi}_1^0})$, $\varepsilon^{jj\ell}\ (m_{\tilde{\chi}^\pm}, m_{\tilde{\chi}_1^0})$, $\varepsilon^{jj}\ (m_{\tilde{\chi}^\pm}, m_{\tilde{\chi}_1^0})$ and $\varepsilon^{rad}\ (m_{\tilde{\chi}^\pm}, m_{\tilde{\chi}_1^0}, m_{\tilde{\chi}_2^0})$ are the efficiencies for each decay channel, B_ℓ the leptonic branching ratio and P_γ the probability to have at least one photon in the event originating from a radiative cascade decay ($\tilde{\chi}_2^0 \to \tilde{\chi}_1^0\gamma$).

The multichannel Bayesian method (see section 5.3) was used for the final chargino exclusion limits in order to take advantage of the fact that the analysis was made separately for the different search windows. The efficiency for each decay channel had to be obtained for each topology and this was done by computing the efficiency for each decay channel as described above but by using the likelihood ratio function for each topology separately. In this way one obtained 16 efficiency tables, one for each decay channel and topology.

Different methods were used to estimate the systematic error on the detection efficiency. The different methods were applied due to large differences in multiplicity between the topologies. In the jj and $jj\ell$ (high multiplicity) topologies a so called shaking method [2, 26] was used and the systematic error was interpreted as the change in efficiency between the "shaken" and "unshaken" signal event samples. The errors obtained in the first two Δm regions were between 4% and 13%, but in the other regions the errors were below 4%. The "shaking" method gave for all regions a higher efficiency and the "unshaken" efficiencies could be considered as conservative. In the $\ell\ell$ (low multiplicity) topology a so called smearing method [2, 27] was used and the systematic errors were calculated to be about 2%. In the rad (mixed high and low multiplicity) topology both methods were used which gave compatible results and gave systematic errors below 2%. The impact on the final limits from these systematic errors were very low in comparison with the statistical error on the efficiency and the systematic errors on the number of selected SM background events. The statistical errors were obtained by the formula

$$\frac{\sigma_\varepsilon}{\varepsilon} = \sqrt{\frac{(1-\varepsilon)}{\varepsilon}/N_{tot}}\ , \tag{5.3}$$

where N_{tot} is the total number of events used to estimate the efficiency, originating from the binomial distribution.

5.3 The Bayesian Method

In order to interpret the results in terms of confidence limits[2], an upper limit on the signal was computed from the observed number of events using a Bayesian method[28]. A difference between this Bayesian method and the likelihood ratio method [29], is that the Bayesian method needs much less computation time and in the chargino search where the limits are obtained from a scan of the SUSY parameter space the Bayesian method was chosen, since the limit computation would otherwise have required an enormous amount of CPU time.

[2]Refers to a limit obtained at a certain confidence level.

5.3.1 The Mono-Channel Method

The Bayesian formula originates from the definition of conditional probabilities

$$P(A \cap B) = P(A|B)P(B) \ . \tag{5.4}$$

This is illustrated in figure 5.3 which shows two subsets $A, B \subset \Omega$ and where it is shown that the probability of having an outcome within the overlap between A and B is equal to the probability to have an outcome within A given B times the probability to have an outcome within B.

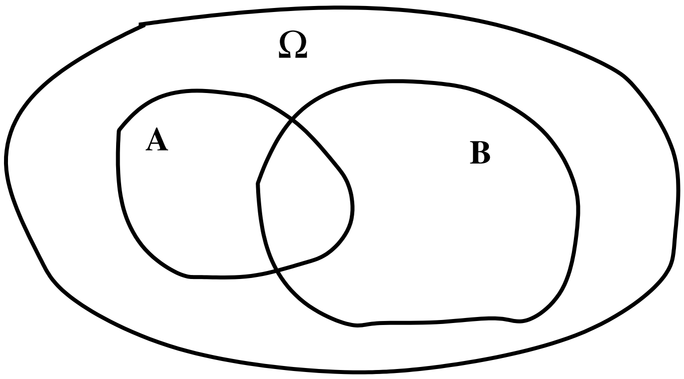

Figure 5.3: The two subsets $A, B \subset \Omega$.

From that definition the equation $P(A \cap B) = P(B \cap A)$ implies that

$$P(A|B)P(B) = P(B|A)P(A) \tag{5.5}$$

which is the so-called Bayes' theorem.

A search for new physics like the chargino analysis is a so-called counting experiment where the numbers of observed events are distributed according to a Poisson distribution. The number of observed events in the experiment might be contaminated by background events which do not originate form the signal process searched for and this has to be taken into account. The probability density function (pdf) for detecting $n_{s\ (b)}$ events from a signal (background) process with a predicted mean value s (b) are then

$$P(n_s|s) = \frac{e^{-s} s^{n_s}}{n_s!} \tag{5.6}$$

and due to the reproductive property of the Poisson distribution the pdf for detecting signal plus background with the mean values s and b becomes

$$P(n|s,b) = \frac{e^{-s} s^{n_s}}{n_s!} \frac{e^{-b} b^{n_b}}{n_b!} = \frac{e^{-(s+b)}(s+b)^n}{n!} = P(n|s+b) \ , \tag{5.7}$$

$$n = n_s + n_b.$$

To compute a confidence interval for the signal mean value (or $s + b$) from an observed number of events, one need to know the pdf $P(s+b|n)$, which can be derived from equation 5.7 and Bayes' theorem under an assumption of the signal. Bayes' theorem gives that

$$P(s+b|n) = \frac{P(n|s+b)P(s+b)}{P(n)} \tag{5.8}$$

which is the pdf of the mean value of $s+b$ for an observed number of events n. If the mean value b can be determined with high accuracy it can be considered as a constant and the pdf can be written only as functions of s[3]. The pdf $P(n)$ is further more equal to

$$P(n) = \int_0^{\infty} P(n|\hat{s}, b) P(\hat{s}) \; d\hat{s} \tag{5.9}$$

which makes it possible to compute a confidence interval for the signal mean value s as

$$CL = \int_{s_1}^{s_2} P(\hat{s}|n, b) \; d\hat{s} = \frac{\int_{s_1}^{s_2} P(n|\hat{s}, b) P(\hat{s}) \; d\hat{s}}{\int_0^{\infty} P(n|\hat{s}, b) P(\hat{s}) \; d\hat{s}} \tag{5.10}$$

To calculate this expression an a priori assumption about the signal pdf has to be made. $P(s)$ is often chosen to be a flat (constant) distribution within the physically allowed region (which was used in the chargino analysis, $s > 0$) since nothing about the expected number of signal events is normally known. This assumption makes it possible to compute an upper limit on the mean signal value at a certain confidence level from the measurement of signal plus background where the background mean value can be accurately determined

$$CL = \frac{\int_0^{s} e^{-\hat{s}} (\hat{s} + b)^n \; d\hat{s}}{\int_0^{\infty} e^{-\hat{s}} (\hat{s} + b)^n \; d\hat{s}} \tag{5.11}$$

5.3.2 The Multi-Channel Method

The mono-channel method can be extended to combine results from different measurements, like results obtained at different center–of–mass energies or with different detectors. If the experiment has been made using N different channels, the total pdf is the product of the individual Poisson distributions,

$$P(s_i|n_i, b_i) = \prod_{i=1}^{N} \frac{e^{-(s_i+b_i)} (s_i + b_i)^{n_i}}{n_i!} = e^{-(s+b)} \prod_{i=1}^{N} \frac{(s_i + b_i)^{n_i}}{n_i!}. \tag{5.12}$$

The pdf can be expressed as a function of only the total signal mean value distributed between the different channels if the distribution of the signal is known (like the signals $\sqrt{s}$-dependence or acceptance dependence). If $p_i = s_i/s$, a pdf that depends only on the total signal mean value becomes

$$P(s|n_i, b_i, p_i) = e^{-(s+b)} \prod_{i=1}^{N} (s + \beta_i)^{n_i} \left[\frac{p_i^{n_i}}{n_i!}\right] \tag{5.13}$$

where $\beta_i = b_i/p_i$. Since the part of the expression in the square brackets is not depending on s, it will be canceled in the Bayesian formula (eq. 5.10) and the confidence level formula for the multi-channel case becomes

$$CL = \int_0^{s} P(\hat{s}|n_i, b_i, p_i) \; d\hat{s} = \frac{\int_0^{s} e^{-\hat{s}} \prod_{i=1}^{N} (\hat{s} + \beta_i)^{n_i} \; d\hat{s}}{\int_0^{\infty} e^{-\hat{s}} \prod_{i=1}^{N} (\hat{s} + \beta_i)^{n_i} \; d\hat{s}} \; . \tag{5.14}$$

5.4 The Chargino Limits

Since no chargino signal was observed in the analysis the results were used to constrain the SUSY parameter space. This was done for the SUGRA scenario which is the most popular SUSY model and where the chargino search is the most important analysis.

[3] A more rigorous derivation can be made by using $P(b) = \delta(\hat{b} - b)$, justified by the high accuracy in the determination of b.

5.4.1 The Limit Computation

In the chargino analysis in DELPHI it was decided to use an extensive scan through the SUGRA parameter space to determine what regions could be excluded and from that obtain an overall chargino mass limit. The scan was performed in several millions of points that were randomly chosen in the intervals $0 < M_2 < 3000$, $-200 < \mu < 200$ and for $\tan\beta = 1,\ 1.5,\ 35$. The gaugino mass unification, $M_1 = \frac{5}{3}\tan^2\theta_W M_2$, was assumed for all points in the scan together with a assumption of heavy sfermions ($m_0 = 1000$ GeV/c^2)(the sneutrino constraint can be relaxed in the low Δm regions, as will be shown later). The following procedure was used in each point:

- The chargino cross section, the decay channel branching ratios, the probability for radiative cascade decays and the chargino and neutralino masses were computed by using SUSYGEN3.
- The total number of expected signal events (N^{tot}_{exp}) was computed from the sum of the products $\varepsilon^{tot}(\sqrt{s}) \cdot \mathcal{L}(\sqrt{s}) \cdot \sigma(\sqrt{s})$ at the different center–of–mass energies.
- The results from the individual topologies (α) at the different center–of–mass energies were combined by using the Bayesian multichannel method. For this one needs the number of observed events in the experiment ($N_{obs,\ \alpha}$), the number of expected SM background events ($N^{bkg}_{exp,\ \alpha}$) and the signal fraction for each channel relative to the total signal distributed in all the channels (S^{frac}_{α}). Due to the different definitions of Δm for the rad decay channel and the others, the number of channels and S^{frac}_{α} had to be determined differently for different scenarios. It was done in the following two step procedure:
  - If the Δm values defined for a non-radiative ($\Delta m^{\ non-rad} = m_{\tilde{\chi}^{\pm}}$- $m_{\tilde{\chi}^0_1}$) and a radiative processes ($\Delta m^{\ rad} = m_{\tilde{\chi}^{\pm}}$- $m_{\tilde{\chi}^0_2}$) belongs to the same Δm region or if the probability to produce a photon through cascade decays is zero, the signal contribution into each topology is computed as

$$P_\alpha = \sum_{j=1}^{4} \varepsilon^j_\alpha \cdot Br^j \ , \ j = \ \jmath\jmath,\ jj\ell,\ \ell\ell \text{ and } rad \tag{5.15}$$

    for each center–of–mass energy in the combination. Here ε^j_α is the efficiency for chargino events from decay channel j to be selected into topology α. If this is not the case and the decay $\tilde{\chi}^0_2 \to \tilde{\chi}^0_1\gamma$ has a probability larger than zero and $\Delta M^{rad} \neq \Delta M^{non-rad}$, eight channels are produced instead of four. The first four corresponds to the channels where the non-radiative signal events contribute and the other four to where only the signal from radiative cascade processes contribute:

$$P'_\alpha = \sum_{j=1}^{3} \varepsilon^j_\alpha \cdot Br^j \ , \ P''_\beta = \varepsilon^4_\beta \cdot Br^4 \tag{5.16}$$

    where P'_α corresponds to the first four channels and P''_β to the other four.
  - The signal fraction between the different channels in the combination can then be computed as

$$S^{frac}_\alpha = \frac{P_\alpha(\sqrt{s}) \cdot \mathcal{L}(\sqrt{s}) \cdot \sigma(\sqrt{s})}{N^{tot}_{exp}} \ , \ \alpha = 1-4 \text{ or } 8. \tag{5.17}$$

    Where α ends at either four or eight depending on the previously discussed $\Delta M^{rad} - \Delta M^{non-rad}$ criteria at the corresponding SUSY point. The number of channels depends both on α and on the number of samples with different center–of–mass energies.

- The number of observed events in the experiment ($N_{obs,\ \alpha}$), the number of expected SM background events ($N^{bkg}_{exp,\ \alpha}$) and the signal fraction for each channel (S^{frac}_{α}) are used by the Bayesian multichannel method to compute an upper limit on the total number of expected signal events at 95% CL (N^{tot}_{95}). The corresponding SUSY point is then regarded as excluded or not from the difference $N^{tot}_{exp} - N^{tot}_{95}$. In order to take the statistical and systematic uncertainties into account $N^{tot}_{exp} - N^{tot}_{95}$ was computed 50000 times while varying the uncertainties randomly, with respect to their distributions and standard deviations, and the SUSY point was considered excluded if $N^{tot}_{exp} - N^{tot}_{95} > 0$ at 95% CL, with respect to the results from the 50000 computations.

This method of producing a mass limit from a scan of the accessible SUSY parameter space was chosen to include the effects from different branching ratios, $\sqrt{s}$ energies etc. in the best way possible. This can be compared to the case where a cross section limit is first obtained which is then interpreted as a mass limit. In this case the model dependence has a much larger impact.

5.4.2 The Obtained Limits

The excluded part from the SUSY parameter scan in the $\mu - M_2$ plane is shown in figure 5.4 for the three assumptions $\tan\beta = 1$, 1.5 and 35. The excluded regions are valid under the assumption of heavy sfermions ($m_0 = 1000$ GeV/c^2) which implies that the chargino decays dominantly by W-decays and that the sneutrino is too heavy to give any significant impact on the chargino production cross section. In all the $\tan\beta$ scenarios the limit seems to become constant for M_2 at high $|\mu|$ values. At high $|\mu|$ values the chargino is almost a pure gaugino and the branching ratios and efficiencies then becomes insensitive to $|\mu|$. Due to this behavior, the chargino mass limit is valid even for $|\mu| > 200$ GeV/c^2 where the chargino mass becomes insensitive to $|\mu|$[4], due to the eigenvalue relation between the relevant parameters (see section 2.2). The assumption of gaugino mass unification provides two additional implications from the excluded part of the parameter space. The scan implies a lower limit on the lightest neutralino mass since $M_1 = 5/3 \tan^2\theta_W M_2$. The point in the parameter scan which sets the lowest neutralino mass limit is shown in figure 5.4d, which is a zoom of figure 5.4a at low $\mu - M_2$ values, and it implies a limit of $m_{\tilde{\chi}^0_1} > 38.2$ GeV/c^2. The lowest neutralino mass limit is obtained for $\tan\beta = 1$ and it is valid under the assumption $m_{\tilde{\nu}} > 1000$ GeV/c^2. This limit can be improved by combining the chargino analysis with other SUSY analysis which have been done at DELPHI to produce the best neutralino limit possible [1].

Another implication from the gaugino mass unification has no impact on the conclusions about figure 5.4 directly but will become important for the chargino mass limits later. In the region where $M_2 >> |\mu|$ the chargino becomes higgsino like (in the same way as it becomes gaugino like when $|\mu| >> M_2$) and for that reason the chargino will have a very weak coupling to the sneutrino. An effect of the gaugino mass unification is that in the region where the chargino is gaugino–like the lightest neutralino and chargino masses will be depending mainly on M_1 and M_2 which implies that the Δm values are large in this region. Both the lightest neutralino and the chargino masses will on the other hand become approximately equal to μ, when $M_2 >> |\mu|$, which implies that one gets very low Δm values in the region where the coupling to the sneutrino is low. For this reason one can note that that SUSY points with a Δm < 10 GeV/c^2 only exists in the very higgsino-like region and the sneutrino mass constraints can be relaxed in this Δm region and the limit becomes valid under the condition that $m_{\tilde{\chi}^\pm} < m_{\tilde{\nu}}$.

The minimum chargino mass limit could be obtained from the excluded region of the scanned parameter space. Figure 5.5 shows the obtained chargino mass limits both as a function of the

[4] Which has been confirmed by a scan over random points beyond $|\mu| > 200$ GeV/c^2 .

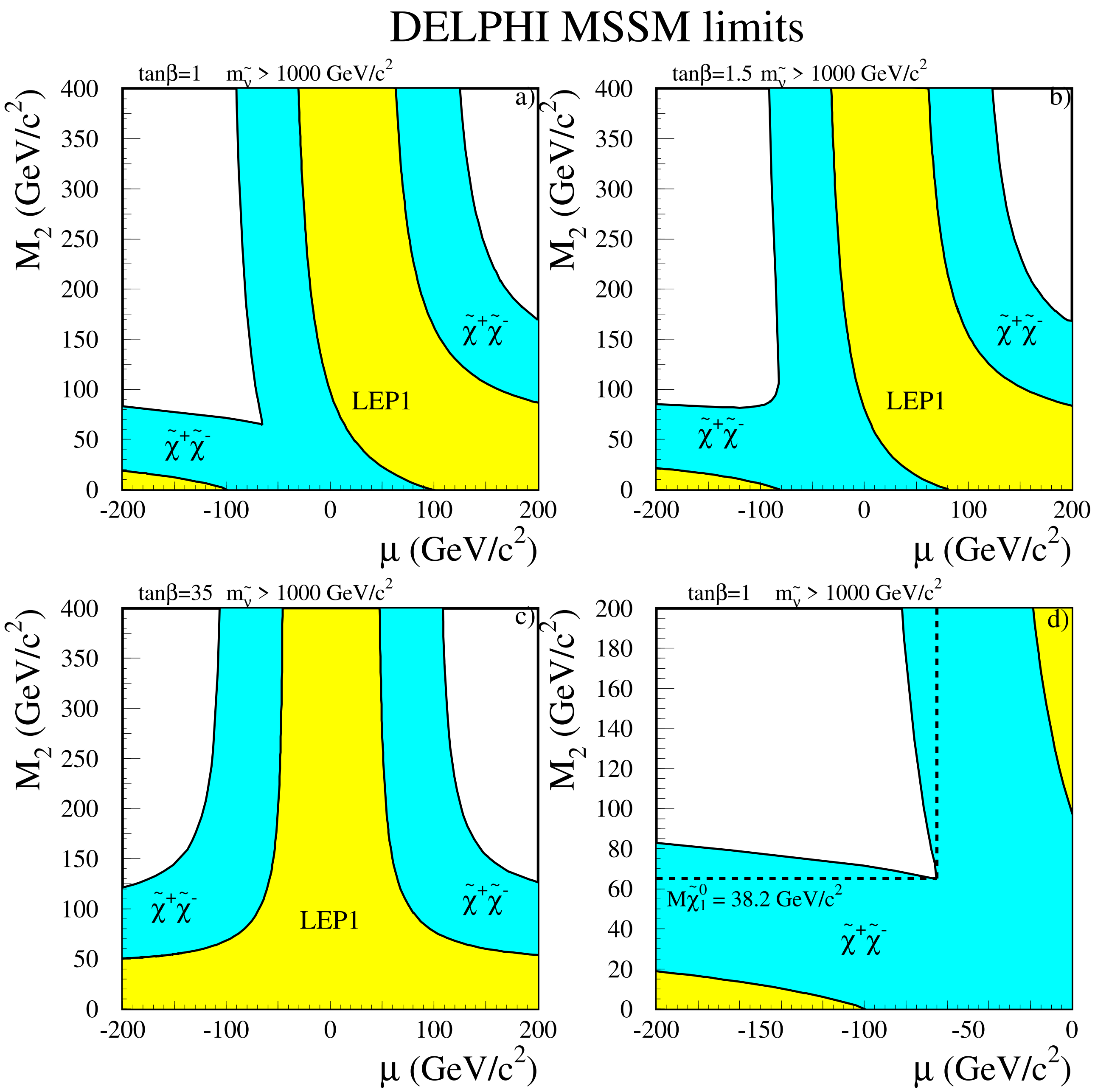

Figure 5.4: The excluded part of the $\mu - M_2$ plane for a) $\tan\beta = 1$, b) $\tan\beta = 1.5$ and c) $\tan\beta = 35$ from the parameter scan. Plot d) shows a zoom of plot a) at small values of μ and M_2, where the implied neutralino mass limit is obtained. The plots are valid for large sfermion masses (m_0 = 1000 GeV/c^2) and under the assumption of gaugino mass unification.

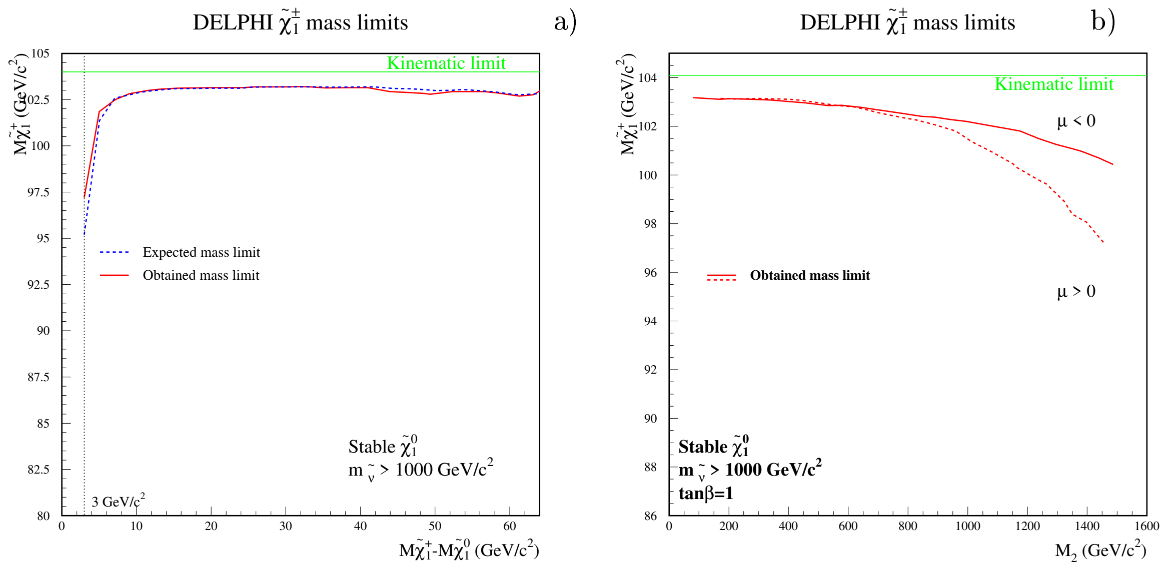

Figure 5.5: The chargino mass limit as a function of a) the Δm values and b) M_2, for $\tan\beta = 1$ (both for positive and negative signs of μ) from the parameter scan. Both limits are valid under the assumption of heavy sfermions (m_0 = 1000 GeV/c^2). This criteria can be relaxed for Δm < 10 GeV/c^2 to $m_{\tilde{\chi}^\pm} < m_{\tilde{\nu}}$. The straight line at the top of the plot represents the kinematically accessible limit.

Δm value (a) and as a function of the M_2 values (b). The mass limit is defined as the lowest chargino mass not excluded in the parameter scan and due to the very dense random scan the resolution only contributes with a 50 MeV/c^2 uncertainty to the mass limit. In figure 5.5a the solid and dashed lines corresponds to the obtained and expected limits respectively and the straight horizontal line at the top of the plot represent the kinematic limit. The plot is valid under the heavy sfermion assumption, but since the limit at Δm < 10 GeV/c^2 is obtained from the part of parameter space where the chargino have a very higgsino-like composition the limit is valid under the relaxed criteria $m_{\tilde{\chi}^\pm} < m_{\tilde{\nu}}$ for this low Δm region. The chargino analysis becomes less sensitive at low Δm values and the overall chargino mass limit is obtained at Δm = 3 GeV/c^2 which is where the analysis starts[5]. The obtained and expected mass limits agree very well except at Δm = 3 GeV/c^2 where it differs with as much as 2 GeV/c^2. This is an effect of the discrepancy in the $\ell\ell$ topology of the year 2000 S1 data. From these results one obtain an overall chargino mass limit of 97.1 GeV/c^2 at Δm = 3 GeV/c^2 , 101.8 GeV/c^2 at Δm = 5 GeV/c^2 ($m_{\tilde{\nu}} > m_{\tilde{\chi}^\pm}$) and 102.7 GeV/$c^2$ for Δm > 10 GeV/c^2 ($m_{\tilde{\nu}}>$ 1000 GeV/c^2). In figure 5.5b the mass limit is shown as a function of M_2 for positive and negative signs of μ. The limit is again valid for heavy sfermion masses (m_0 = 1000 GeV/c^2) and for $\tan\beta = 1$. The limit is lower for positive μ than for negative and this is due to the fact that there is a higher degree of degeneracy between the chargino and the neutralino for positive signs of μ than for negative at a fixed M_2 value.

Figure 5.6 shows the chargino cross sections at $\sqrt{s}$ = 208 GeV from the parameter scan as a function of the chargino mass. Plot 5.6a corresponds to the part of parameter space where Δm > 10 GeV/c^2 and 5.6b to Δm = 3 GeV/c^2 . The minimum cross section that was excluded is also shown which in the case of plot 5.6a is 0.39 pb which corresponds to a chargino mass limit of 102.7 GeV/c^2. In 5.6b it was 1.17 pb and this corresponds to a chargino mass limit of 97.1 GeV/c^2. The figure also shows a larger spread of production cross section for a specific chargino

[5] A specific low Δm chargino search has been performed at DELPHI to investigate the region with Δm < 3 GeV/c^2 [1].

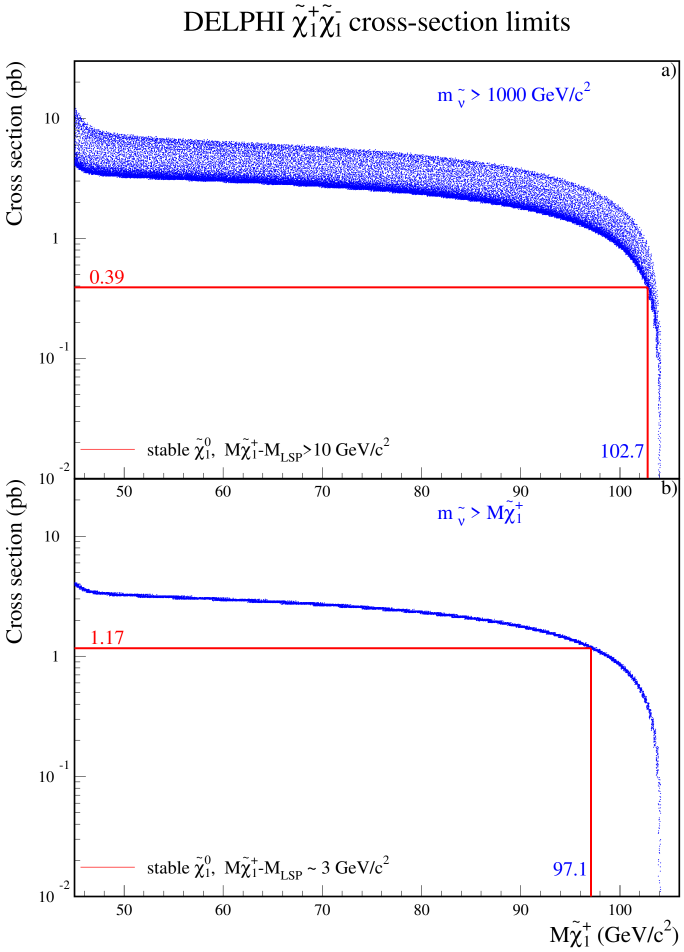

Figure 5.6: The cross sections at $\sqrt{s} = 208$ GeV as a function of the chargino mass. a) corresponds to the points obtained in the region with $\Delta m > 10$ GeV$/c^2$ and b) to the region with $\Delta m = 3$ GeV$/c^2$. The figure also shows the minimal cross sections that where excluded, corresponding to the two mass limits a) 102.7 GeV$/c^2$ and b) 97.1 GeV$/c^2$.

mass in a) than in b). This is due to the much larger variety of chargino composition in the Δm $>$ 10 GeV$/c^2$ case than for Δm = 3 GeV$/c^2$, where the chargino is very higgsino-like. In the large Δm case the highest cross sections for a fixed chargino mass corresponds to a gaugino-like chargino (since $m_{\tilde{\nu}}>$ 1000 GeV$/c^2$) and the lowest cross sections are more higgsino-like.

The results from the chargino analysis were also interpreted as mass limits in the so-called GMSB model and further studies of the validity and stability of the chargino mass limits have been made. These results will not be presented here but they are available in reference[2].

Chapter 6

Conclusions and Summary

A search for charginos as suggested by supersymmetric theories have been made with the DELPHI experiment at LEP. No signal was observed and the results were used to constrain the SUSY parameter space in the SUGRA scenario.

The analysis was based on a likelihood ratio type event selection method which was used to optimize the background suppression for a given signal efficiency. The method was optimized under the assumption that, in the absence of an observed signal, only SM background was measured. This provided a very powerful and convenient tool to maximize the sensitivity of the chargino analysis. The likelihood ratio method was performed separately for four different event topologies and in six Δm regions where the events were investigated using a large number of discriminating variables. The method worked very well after some additional procedures were added to the original likelihood ratio method, in order to minimize statistical effects and effects due to the weak correlation between the discriminating variables.

Case	$m_{\tilde{\nu}}$ (GeV/c^2)	$M_{\chi^\pm}^{min}$ (GeV/c^2)	σ_{min}^{208} (pb)	$N_{95\%}$
$\Delta m > 10$ GeV/c^2	> 1000	102.7	0.39	13.8
$\Delta m = 5$ GeV/c^2	> 1000	101.7	0.57	7.3
$\Delta m = 3$ GeV/c^2	$> m_{\tilde{\chi}_1^\pm}$	97.1	1.17	18.1

Table 6.1: Lower limits of the chargino mass, the minimal pair-production cross-sections at 208 GeV for chargino masses below the limit and upper limits on the number of observed events. The results were obtained from the data recorded at $< E_{cm} >$ = 192-208 GeV.

The results from the event selection was used to excluded the SUSY parameter space by a parameter scan. A very large number of SUSY points where tested to see if the predicted chargino signal was excluded or not with respect to the measurement. From this scan a lower limit on the chargino mass could be extracted and this is given in table 6.1 for three different Δm regions.

The limit is presented for three different Δm regions since the Δm values affects the detection efficiency significantly. The efficiency in general gets lower with decreasing Δm value. The table shows that the overall limit is given by the lowest Δm value, $\Delta m = 3$ GeV/c^2, and corresponds to $m_{\tilde{\chi}^\pm} \geq 97.1$ GeV/c^2. This limit is valid in the SUGRA model under the assumptions of gaugino mass unification and heavy sfermions, but the sneutrino mass only has to exceed the chargino mass in this low Δm region. For $\Delta m \geq 10$ GeV/c^2 the limit increases to $m_{\tilde{\chi}^\pm} \geq 102.7$ GeV/c^2 where the sneutrino mass constraints have to be tighter due to the possible gaugino composition ($m_0 = 1000$ GeV/c^2). This mass limit shows how close to the kinematic limit ($\sqrt{s}/2$) the chargino search could probe.

The search did not discover the chargino but the results contributes to a better understanding of what SUSY cannot look like and the limits constitute some of the strongest constraints on SUSY to date. It is still possible for SUSY to exist since the SUSY particles could have masses of the order of 1 TeV . A significant part of this region was investigated by the LEP experiments and it is now up to the LHC experiments (ATLAS and CMS) to investigate the remaining part.

Appendix A

Data–MC Comparison after Common Selections

This appendix will present a comparison of data and SM simulations after the **common** selection. This is a complement to section 4.4, where only one example from the $jj\ell$ and rad topologies were discussed in detail. A data–MC comparison of the data collected during year 2000 is presented both for the $jj\ell$ and rad topologies and during both the periods with and without the TPC sector 6 working.

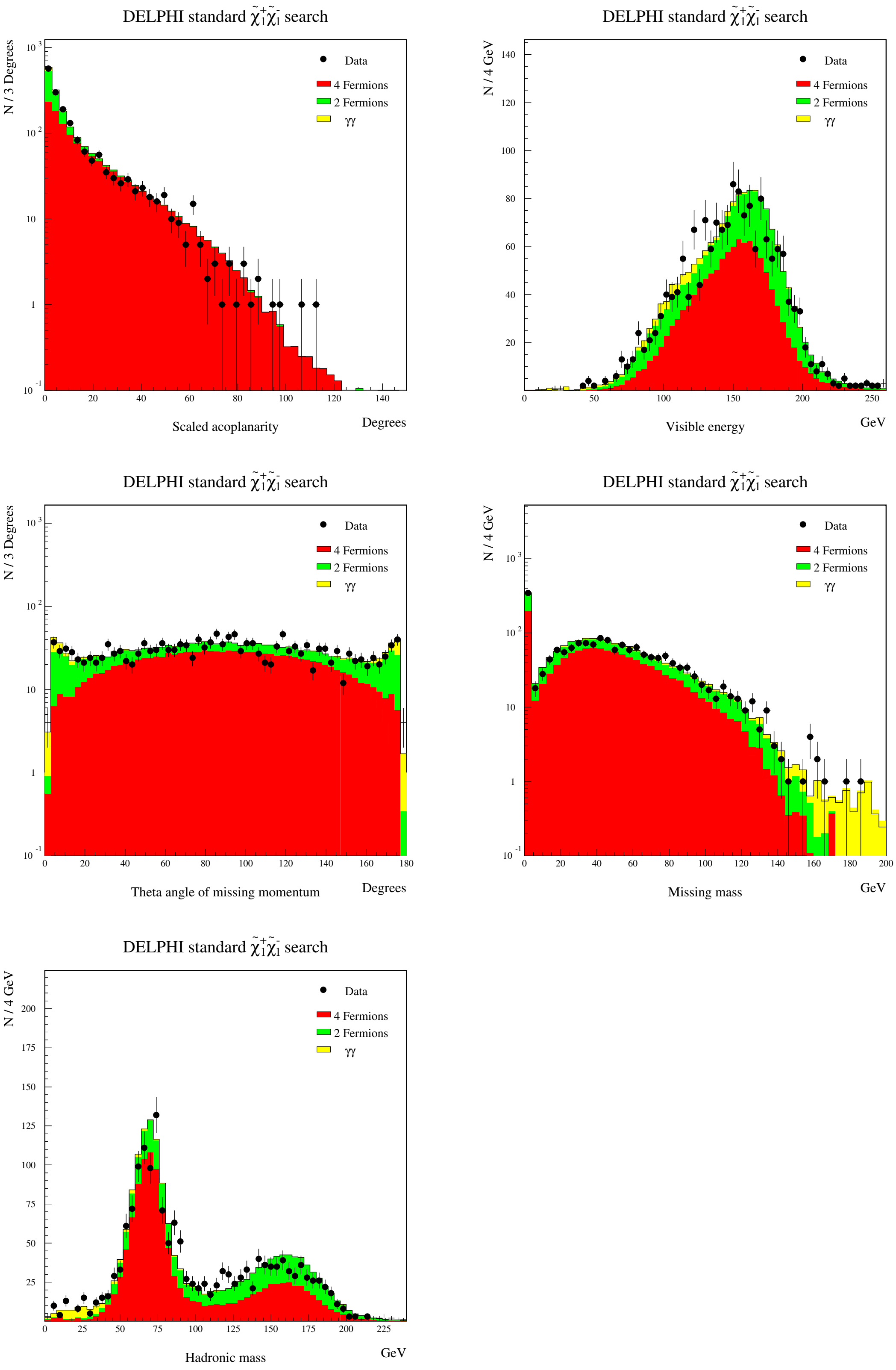

Figure A.1: A data–MC comparison after the *common* selection for the $jj\ell$ topology for the data sample of year 2000 with the TPC sector 6.

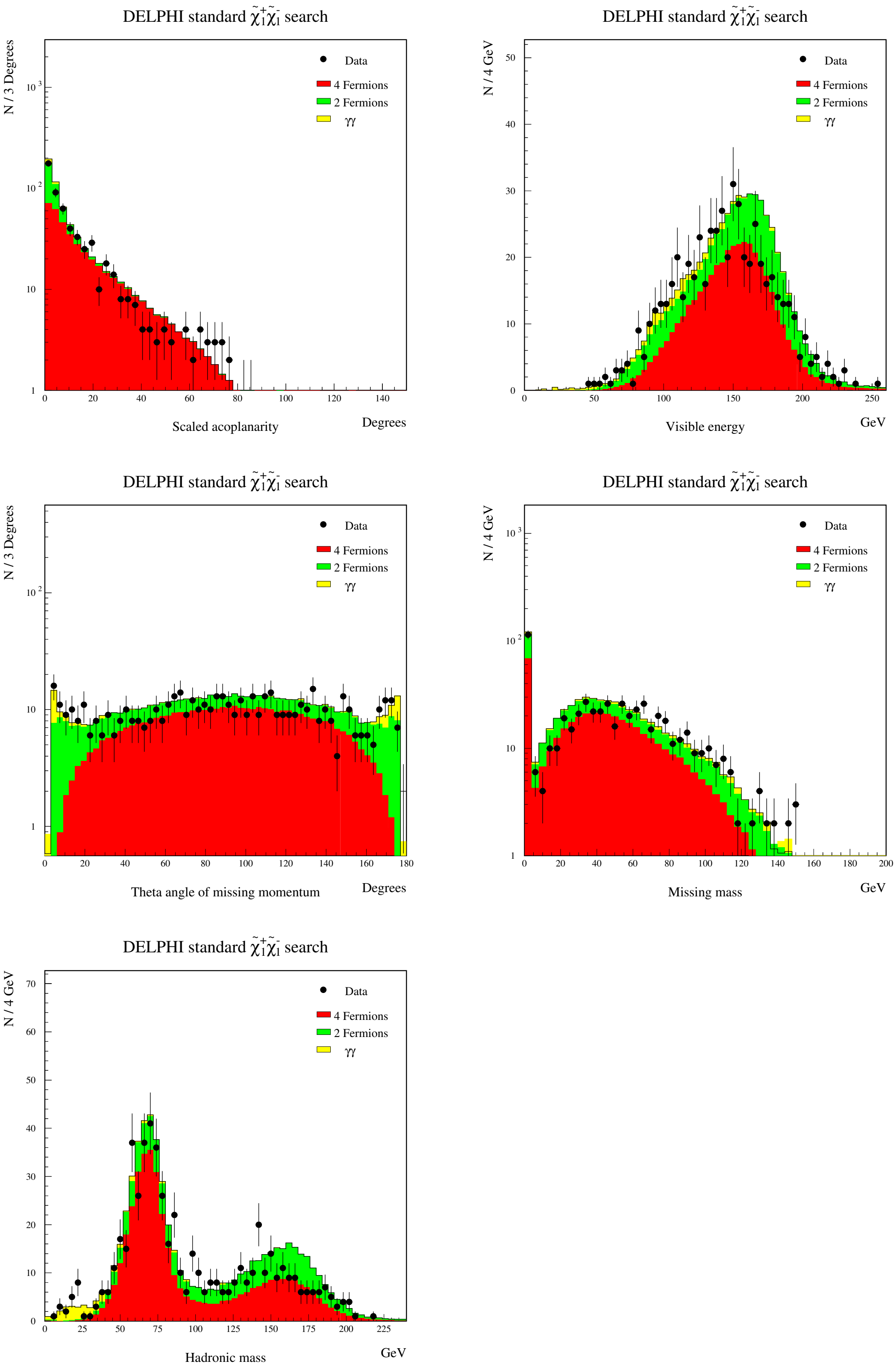

Figure A.2: A data–MC comparison after the *common* selection for the $jj\ell$ topology for the data sample of year 2000 without the TPC sector 6.

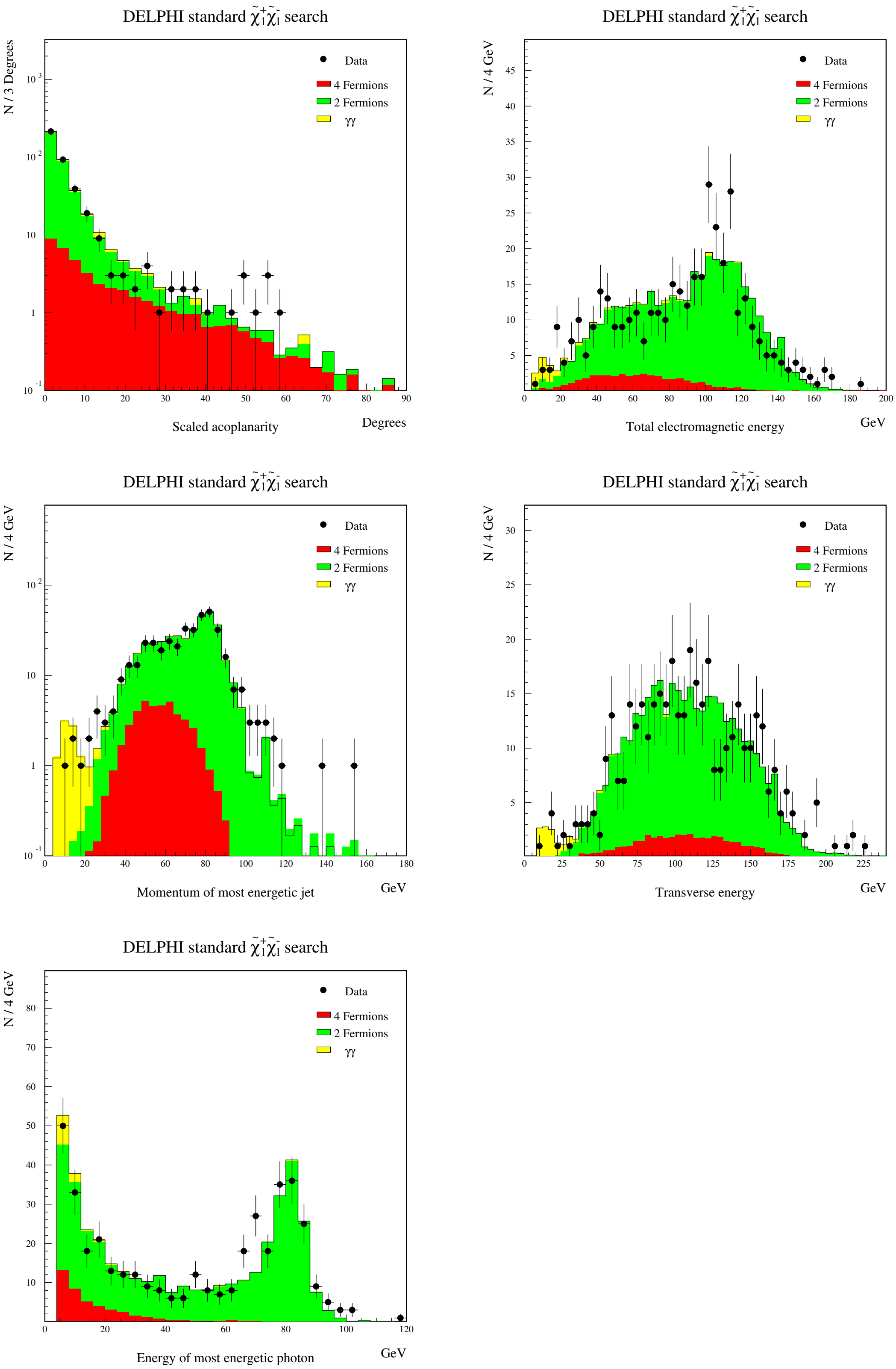

Figure A.3: A data–MC comparison after the *common* selection for the *radiative* topology for the data sample of year 2000 with the TPC sector 6.

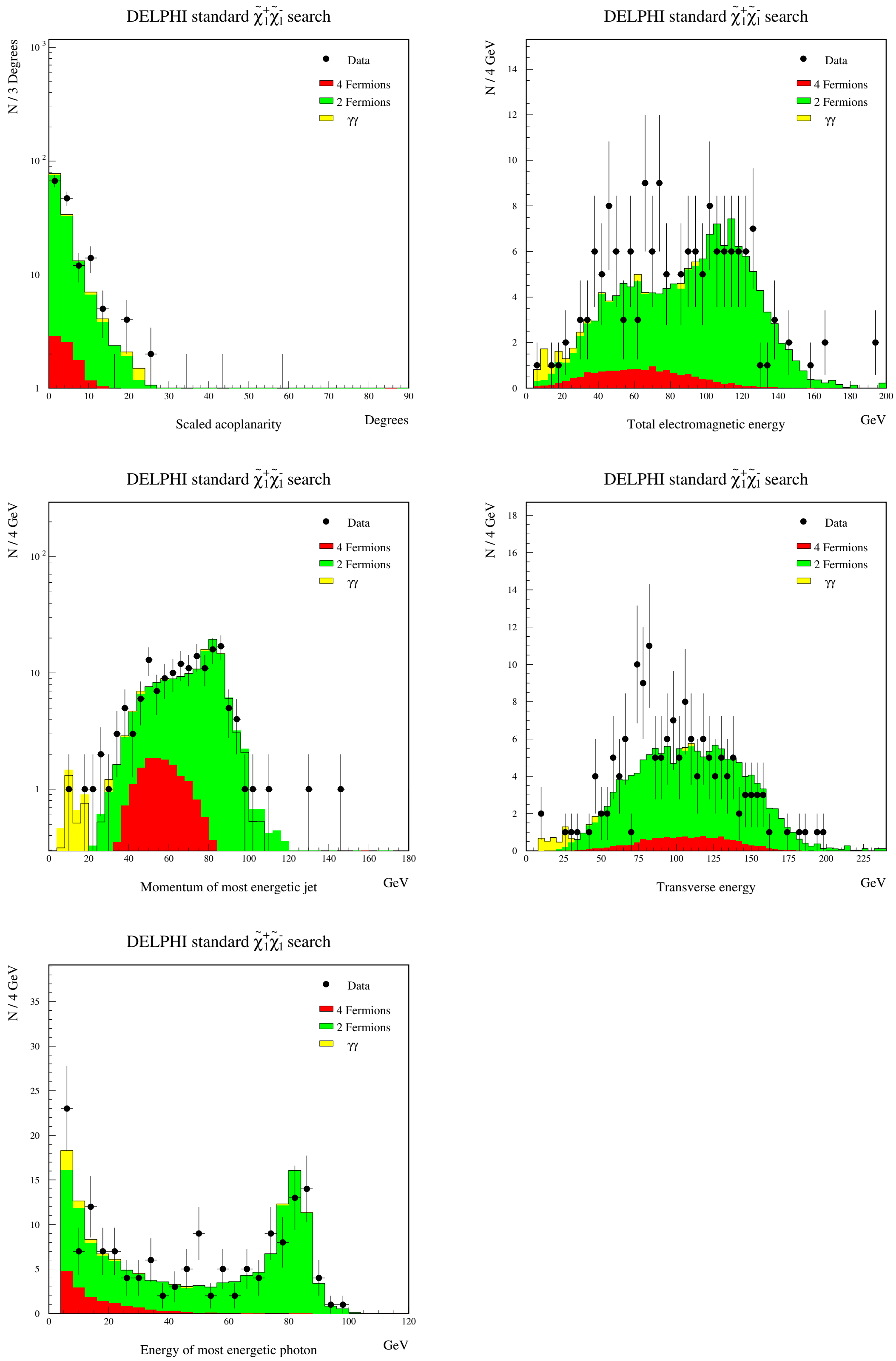

Figure A.4: A data–MC comparison after the *common* selection for the *radiative* topology for the data sample of year 2000 without the TPC sector 6.

Appendix B

Data–MC comparison after Pre- and Final Selection

In this appendix a comparison between data and SM simulations will be presented after both the **preselection** and the **final** selection. This is a complement to the results discussed in detail in section 4.4, since all the different Δm windows will be presented for the $jj\ell$ and rad topologies. Each row represent the distributions after the preselection (left) and the final selection (right), for the same variable. The variables are chosen from the optimal variable set (as described in section 4.2.3). The agreement concerns data collected during year 2000 from both the period with and without the TPC sector 6 working.

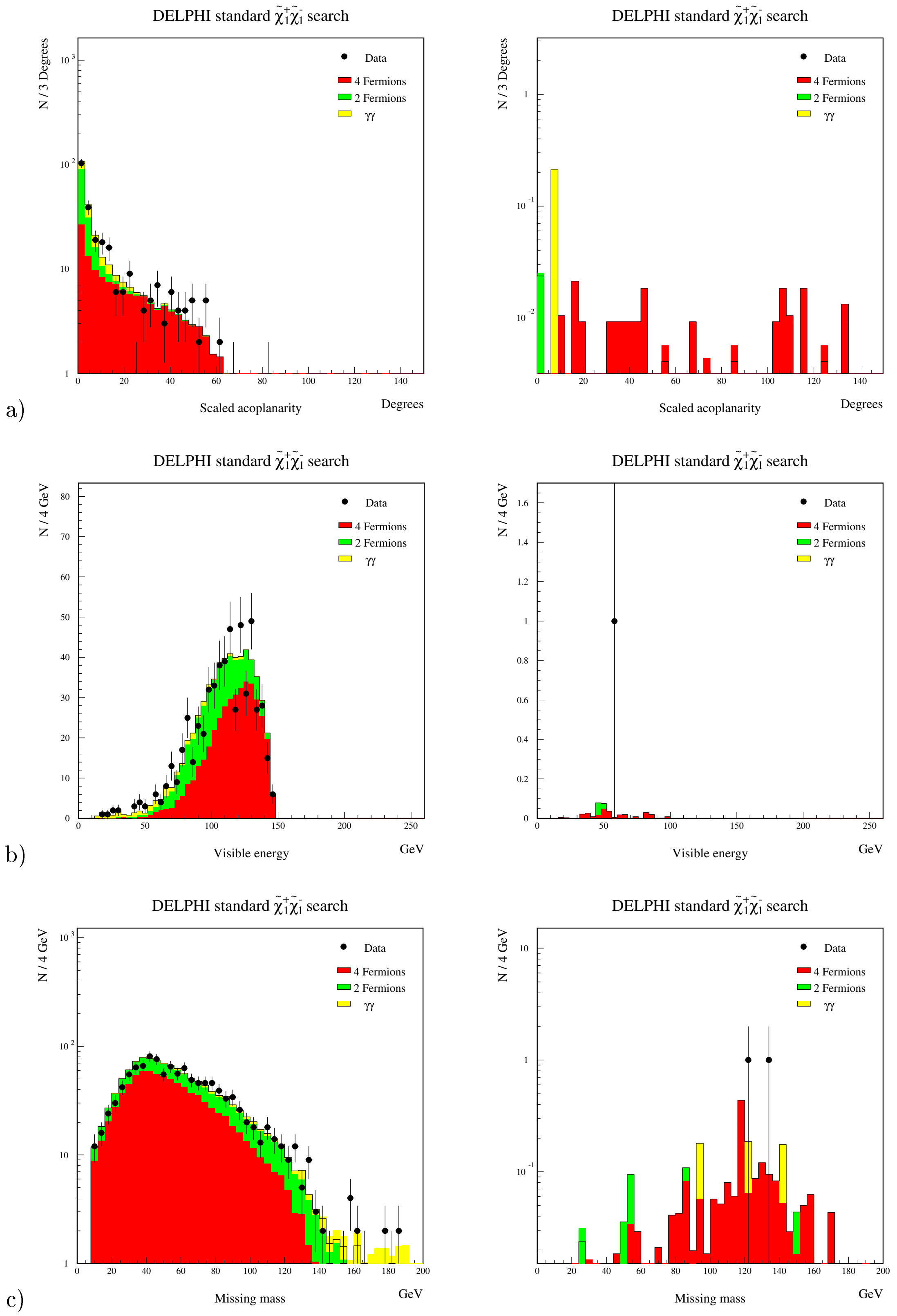

Figure B.1: A data–MC comparison after the preselection and the final selection for the $jj\ell$ topology. The three cases correspond to the Δm regions: a) $3 \leq \Delta m < 25$ GeV$/c^2$, b) $25 \leq \Delta m < 35$ GeV$/c^2$, c) $35 \leq \Delta m < 50$ GeV$/c^2$. The data from year 2000 with TPC sector 6 was used.

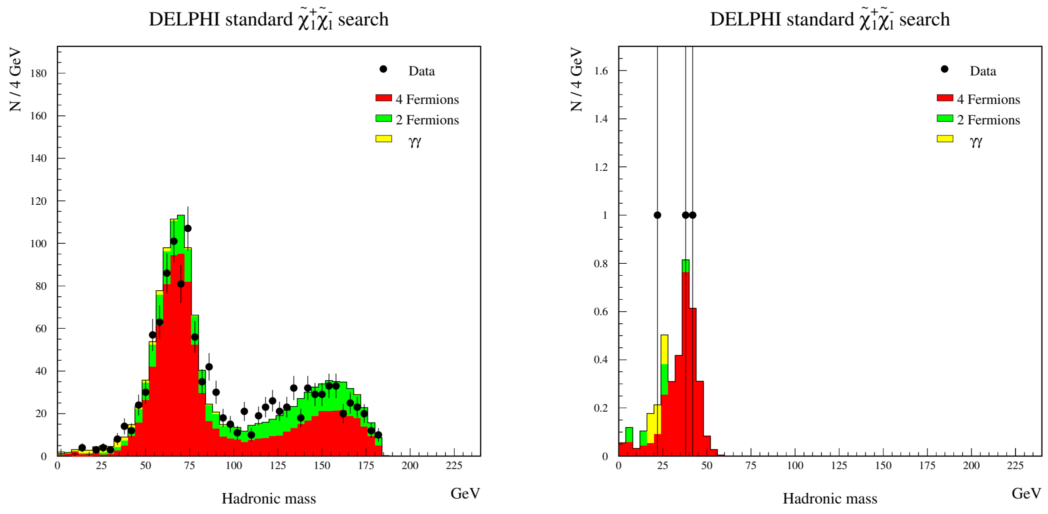

Figure B.2: A data–MC comparison after the preselection and the final selection for the $jj\ell$ topology. The data from year 2000 with TPC sector 6 is shown for the region 50 GeV/$c^2 \leq \Delta m$

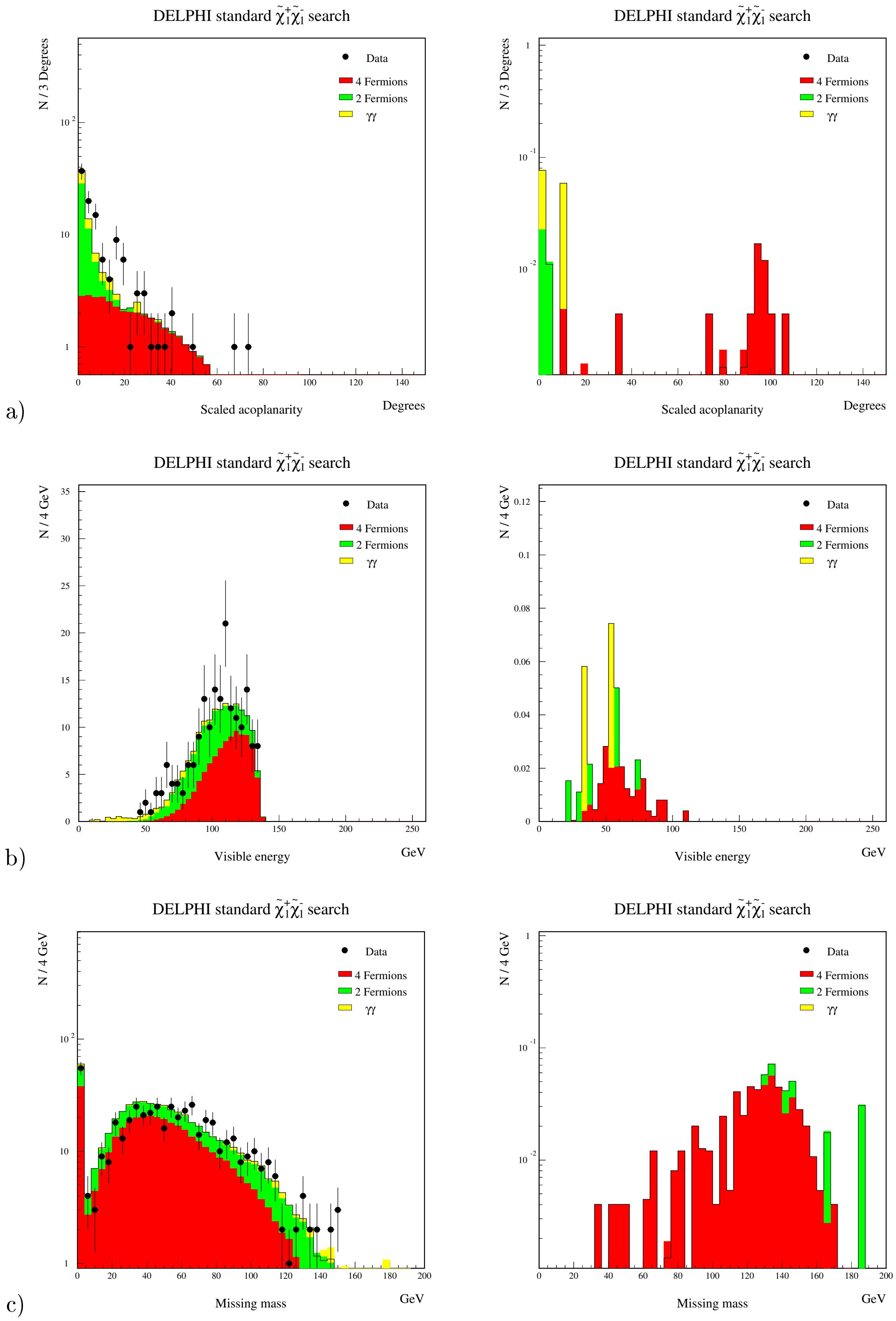

Figure B.3: A data–MC comparison after the preselection and the final selection for the $jj\ell$ topology. The three cases correspond to the Δm regions: a) $3 \leq \Delta m < 25$ GeV$/c^2$, b) $25 \leq \Delta m < 35$ GeV$/c^2$, c) $35 \leq \Delta m < 50$ GeV$/c^2$. The data from year 2000 without TPC sector 6 was used.

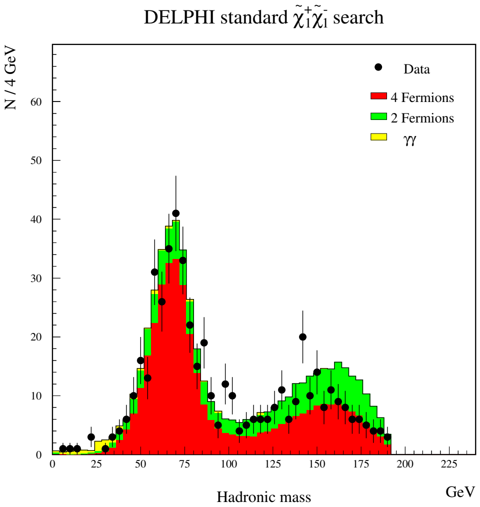

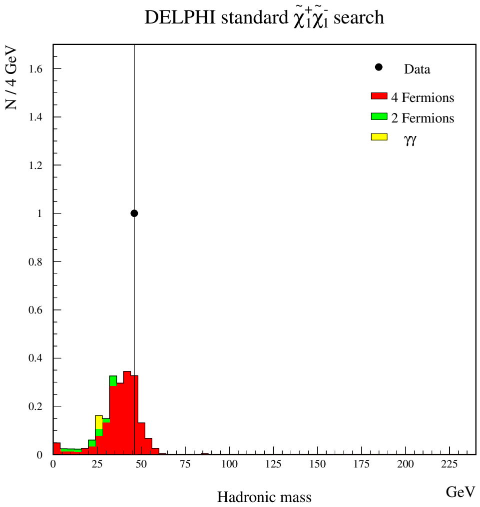

Figure B.4: A data–MC comparison after the preselection and the final selection for the $jj\ell$ topology. The data from year 2000 without TPC sector 6 is shown for the region 50 GeV/$c^2 \leq \Delta m$

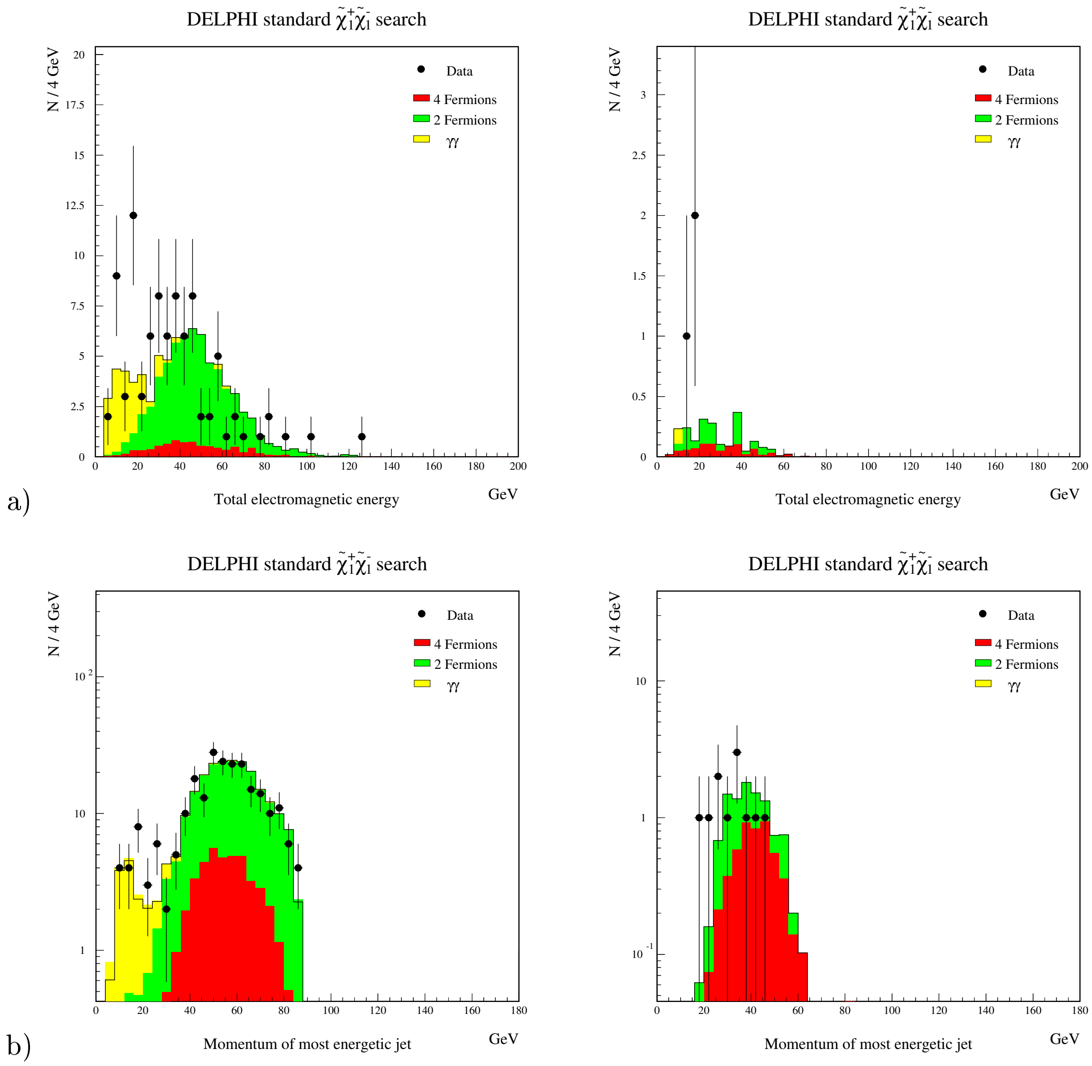

Figure B.5: A data–MC comparison after the preselection and the final selection for the radiative topology. The two cases correspond to the Δm regions: a) $3 \leq \Delta m < 35$ GeV/c^2 and b) 35 GeV/$c^2 \leq \Delta m$ with the data from year 2000 with TPC sector 6.

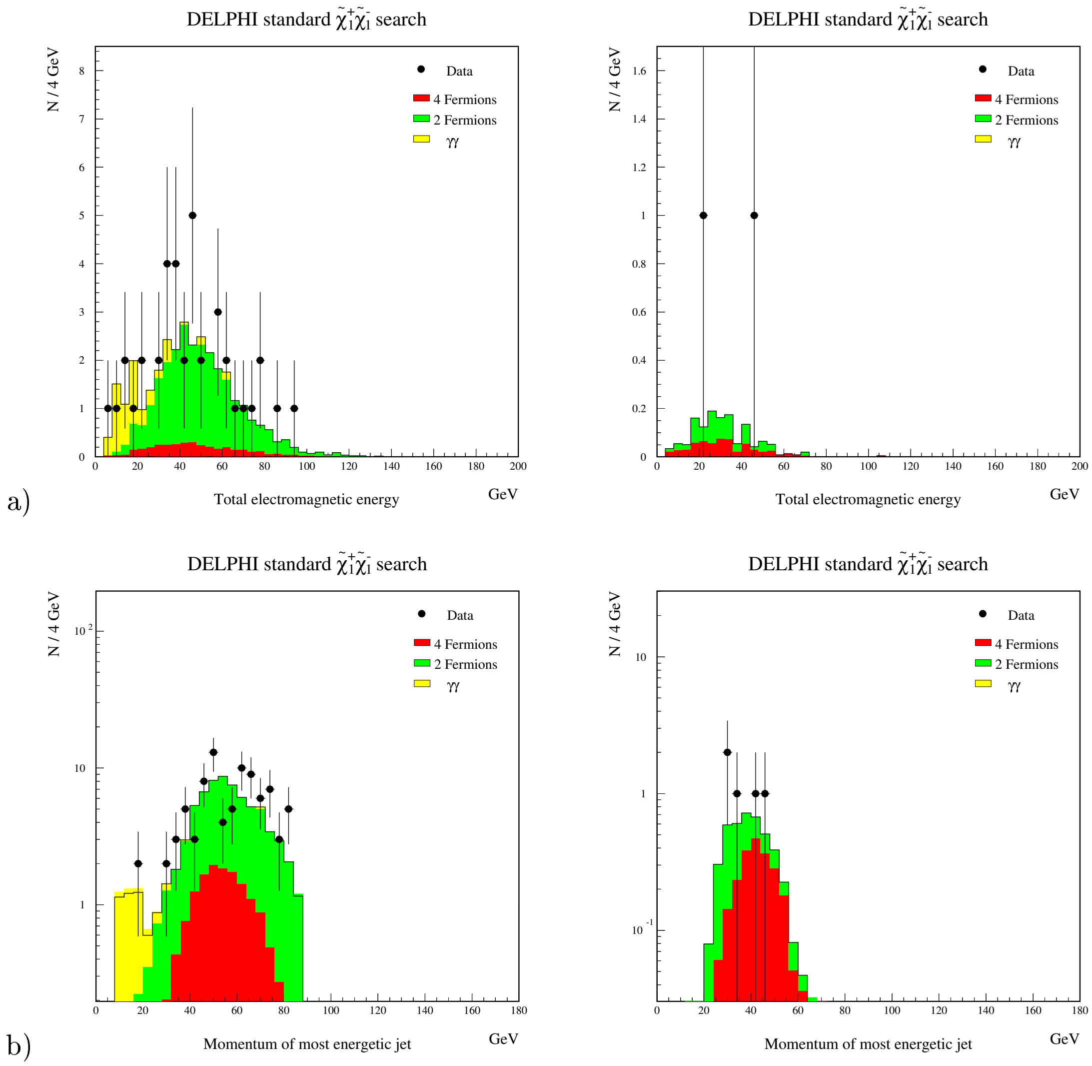

Figure B.6: A data–MC comparison after the preselection and the final selection for the radiative topology. The two cases correspond to the Δm regions: a) $3 \leq \Delta m < 35$ GeV/c^2 and b) 35 GeV/$c^2 \leq \Delta m$ with the data from year 2000 without TPC sector 6.

Appendix C

Data–MC Comparison after $\mathcal{L}_{\mathcal{R}}$–Cut

This appendix will present a data–MC comparison as a function of the **likelihood ratio cut** for the $jj\ell$ and rad topologies. All Δm windows will be shown for the data collected during year 2000 for both the period with and without the TPC sector 6. This is a complement to section 4.4 where one window from the $jj\ell$ and the rad topologies were discussed in detail.

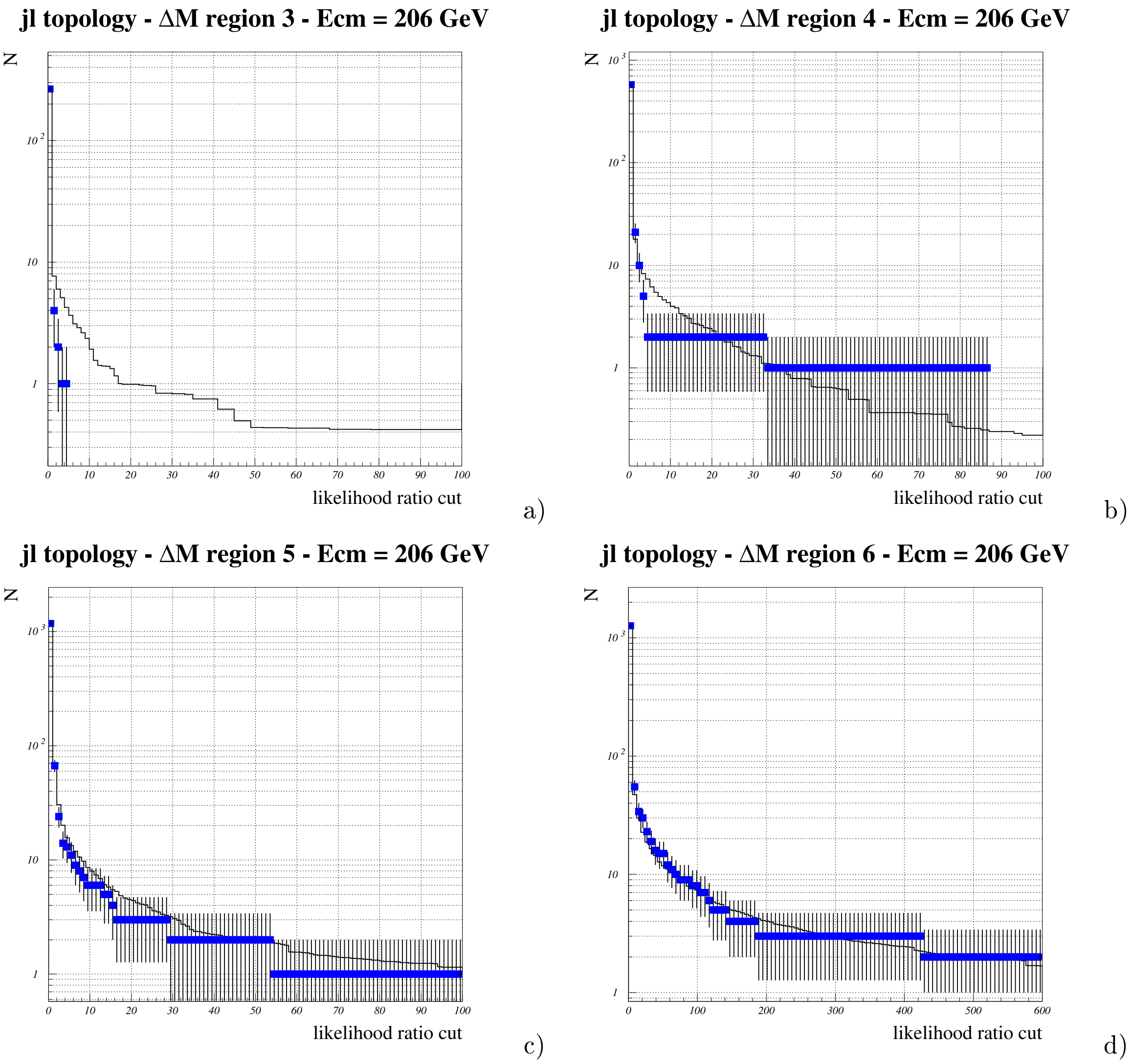

Figure C.1: The distributions of the number of real data (dots) and background events (histogram) as a function of the Likelihood Ratio cut for the $jj\ell$ topology: a) $3 \leq \Delta m < 25$ GeV/c^2, b) $25 \leq \Delta m < 35$ GeV/c^2, c) $35 \leq \Delta m < 50$ GeV/c^2, d) 50 GeV/$c^2 \leq \Delta m$. All plots show the data from year 2000 with TPC sector 6.

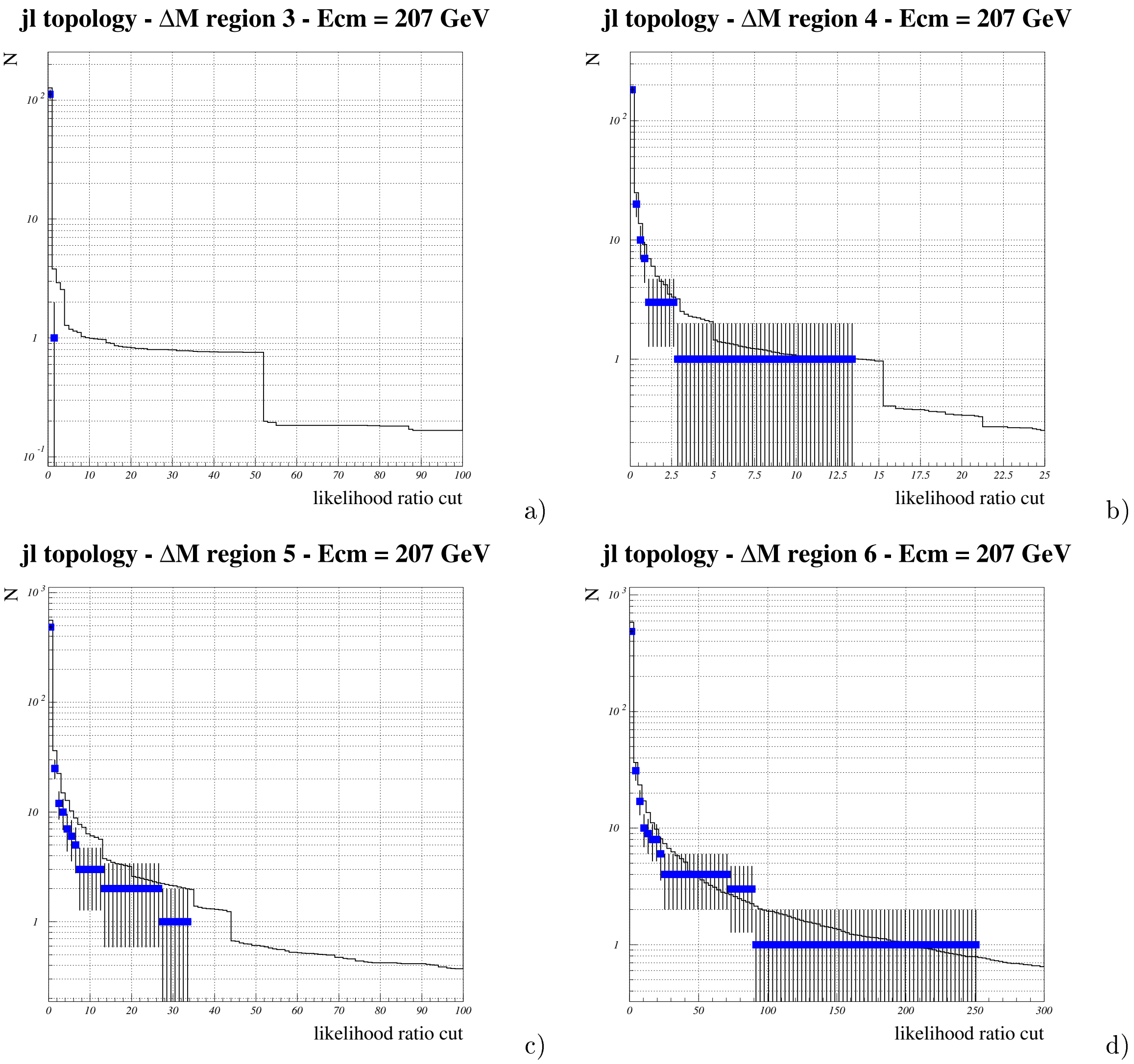

Figure C.2: The distributions of the number of real data (dots) and background events (histogram) as a function of the Likelihood Ratio cut for the $jj\ell$ topology: a) $3 \leq \Delta m < 25$ GeV/c^2, b) $25 \leq \Delta m < 35$ GeV/c^2, c) $35 \leq \Delta m < 50$ GeV/c^2, d) 50 GeV/$c^2 \leq \Delta m$. All plots show the data from year 2000 without TPC sector 6.

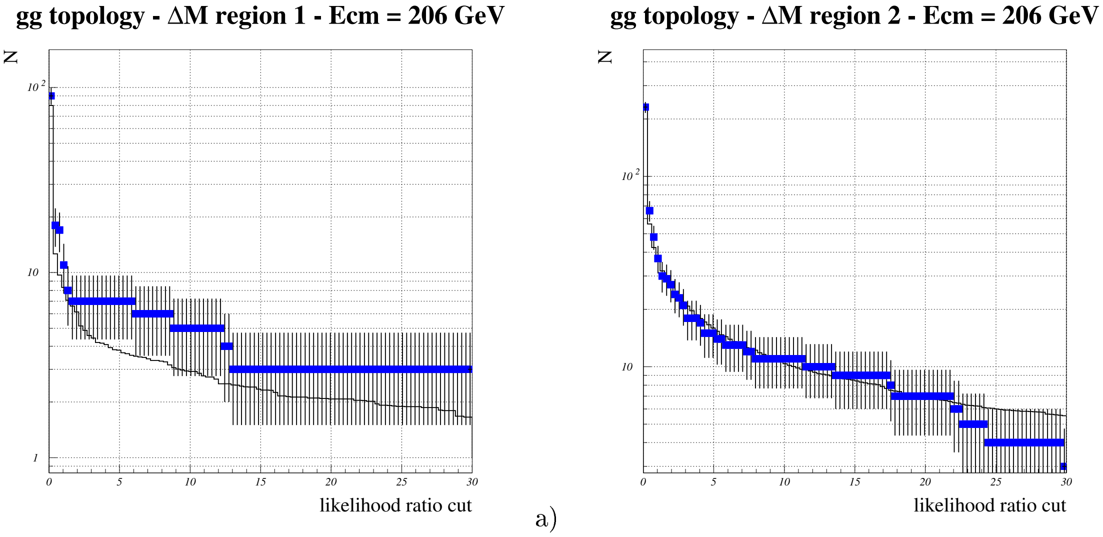

a) b)

Figure C.3: The distributions of the number of real data (dots) and background events (histogram) as a function of the Likelihood Ratio cut for the radiative topology: a) $3 \leq \Delta m < 35$ GeV/c^2, b) 35 GeV/c^2 $\leq \Delta m$. All plots show the data from year 2000 with TPC sector 6.

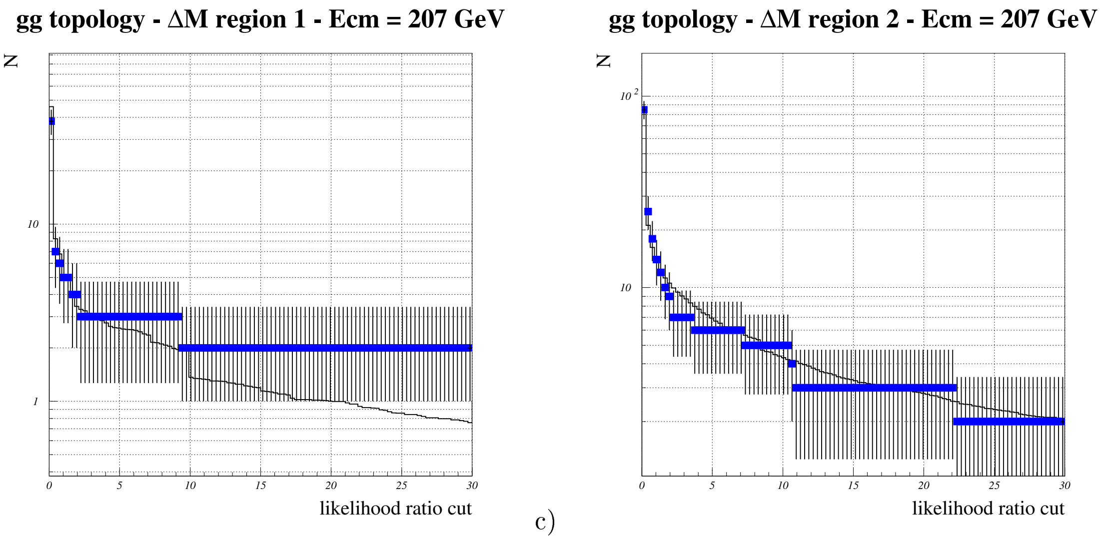

c) d)

Figure C.4: The distributions of the number of real data (dots) and background events (histogram) as a function of the Likelihood Ratio cut for the radiative topology: c) $3 \leq \Delta m < 35$ GeV/c^2, d) 35 GeV/c^2 $\leq \Delta m$. All plots show the data from year 2000 without TPC sector 6.

Bibliography

[1] J. Abdallah *et.al.* [DELPHI Collaboration], *Searches for supersymmetric particles in e+e- collisions up to 208 GeV, and interpretation of the results within the MSSM* , CERN-EP 2003-007, hep-ex/0311019 (Accepted for publication by Eur. Phys. J C).

[2] T. Alderweireld, *Search for charginos in e+e- interactions with the DELPHI detector at LEP*, Ph.D. thesis, Université de Mons (Sept. 2002), CERN-THESIS-03-009.

[3] P. Fayet and S. Ferrara, Phys. Rep. **32** (1977) 249.

[4] S.P. Martin, in "Perspectives on Supersymmetry", ed. G.L. Kane, World Sceientific, 1998; extended version, S.P. Martin, hep-ph/9709356.

[5] M.E. Peskin, "Beyond the standard model", SLAC-PUB-7479 (hep-ph/9705479).

[6] John R. Ellis (CERN), *Supersymmetry for alp hikers*, CERN-TH-2002-052, Mar 2002. Proceedings for ESHEP 2001, Beatenberg, Switzerland, 26 Aug - 8 Sep 2001 (hep-ph/0203114).

[7] G.F. Giudice and R. Rattazzi, Phys. Rep. **322** (1999) 419 (hep-ph/9801271).

[8] S. Ambrosanio and B. Mele, Phys. Rev. **D53** (1996) 2541.

[9] *LEP DESIGN REPORT: VOL. 1. THE LEP INJECTOR CHAIN*, CERN-LEP/TH/83-29, CERN/PS/DL/83-31, CERN/SPS/83-26, LAL/RT/83-09, Jun 1983. *LEP DESIGN REPORT: VOL. 2. THE LEP MAIN RING*, CERN-LEP/84-01, Jun 1984.

[10] DELPHI Collaboration, P. Aarnio *et al.*, Nucl. Inst. and Meth. **A303** (1991) 233; DELPHI Collaboration, P. Abreu *et al.*, Nucl. Inst. and Meth. **A378** (1996) 57.

[11] DELPHI Collaboration, P. Abreu *et al.*, Nucl. Inst. and Meth. **A362** (1995) 361.

[12] DELPHI Collaboration, DELPHI 89-44 PROG 137.

[13] T. Sjöstrand, Comp. Phys. Comm. **39** (1986) 347;
T. Sjöstrand, `PYTHIA 5.6` *and* `JETSET 7.3`, CERN-TH/6488-92.

[14] S. Jadach, W. Placzek and B.F.L. Ward, Phys. Lett. **B390** (1997) 298.

[15] J.E. Campagne and R. Zitoun, Z. Phys. **C43** (1989) 469.

[16] S. Jadach, B.F.L. Ward and Z. Was, Comp. Phys. Comm. **79** (1994) 503.

[17] F.A. Berends, R. Pittau, R. Kleiss, Comp. Phys. Comm. **85** (1995) 437.

[18] J.Fujimoto *et al.*, Comp. Phys. Comm. **100** (1997) 128

[19] S. Nova, A. Olshevski, and T. Todorov, *A Monte Carlo event generator for two photon physics*, DELPHI note 90-35 (1990).

[20] F.A. Berends, P.H. Daverveldt, R. Kleiss, Comp. Phys. Comm. **40** (1986) 271, Comp. Phys. Comm. **40** (1986) 285, Comp. Phys. Comm. **40** (1986) 309.

[21] S.Katsanevas and P.Morawitz, Comp. Phys. Comm. **112** (1998) 227.

[22] DELPHI Collaboration, DELPHI 89-67 PROG 142;
DELPHI Collaboration, DELPHI 89-68 PROG 143.

[23] F. Cossutti, A. Tonazzo, F. Mazzucato, *REMCLU : a package for the Reconstruction of Electromagnetic CLUsters at LEP200*, DELPHI note 2000-164 PROG 242 (2000).

[24] T.W. Anderson, An introduction to multivariate analysis, New York Wiley, 1958.

[25] DELPHI collaboration, Phys. Lett. **B479** (2000) 118;
T. Alderweireld, I. Gill, P. Rebecchi, *Review of the chargino search in DELPHI. Latest results at* $E_{cm} = 189$ GeV , CERN-OPEN-2002-031;
DELPHI collaboration, Phys. Lett. **B446** (1999) 75.

[26] J.Rehn *et al.*, *A technique to evaluate and propagate uncertainties in the Monte Carlo modeling of the event reconstruction*, DELPHI note 2003-065 PHYS 934 (2003).

[27] A. Behrmann, P.J. Holt *Muon Momentum and Muon Chamber Efficiency Corrections for LEPII*, DELPHI note 2002-017 PHYS 918 (2002).

[28] V.F. Obraztsov, Nucl. Instr. and Meth. **316** (1992) 388;
V.F. Obraztsov, Nucl. Instr. and Meth. **399** (1997) 500.

[29] A. Read *et al.*, *1st Workshop on Confidence Limits*, Yellow report CERN 2000-005, (May 2000) 81-103;
A. Read, note DELPHI 97-158 PHYS 737.